UC San Diego

Title
Magnetic and Surface Interactions of Functionalized Polydopamine Nanoparticles for Biomedical Applications

Permalink
https://escholarship.org/uc/item/8jt912ft

Author
Xie, Yijun

Publication Date
2019

Peer reviewed|Thesis/dissertation

UNIVERSITY OF CALIFORNIA SAN DIEGO

Magnetic and Surface Interactions of Functionalized Polydopamine Nanoparticles for Biomedical Applications

A dissertation submitted in partial satisfaction of the
requirement for the degree of Doctor of Philosophy

in

Materials Science and Engineering

by

Yijun Xie

Committee in charge:

       Professor Jeffrey Rinehart, Chair
       Professor Renkun Chen
       Professor Jesse Jokerst
       Professor William Trogler
       Professor Wei Xiong

2019

The dissertation of Yijun Xie is approved, and it is acceptable in quality and form for publication on microfilm and electronically:

_____

_____

_____

_____

_____
                                                                                                            Chair

University of California San Diego

2019

DEDICATION

I dedicate this thesis to my parents:

Qirong Xie & Wenjuan Wu

for supporting my decision with love

EPIGRAPH

Man proposes, God disposes.

TABLE OF CONTENTS

LIST OF ABBREVIATIONS

BF-STEM = bright field scanning transmission electron microscopy

CEUS = contrast-enhanced ultrasound

CFO = $CoFe_2O_4$

Co = Cobalt

Co(acac)$_2$ = cobalt(II) acetylacetonate

CPS = contrast pulse sequencing

CTAB = cetrimonium bromide

Cu = Copper

Cryo-TEM = Cryo-transmission electron microscopy

CT = computed tomography

D = axial anisotropy parameter

DA = dopamine hydrochloride

DHI = 5,6-dihydroxyindole

DHICA = 5,6-dihydroxyindole-2-carboxylic acid

DLS = dynamic light scattering

DMEM = Dulbecco's Modified Eagle Medium

DOPA = 3,4-dihydroxyl-L-phenylalanine

DOTA = diethylene triamine pentaacetic acid

EDS = energy dispersive X-ray spectroscopy

EELS = electron energy loss spectroscopy

EPR = Electron Paramagnetic Resonance

eV = electron volts

FBS = fetal bovine serum

FC = field-cooling

Fe = iron

Fe(acac)$_3$ = iron(III) acetylacetonate

g = grams

Gd = gadolinium

G = Gauss

h = hours

HAADF-STEM = high angle annular dark field scanning transmission electron microscopy

H$_A$ = anisotropy field

H$_c$ = coercive field

H$_{ex}$ = exchange bias field

HIFU = high intensity focused ultrasound

HPLC = high-performance liquid chromatography

ICP-OES = inductively coupled plasma-optical emission spectrometry

IR = Infrared Spectroscopy

K = Kelvin

L = liters

Mn = Manganese

MI = mechanical index

min = minutes

M$_r$ = remnant magnetization

M$_s$ = saturation magnetization

MTS = 3-(4,5-dimethylthiazol-2-yl)-5-(3-carboxymethoxyphenyl)-2-(4-sulfophenyl)-2H-tetrazolium

NIR = near-infrared

mol = moles

MRI = magnetic resonance imaging

MS = mass spectrometry

Nanoparticles = NPs

NaOH = Sodium hydroxide

Ni = Nickel

NMR= Nuclear magnetic resonance

NMRD = nuclear magnetic relaxation dispersion

NP = nanoparticle

Oe = oersted

PA = photoacoustic

PBS = phosphate-buffered saline

PDI = polydispersity

PDA = polydopamine

PDA-F NPs = fluorinated polydopamine nanoparticles

PDCA = pyrrole-2,3-dicarboxylic acid (PDCA)

PET = positron emission tomography

PFB = perfluorobutane

PFC = perfluorocarbon

PFH = perfluorohexane

PFP = perfluoropentane

R_1 = the longitudinal proton relaxation rates

RI = refractive index

ROI = regions of interest

ROS = reactive oxygen species

RT = room temperature

SEM = Scanning electron microscope

SMN = spherical micellar nanoparticles

SQUID = superconducting quantum interference device

STEM = scanning transmission electron microscopy

T = temperature

T_1 = longitudinal relaxation time

T_2 = transverse relaxation time

T_B = magnetic blocking temperature

T_N = Neel temperature

TEM = transmission electron microscopy

Tris = tris(hydroxymethyl)aminomethane

UCA = ultrasound contrast agent

US = ultrasound

UV = Ultraviolet

XPS = X-ray photoelectron spectroscopy

XRD = X-ray diffraction

ZFC = zero field-cooling

ZFS = zero-field splitting

LIST OF FIGURES

LIST OF TABLES

ACKNOWLEDGEMENTS

during all my PhD study. In addition, Dr. Ranjan Ramachandra helped me with the electron diffraction and EELS analysis. I am very grateful for their help as I always have a lot of questions to ask when I use TEM.

Finally, I would thank my parents. When I started my PhD, I realized that my parents did not want me to do research work as my career because it is too difficult, but they still supported my decision without any hesitation. I really appreciate their devotion. I always feel very lucky and gratefully to have them in my life. My father is a smart, quiet and focused man, and he teaches me the strength of reading and learning knowledge. My mother is very kind and soft, and she understands my feeling very well. They will always back me up at any situation. Also, I would like to thank my dear friend, Lihua Liu, who always encouraged me when I was overwhelmed by the negative emotion. She is also an expert in TEM and teaches me a lot of knowledge on TEM. Wherever I am, in Shanghai, Edmonton as well as San Diego, I always appreciate her support.

Chapter 2, is adapted in full reprint of the materials pubished in the following paper: **Structure and Function of Iron-Loaded Synthetic Melanin**, Yiwen Li[†], Yijun Xie[†], Zhao Wang[†], Nanzhi Zang, Fabio Carniato, Yuran Huang, Christopher M. Andolina, Lucas R. Parent, Treffly B. Ditri, Eric D. Walter, Mauro Botta, Jeffrey D. Rinehart,* Nathan C. Gianneschi,* *ACS Nano*, **2016**, 10, 10186-10194.; Copyright 2016 American Chemical Society. The dissertation author is the co-first author of this chapter. In Chapter 2, I would like to thank Dr. Yiwen Li, Dr. Zhao Wang, Prof. Nathan Gianneschi for the particle synthesis, MRI contrast study, magnetic study and design for the project. I am also thankful for the help from Dr. Yuran Huang, Nanzhi Zang, Dr. Lucas R. Parent and Dr. Treffly B. Ditri for the characterization of the nanoparticles. I also thank Fabio Carniato, Christopher M. Andolina, Eric D. Walter and Dr. Mauro Botta for their contributions to the further characterization of nanoparticles.

Chapter 3, in full, is a reprint of materials published in the following paper: **Perfluorocarbon-loaded polydopamine nanoparticles as ultrasound contrast agent**, Yijun Xie, James Wang, Zhao Wang, Kelsey A. Krug, Jeffery D. Rinehart, *Nanoscale* **2018**, 10, 12813-12819, with permission from The Royal Society of Chemistry. The dissertation author is the first author of this paper. For Chapter 3, I would like to

thank James Wang for the ultrasound imaging experiments, Dr. Zhao Wang for the particle characterization, and Kelsey A. Krug for the cell experiments.

Chapter 4, in full, has been submitted for publications for the following manuscript: **Tuning the ultrasonic and photoacoustic response of polydopamine-stabilized perfluorocarbon contrast agents**, Yijun Xie, Junxin Wang, James Wang, Ziying Hu, Ali Hariri, Nicholas Tu, Kelsey A. Krug, Michael D. Burkart, Nathan C. Gianneschi, Jesse V. Jokerst, and Jeffrey D. Rinehart, **2019** (in submission). The dissertation author is the first author of this paper. For Chapter 4, I appreciate the help from Dr. Junxin Wang and James Wang and Ali Hariri for the imaging study, Ziying Hu and Nicholas Tu for the materials characterization and synthesis, Kelsey A. Krug for the cell experiments. I also thank Dr. Nathan C. Gianneschi and Jesse V. Jokerst for their useful comments on the manuscript.

Chapter 5 is adapted in full reprint of the materials from the following paper: **Strengthening nanocomposite magnetism through microemulsion synthesis**, Yijun Xie, Alexandre H. Vincent, Haeun Chang, Jeffrey D. Rinehart, *Nano Research*, **2018**, 11, 4133–4141.; Copyright 2018, Tsinghua University Press and Springer-Verlag GmbH Germany, part of Springer Nature. The dissertation author is the first author of this paper. For Chapter 5, I would like to thank Alexandre H. Vincent and Haeun Chang for the materials synthesis.

VITA

2012	Bachelor of Engineering, Shanghai Jiao Tong University, Shanghai, China
2014	Master of Science, University of Alberta, Alberta, Canada
2019	Doctor of Philosophy, University of California San Diego, USA

PUBLICATIONS

Xie, Y.*; Wang, J.*; Wang, J.; Hu, Z.; Hariri, A.; Tu, N.; Krug, K. A.; Burkart, M.D.; Gianneschi, N.C.; Jokerst, J. V.; Rinehart, J. D., "Tuning the ultrasonic and photoacoustic response of polydopamine-stabilized perfluorocarbon contrast agents". *Under Review*.

Xie, Y.; Wang, J.; Wang, Z.; Krug, K. A.; Rinehart, J. D., "Perfluorocarbon-loaded polydopamine nanoparticles as ultrasound contrast agents". *Nanoscale* 2018, 10, 12813-12819.

Xie, Y.; Vincent, A.; Chang, H.; Rinehart, J. D., "Strengthening nanocomposite magnetism through microemulsion synthesis". *Nano Res*. 2018, 11, 4133-4141.

Wang, Z.; Carniato, F.; **Xie, Y.**; Huang, Y.; Li, Y.; He, S.; Zang, N.; Rinehart, J. D.; Botta, M.; Gianneschi, N. C., "High Relaxivity Gadolinium-Polydopamine Nanoparticles." *Small* 2017, 13, 1701830.

Wang, Z.*; **Xie, Y.***; Li, Y.; Huang, Y.; Parent, L. R.; Ditri, T.; Zang, N.; Rinehart, J. D.; Gianneschi, N. C., "Tunable, metal-loaded polydopamine nanoparticles analyzed by magnetometry." *Chem. Mater*. 2017, 29, 8195-8201.

Li, Y.*; **Xie, Y.***; Wang, Z.*; Zang, N.; Carniato, F.; Huang, Y.; Andolina, C.; Parent, L.; Ditri, T.; Walter, E.; Botta, M.; Rinehart, J. D.; Gianneschi, N. C., "Structure and Function of Iron-Loaded Synthetic Melanin". *ACS Nano* 2016, 10, 10186–10194.

Li, Y.; Huang, Y.; Wang, Z.; Carniato, F.; **Xie, Y.**; Patterson, J.; Thompson, M.; Andolina, C.; Ditri, T.; Millstone, J.; Figueroa, J.; Rinehart, J. D.; Scadeng, M.; Botta, M.; Gianneschi, N. C., "Polycatechol Nanoparticle MRI Contrast Agents". *Small* 2016, 12, 668–677.

* co-first author

ABSTRACT OF THE DISSERTATION

Magnetic and Surface Interactions of Functionalized Polydopamine Nanoparticles for Biomedical Applications

by

Yijun Xie

Doctor of Philosophy in Materials Science and Engineering

University of California San Diego, 2019

Professor Jeffrey Rinehart, Chair

Polydopamine (PDA) materials have provoked great attention in chemistry and materials science since 2007 due to their versatile properties including metal-ion chelation, easy functionalization, adhesion, and free radical scavenging ability. Produced via mild oxidation of dopamine monomer to form a colloidally-suspendable nanomaterial, polydopamine was initially developed as a versatile, biomimetic coating material, similar to the foot protein of mussels. Subsequently, PDA nanoparticles were developed as free radical scavengers and biomedical contrast agents amongst an ever-expanding list of applications. Currently, PDA nanoparticles are tunable in size within the range from tens to several hundred nanometers, and they can be easily loaded with metal ions and functionalized with different types of molecules.

Therefore, PDA materials have great potentials in applications such as biomedicine, catalysis, and environmental remediation.

In chapter 2, Fe^{3+}-loaded PDA materials were studied as magnetic resonance imaging (MRI) contrast agents. An amorphous metal-chelated polymer nanoparticle presents a significant challenge for characterizing the source of MRI contrast as structural data is complex and characterization methods limited. Tunable concentrations of Fe^{3+} were achieved and the structure and magnetic interaction were analyzed comprehensively by magnetometry and electron paramagnetic resonance. These characterizations indicate the antiferromagnetic coupling in Fe^{3+} centers and optimal Fe^{3+} concentrations can be predicted to improve the contrast performance of PDA materials.

In chapter 3 and 4, fluorocarbon-functionalized PDA and Fe^{3+}-loaded PDA NPs were investigated as ultrasound contrast agents. Traditional ultrasound imaging uses microbubbles with perfluorocarbon core and lipid shell to enhance an ultrasound signal. Herein, a balance between polarity and fluorophilicity is achieved to generate water-dispersible nanomaterials that also stabilize perfluorocarbon liquids. Results show strong and long-term US imaging capability, with chelation of Fe^{3+} introducing enhanced photoacoustic imaging capability.

In chapter 5, a facile method to generate magnetic exchange-bias between ferromagnetic and antiferromagnetic nanomaterials using nanoparticle emulsion clusters is developed. Magnetic $CoFe_2O_4/CoO$ nanoclusters are studied as proof-of-concept for exchange-bias behavior. This system shows a record exchange bias field (3200 Oe; 5K) for a nanoparticle-based system. This study gives a roadmap for extending synthetic methods beyond the superparamagnetic range and into composite single-domain materials for high-temperature magnetic materials with exchange-bias behavior.

Chapter 1 Introduction to Polydopamine Materials

1.1   Introduction

This chapter is intended to provide background information about the structure, synthetic technique and biomedical applications of polydopamine (PDA) materials. Various relevant techniques of biomedical imaging are also described. The introduction covers fundamental chemistry as it relates to applications both current and along future directions of polydopamine research.

1.2   Synthesis and Characterization of Polydopamine Nanoparticles

1.2.1   Structure of Polydopamine Materials

The production of PDA is generally achieved by a solution oxidation method.[1-2] The dopamine molecule is oxidized and self-polymerized under alkaline aqueous solution using oxygen as the oxidant. The mild and straightforward self-polymerization procedure is a major advantage in the production of PDA materials. Although polydopamine can be synthesized in such a simple procedure, the structure of PDA is amorphous, highly variable, and still an active area of investigation. In early studies of PDA structure, self-polymerization of PDA was suggested to have followed the pathway of natural eumelanin production.[3-4] Figure 1.1 shows a proposed polymerization mechanism, with dopamine being oxidized into dopamine quinone and cyclizing into leucodopaminechrome. It can be further oxidized and isomerized to 5,6-indolequinone. The further reactions can happen at positions 2, 3, 4, and 7, forming a cross-linked oligomer or polymer.
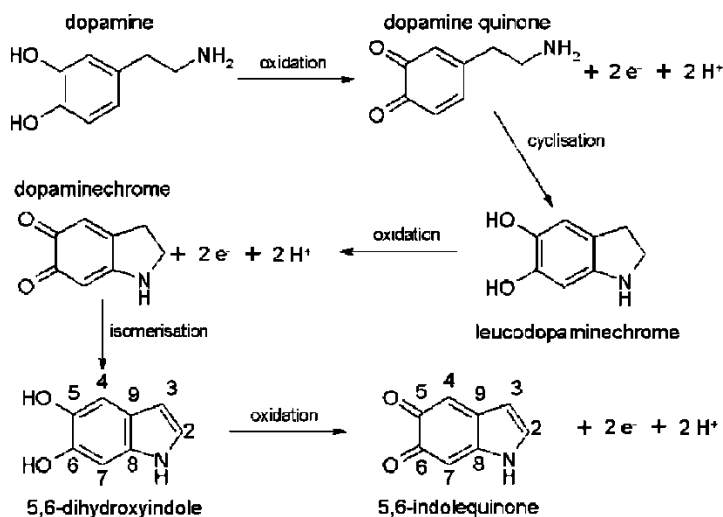
Figure 1.1 The molecular mechanism of the formation of PDA based on natural eumelanin production. Copyright 2011 American Chemical Society.[4]

In addition to the mechanism developed based on the eumelanin model, Dreyer *et al*. proposed another mechanism based on a supramolecular aggregates model (Figure 1.2). Using N and C nuclear magnetic resonance (NMR) analysis, the authors conclude that PDA is an aggregate of monomers cross linked through strong and noncovalent forces such as hydrogen bonding, charge transfer, and π- stacking. Rather than covalent bonding, other type of noncovalent, intermolecular interaction plays a more important role in this model.
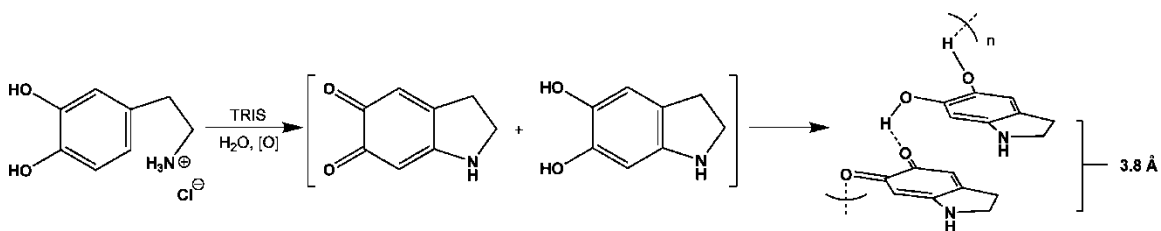
Figure 1.2 The molecular mechanism of the formation of PDA based on supramolecular aggregate model. Copyright 2012 American Chemical Society.[5]

Besides these two models, Hong *et al*. suggested that the formation of PDA is due to the synergistic effect of covalent polymerization and noncovalent self-assembly structure.[6] The authors use HPLC to identify the unpolymerized dopamine and polymerized dopamine, and found the self-assembly products from dopamine and 5,6-dihydroxyindole (DHI). [1]H-NRM data also indicates the covalent bond formation

of dopamine-DHI-DHI conjugates. Therefore, the authors suggested two different pathways: self-assembly

of dopamine-DHI and covalent band formation of dopamine-DHI happen together to the polymerization.
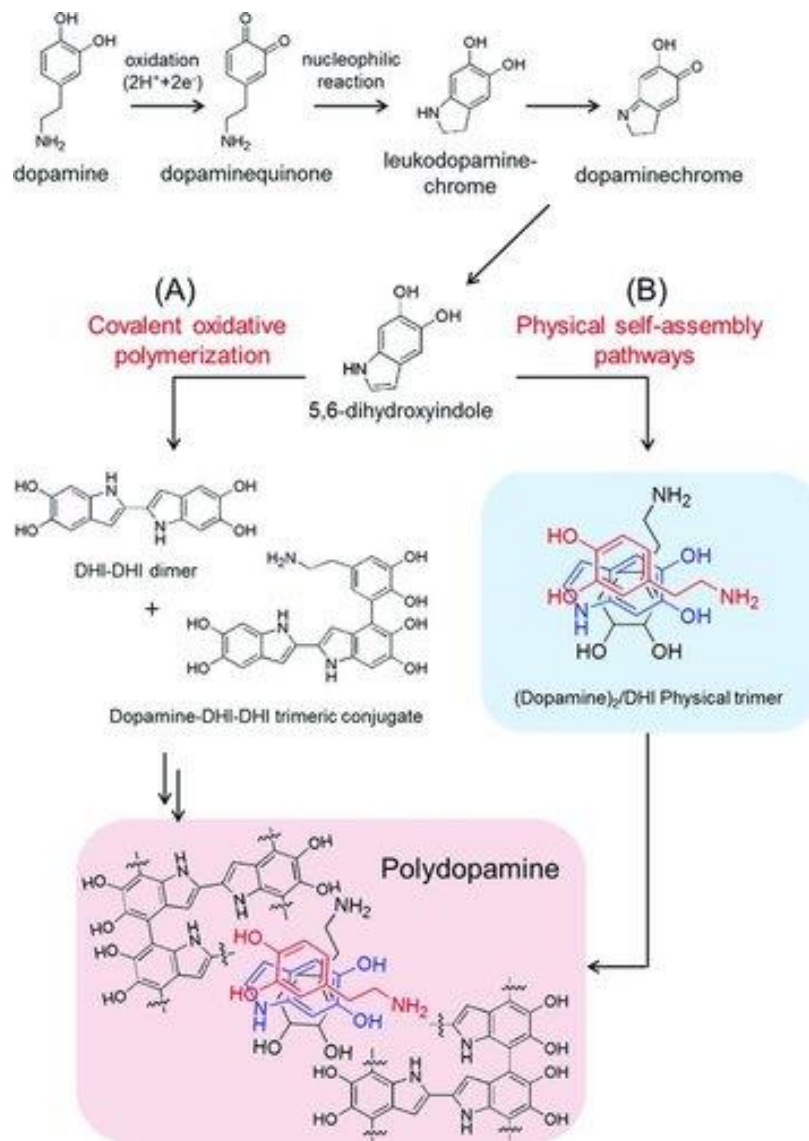
Figure 1.3 Two pathways for PDA synthesis: (A) covalent oxidative polymerization, and (B) physical self-assembly pathway of DHI and dopamine. Copyright 2012 John Wiley & Sons, Inc.[6]

1.2.2 Synthesis of Polydopamine Materials

As mentioned above, solution oxidation is the most common method for PDA synthesis.[1, 7] Generally, the commerical PDA monomer, dopamine hydrochloride can self-polymerize into PDA under alkaline aqueous solution with oxygen in the air. Mild alkaline conditions are used for the polymerization process. The polymerization process can be observed by the color change from pale yellow to black. For making PDA NPs, NaOH, $NH_3 \cdot H_2O$ and Tris can be used as the base source with a pH around 9-11 (Figure 1.4).[8-11] For making PDA coating film, pH value of the solution could be tuned from 5 to 8.5 with the increase of PDA film thickness.[12-13]
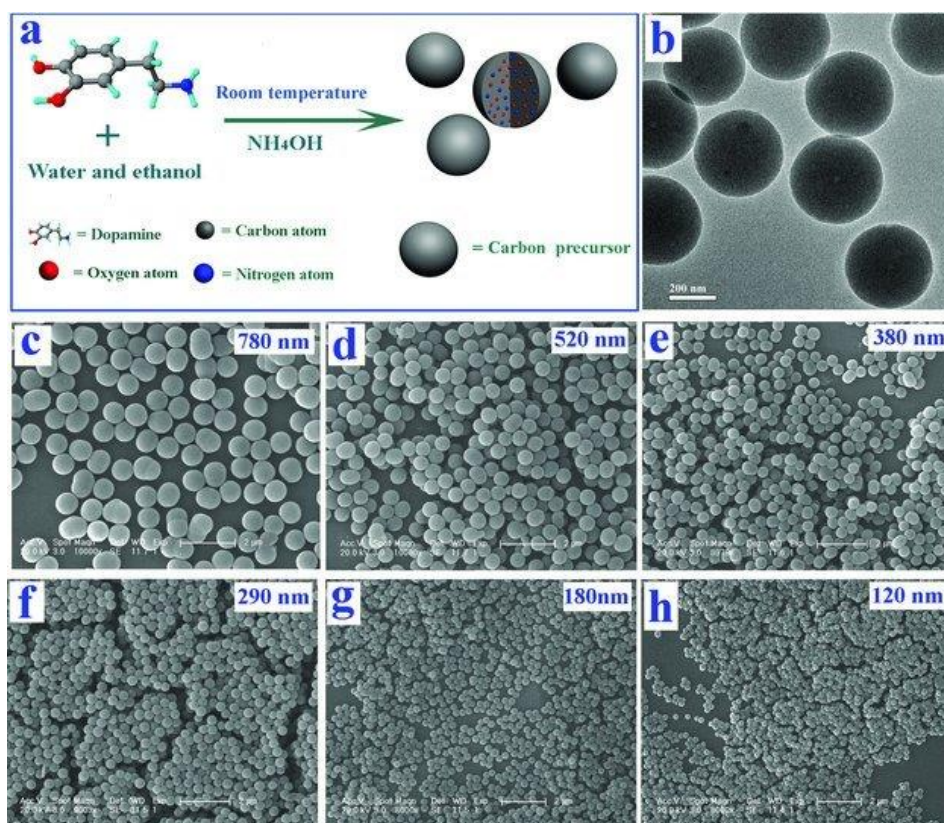
Figure 1.4 (a) Schematic illustration of the synthesis of PDA NPs, (b) Typical TEM image of PDA NPs. (c-h) SEM images of PDA NPs with different sizes. Copyright 2013 John Wiley & Sons, Inc.[11]

In the solution oxidation method, the type of the oxidant used in the reaction solution is very important for the formation of PDA. Besides oxygen, inorganic oxidants such as $(NH_4)_2S_2O_8$, $NaIO_4$,

NaClO$_4$, and KClO$_3$ can be used, for the oxidation and polymerization of dopamine in the alkaline aqueous solution.[2, 14-15] Furthermore, metal ions (e.g. Cu^{2+}, Ni^{2+}) are found to accelerate the polymerization of PDA.[16-17] When combined with H$_2$O$_2$, CuSO$_4$/H$_2$O$_2$ can produce reactive oxygen species (ROS), which can speed up the deposition rate of PDA on different surfaces.[18]

Enzymatic oxidation is another way to oxidize dopamine into PDA. The advantage of enzymes as the catalysts is their high efficiency and biocompatiability. For example, laccase can catalyze the polymerization of dopamine in aqueous solution and combine PDA into a robust matrix.[19] The resulting polymer composits can be used for biosensing. In another report, urease is used to catalyze the dopamine polymerization to form PDA NPs.[20]

Another type of synthetic method to make PDA is electropolymerization, which is generally used for coating PDA films on electrodes for electrochemical catalytic reaction. Lee et al reported the preparation of enzymatic biocatalytic cathode via electropolymerization of a multifunctional PDA film (Figure 1.5).[21] The electropolymerized PDA can form a compact biocatalytic thin film, which provides the long-lasting enzyme activity and stable structure for CO$_2$ reduction.
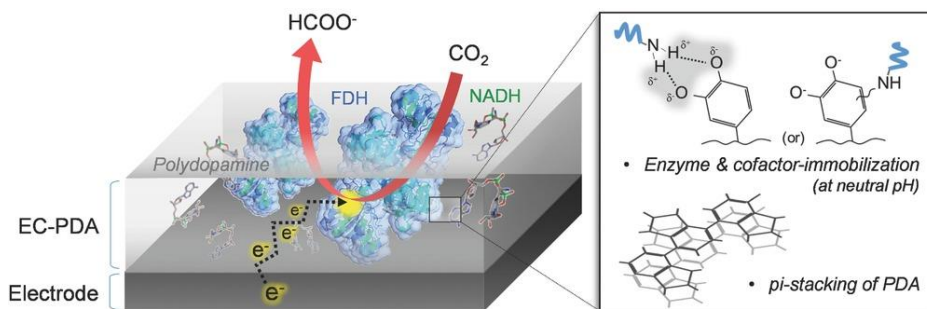
Figure 1.5 Schematic figure of 3D structure of EC-PDA film and its forming mechanism. Copyright 2016 John Wiley & Sons, Inc.[21]

1.3 Applications

1.3.1   Metal Ion Chelation and Magnetic Resonance Imaging (MRI)

One of the most interesting physical properties for PDA is the chelation ability with transition metal ions, including Fe^{3+}, Mn^{3+}, Co^{3+}, Cu^{2+}, etc. The binding site of PDA to metal ions include catechol, amine, o-quinone, imine groups.[22-23] Metal ion chelation was first studied in mussel byssal thread cutile, with catecholato-iron chelate complexes demonstrating strong mechanical properties.[24] The catechol binding strength and site could also be tuned at different pH conditions. For example, Niels et al reported that monocatechol-Fe species dominate at pH < 5.6, biscatechol-Fe species dominate at 5.6 < pH < 9.1, and triscatechol specties dominate at pH > 9.1.[25] In another work, Hong et al shows that Mg^{2+}, Ca^{2+}, Zn^{2+} can bind to carboxylic acid groups, while Cu^{2+} and Fe^{3+} bind to hydroxyl and amine groups;[26] In their study, IR absorption spectroscopy was used to examine the binding state of these metal ions to PDA.[27] It should be noted that some noble metal ions such as Au^{3+}, Ag^{+}, and Pt^{3+} can be reduced to metals by PDA along with the chelation.[2] The metal ions chelation properties of PDA materials give them with the possibility for the applications such as bioimaging and environmental remediation by such as metal ion sequestration.

Two important techniues to characterize the metal ions in PDA system are electron paramagnetic resonance (EPR) spectroscopy and superconducting quantum interference device (SQUID) magnetometry. EPR can be used to characterize many materials with unpaired electrons. Since many of the metal ions loaded into PDA will have unpaired electrons, it can be effective to characterize them by EPR. In one study, Im *et al*. confirmed Fe^{3+}-catechol complexation by EPR spectroscopy (Figure 1.6).[28] The g value of radicals in PDA and complexed Fe^{3+} is broad and similar (g = 2.00), the lower intensity of the characteristic peak from the Fe^{3+} loaded PDA sample compared with pure PDA indicates the Fe-catechol binding may interefere with the formation of free radical species or alter its relaxation properties. Compred with EPR, SQUID magnetometry is more suitable for characterizing the samples with more magnetically-concentrated species. In our own study, we use SQUID magneometry to study the Fe^{3+} and Mn^{3+} loaded PDA samples

with high metal concentrations.[29-30] The SQUID magnetometry could not only give us rough information about the symmetry of the coodination environment , but also tell us the magnetic interaction between the metal ions in the PDA system. For the metal loaded system, we can compine EPR spectroscopy with magnetometry, which can give us a complete information of coordination environment, magnetic interaction, local anisotropy as well as oxidation state of metals.
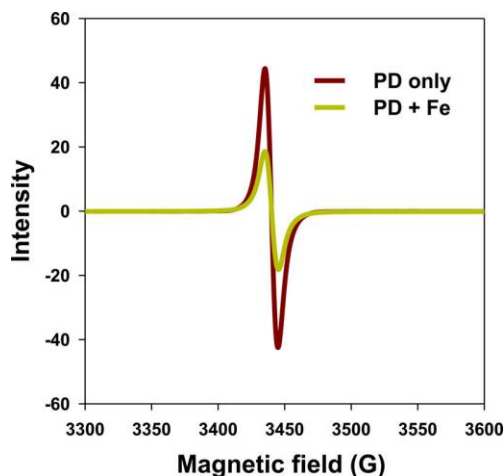
Figure 1.6 EPR spectra of PDA and Fe-doped PDA. Copyright 2012 American Chemical Society.[28]

One of the important applications for metal-loaded PDA materials is MRI imaging technique. MRI is one of the most widely-used and information-rich imaging techniques in hospitals and scientific research due to its very high spatial resolution, non-invasiveness, and high penetration depth. The technique of ^{1}H MRI was developed in the 1970s and ^{19}F MRI was developed in the 1990s.[31] The basic principle of MRI is analogous to that of nuclear magnetic resonance (NMR). The alignment and relaxation of proton spins in the magnetic field is the key to the principle of MRI.[32] The spins of protons will align parallel or antiparallel along the direction of magnetic field and produce a net magnetic moment. The spins will also precess with a specified frequency around the magnetic field, called Larmor frequency (Figure 1.7a).[32]
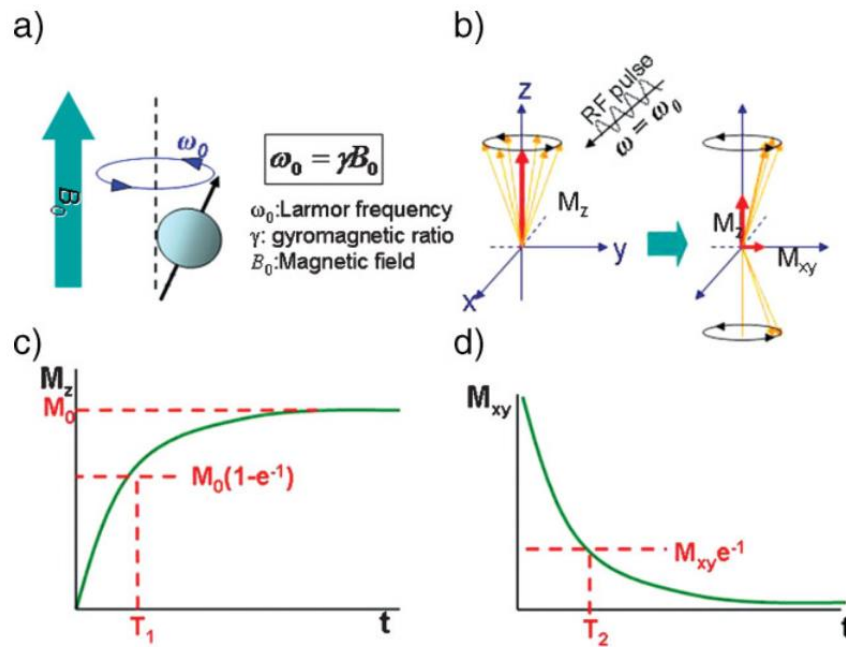
Figure 1.7 (a) The precession of proton spins under the magnetic field B_0 under the Larmor frequency ω_0, (b) the change of precession and magnetization state of proton spins after the introduction of RF frequency, (c) T_1 relaxation process of spins, (d) T_2 relaxation process of spins. Copyright 2009 John Wiley & Sons, Inc.[32]

When a radiofrequency (RF) pulse is introduced onto the proton spins (Figure 1.7b), the precession state of the spins will be disturbed, the protons adsorb the RF energy and are excited to the antiparallel state. After removing the RF pulse, the excited proton spins will relax to their equilibrium state. Two different relaxation processes can be defined to characterize the spin relaxation. The first is longitudinal relaxation (T_1 relaxation), in which the magnetization (M_z) will decrease to its initial state (Figure 1.7c). The second one is transverse relaxation (T_2 relaxation), in which the magnetization in the perpendicular plane (M_{xy}) disappears by the spin dephasing (Figure 1.7d).[32]

Although the MRI technique has the advantage of high resolution, the image contrast and sensitivity suffer due to the long relaxation time of water protons. Additional contrast agent is essential to enhance the image contrast and sensitivity of detection. As there are two relaxation pathways in MRI, there are two methods of creating of MRI contrast: T_1 and T_2 contrast agents. Typical T_1 contrast agents are paramagnetic chelates such as Gd-DTPA and Gd-DOTA;[33] The advantage of Gd chelates is the seven unpaired electrons

from Gd^{3+}, which gives a large net magnetic moment which can greatly enhances its relaxation rate (Figure 1.8). However, due to the potential toxicity of Gd^{3+} in biological system, transition metals such as Mn^{2+}, Fe^{3+}, Cu^{2+} can be used to replace Gd^{3+} due to their presence in biological processes. For example, Mn^{2+} in the form of $MnCl_2$ solution has been used to visualize the anatomic structure of the brain.[34] Typical T_2 contrast agents are ferrimagnetic Fe_3O_4 nanoparticles. The high magnetization of Fe_3O_4 nanoparticles can create field inhomogeneity and shorten the T_2 relaxation time, producing the T_2 contrast.

Ion	Configuration		Magnetic moment
	3d	4f	
Transition metal ion			
$^{24}Cr^{3+}$	⇡⇡⇡ ——		3.88
$^{25}Mn^{2+}$	⇡⇡⇡⇡⇡		5.92
$^{26}Fe^{3+}$	⇡⇡⇡⇡⇡		5.92
$^{29}Cu^{2+}$	⇅⇅⇅⇅⇡		1.73
lanthanide metal ion			
$^{63}Eu^{3+}$		⇅⇡⇡ ⇡⇡⇡⇡	3.4
$^{64}Gd^{3+}$		⇡⇡⇡ ⇡⇡⇡⇡	7.94
$^{66}Dy^{3+}$		⇅⇅⇡ ⇡⇡⇡⇡	10.65

Figure 1.8 3d and 4f electron configuration and magnetic moment of different metal ions. Copyright 2009 John Wiley & Sons, Inc.[32]

1.3.2 Ultrasound imaging

Ultrasound imaging is one of the most widely used imaging technique in the world. Similar to MRI, it has the advantage of noninvasive and safety, while it also has the advantage of low cost and real-time imaging. The contrast shown in ultrasound imaging requires density difference between tissues to produce different acoustic impedance resistance to sound propagation.[35] Ultrasound contrast agents can create very large acoustic impedance since many of them are made of volatile gas, thus enhancing the ultrasound signal. One of the most commonly used ultrasound contrast agents are microbubbles, which is $1 - 7$ μm in size. Microbubbles can behave as blood-pool markers, tracers, and cardiac imaging.[36] The microbubbles are made of gas core such as air or perfluorocarbon (PFC) gas, and stabilizing shell (such as phospholipids and polymer, albumin). The core materials can give them biocompatibility and persistence for minutes after injection. One of the major contribution of microbubbles to the ultrasound imaging is Doppler mode. The

Doppler mode signal correlates frequency shifts to relative motion. The echoes from stationery tissue and moving scatterers generate different signal Doppler frequencies. The big difference in density of bubbles and tissues represents a large impedance mismatch and the echogenicity. Figure 1.9 shows the typical ultrasound images with doppler mode on hepatic tumor tissue. In addition, when the microbubbles are exposed to an ultrasound pulse, they will vibrate like alternate contraction and expansion. Their vibrating resonance frequency is around 2-10 MHz, which corresponds to the frequencies used in diagnostic ultrasound facility.[36]

Another contribution from the applications of ultrasound contrast agent is the contrast pulse sequencing (CPS) imaging mode. CPS is an another type of contrast-enhanced ultrasound imaging technology that uses nonlinear signal from the contrast agent, which is different from the linear signal from the tissues and improves the spatial resolution and sensitivity.[37-39] CPS can provide higher penetration depth and less attenuation than conventional ultrasound imaging technique. Figure 1.10 shows an example of CPS imaging.
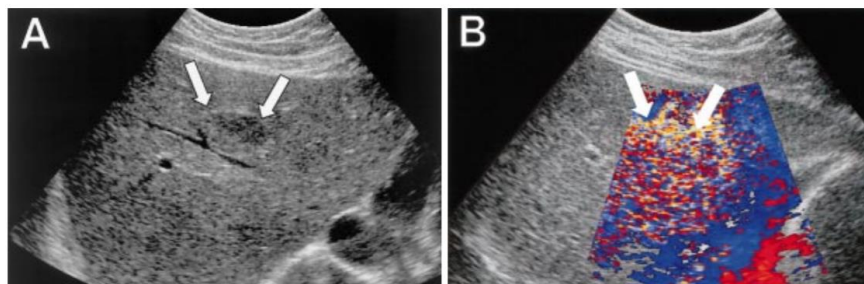
Figure 1.9 Ultrasound images from a focal nodular hyperplasia with (A) conventional B mode image, (B) color Doppler mode with Levovist (2.5 g, 400 mg/ml) as the contrast agent. Copyright 2001 Springer-Verlag.[40]

Due to the large size of microbubbles, next-generation ultrasound contrast agents were developed with smaller than 1 μm size (Figure 1.11). For example, nanoparticle can be used as the cavitation seeds for the ultrasound imaging. Goodwin et al. reported the air-encapsulation mesoporous silica nanoparticles.[41] The 100 nm mesoporous silica nanoparticles are functionalized with octyl groups and Pluronic F127 which can fill the nanoparticles with air and still stable in aqueous solution. The administration of high intensity

focused ultrasound (HIFU) allows sensitive imaging with very low concentration of nanoparticles.[41] Coussios et al. reported a sub-micron size of polystyrene (PS) nanocups for B-mode imaging and drug delivery, and the ultrasound-propelled nanocups can travel and enhance the delivery of unmodified therapeutics.[42] In our previous study, we use F-functionalized PDA nanoparticles loaded with perfluoropentane (PFP) for ultrasound contrast agents, and our *in vitro* study shows high imaging contrast and long imaging time using our materials.[43]
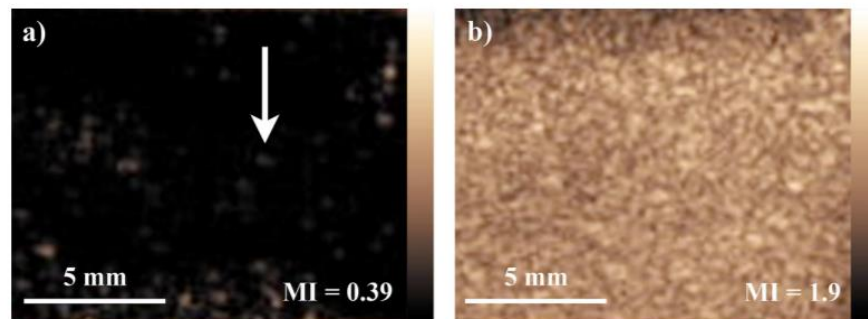
Figure 1.10 CPS Imaging of gas filled silica particles, (a) CPS images at mechanical index (MI) of 0.39, (b) CPS images at MI of 1.9. Copyright 2012 AIP Publishing LLC.[39]
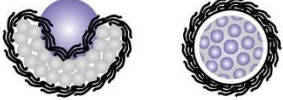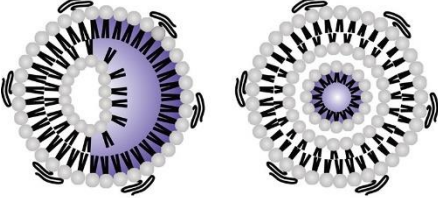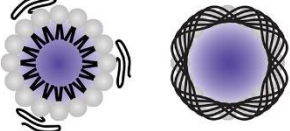
Agent Type	Shell	Core	Size (Diameter)
Cavitation seed	Lipid, polymer	Solid core with gas pockets	20 - 500 nm
Echogenic liposome	Lipid bilayer	Aqueous core with gas pockets (perfluorocarbon)	100 nm - 10 um
Nanobubble	Lipid, polymer, protein	Gas core (perfluorocarbon)	100 - 800 nm
Gas vesicle	Protein	Gas core	45 - 250 nm (diameter) 100 - 600 nm (length)
Nanodroplet	Lipid, polyer	Liquid core (perfluorocarbon)	200 - 400 nm

Figure 1.11 The size and composition of different sub-micron ultrasound contrast agents. Copyright 2017 John Wiley & Sons, Inc. [44]

1.3.3 Photoacoustic imaging

Photoacoustic imaging (PA) is a new type of imaging technique based on laser-activated ultrasound generation (light in, ultrasound out). It combines the high contrast and spectroscopy capability of optical imaging with the high spatial resolution of ultrasound imaging. In PA imaging, ultrasound waves will be generated after irradiating the tissue with modulated electromagnetic radiation like pulse laser.[45] The commonly used radiation source is a laser with the wavelength between 550 and 900 nm.[45] The near-infrared (NIR) range can provide the largest penetration depth for the tissue. Strong adsorption in NIR range can provide good PA signal. From this standpoint, PA contrast agents generally have great absorption in NIR spectral range. PDA is a good candidate for PA contrast agent since it has good adsorption in NIR range. Zhang et al. reported an Iridium(III) complexes loaded PDA nanoparticles for multimodal imaging and cancer therapy.[46] The nanoparticles show strong PA signal in mice tumor and demonstrate the great advantage in imaging-guided cancer therapy and real-time monitoring of the response to therapy (Figure

1.12). In another example, peptide functionalized PDA nanoparticles can be used for the combined PA imaging and photothermal therapy.[47] In our current study, we made F-functionalized Fe-loaded PDA nanoparticles with US/PA dual imaging modality. Initial *in vivo* study shows that subcutaneously injection of nanoparticles exhibits strong PA signal in nude mouse.
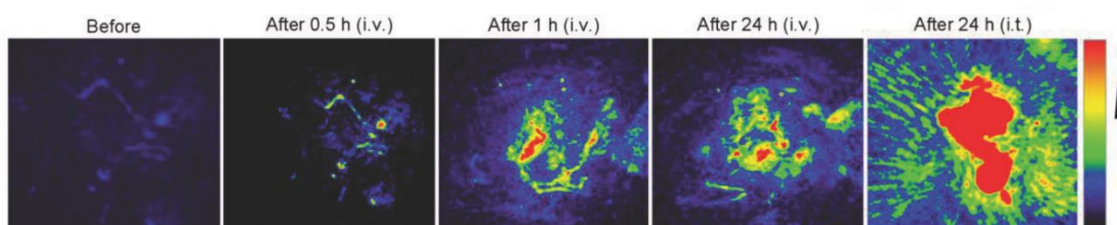
Figure 1.12 *In vivo* photoacoustic imaging of tumors in mice. Copyright 2018 John Wiley & Sons, Inc.[46]

1.4 References

(1) Lee, H.; Dellatore, S. M.; Miller, W. M.; Messersmith, P. B. Mussel-Inspired Surface Chemistry for Multifunctional Coatings. *Science* **2007,** *318* (5849), 426.

(2) Liu, Y.; Ai, K.; Lu, L. Polydopamine and Its Derivative Materials: Synthesis and Promising Applications in Energy, Environmental, and Biomedical Fields. *Chem. Rev.* **2014,** *114* (9), 5057-5115.

(3) Łuczak, T. Preparation and characterization of the dopamine film electrochemically deposited on a gold template and its applications for dopamine sensing in aqueous solution. *Electrochim. Acta* **2008,** *53* (19), 5725-5731.

(4) Bernsmann, F.; Ball, V.; Addiego, F.; Ponche, A.; Michel, M.; Gracio, J. J. d. A.; Toniazzo, V.; Ruch, D. Dopamine−Melanin Film Deposition Depends on the Used Oxidant and Buffer Solution. *Langmuir* **2011,** *27* (6), 2819-2825.

(5) Dreyer, D. R.; Miller, D. J.; Freeman, B. D.; Paul, D. R.; Bielawski, C. W. Elucidating the Structure of Poly(dopamine). *Langmuir* **2012,** *28* (15), 6428-6435.

(6) Hong, S.; Na, Y. S.; Choi, S.; Song, I. T.; Kim, W. Y.; Lee, H. Non-Covalent Self-Assembly and Covalent Polymerization Co-Contribute to Polydopamine Formation. *Adv. Funct. Mater.* **2012,** *22* (22), 4711-4717.

(7) Zhang, L.; Wu, J.; Wang, Y.; Long, Y.; Zhao, N.; Xu, J. Combination of Bioinspiration: A General Route to Superhydrophobic Particles. *J. Am. Chem. Soc.* **2012,** *134* (24), 9879-9881.

(8) Ju, K.-Y.; Lee, J. W.; Im, G. H.; Lee, S.; Pyo, J.; Park, S. B.; Lee, J. H.; Lee, J.-K. Bio-Inspired, Melanin-Like Nanoparticles as a Highly Efficient Contrast Agent for T1-Weighted Magnetic Resonance Imaging. *Biomacromolecules* **2013,** *14* (10), 3491-3497.

(9) Liu, Y.; Ai, K.; Liu, J.; Deng, M.; He, Y.; Lu, L. Dopamine-Melanin Colloidal Nanospheres: An Efficient Near-Infrared Photothermal Therapeutic Agent for In Vivo Cancer Therapy. *Adv. Mater.* **2013,** *25* (9), 1353-1359.

(10) Yue, Q.; Wang, M.; Sun, Z.; Wang, C.; Wang, C.; Deng, Y.; Zhao, D. A versatile ethanol-mediated polymerization of dopamine for efficient surface modification and the construction of functional core–shell nanostructures. *J. Mater. Chem. B* **2013,** *1* (44), 6085-6093.

(11) Ai, K.; Liu, Y.; Ruan, C.; Lu, L.; Lu, G. Sp2 C-Dominant N-Doped Carbon Sub-micrometer Spheres with a Tunable Size: A Versatile Platform for Highly Efficient Oxygen-Reduction Catalysts. *Adv. Mater.* **2013,** *25* (7), 998-1003.

(12) Ryu, J.; Ku, S. H.; Lee, H.; Park, C. B. Mussel-Inspired Polydopamine Coating as a Universal Route to Hydroxyapatite Crystallization. *Adv. Funct. Mater.* **2010,** *20* (13), 2132-2139.

(13) Ball, V.; Frari, D. D.; Toniazzo, V.; Ruch, D. Kinetics of polydopamine film deposition as a function of pH and dopamine concentration: Insights in the polydopamine deposition mechanism. *J. Colloid Interface Sci.* **2012,** *386* (1), 366-372.
(14) Deng, Z.; Shang, B.; Peng, B. Polydopamine Based Colloidal Materials: Synthesis and Applications. *Chem. Rec.* **2018,** *18* (4), 410-432.

(15) Wei, Q.; Zhang, F.; Li, J.; Li, B.; Zhao, C. Oxidant-induced dopamine polymerization for multifunctional coatings. *Polym. Chem.* **2010,** *1* (9), 1430-1433.

(16) Yang, L.; Kong, J.; Zhou, D.; Ang, J. M.; Phua, S. L.; Yee, W. A.; Liu, H.; Huang, Y.; Lu, X. Transition-Metal-Ion-Mediated Polymerization of Dopamine: Mussel-Inspired Approach for the Facile Synthesis of Robust Transition-Metal Nanoparticle–Graphene Hybrids. *Chem. Eur. J.* **2014,** *20* (25), 7776-7783.

(17) Ge, R.; Lin, M.; Li, X.; Liu, S.; Wang, W.; Li, S.; Zhang, X.; Liu, Y.; Liu, L.; Shi, F.; Sun, H.; Zhang, H.; Yang, B. Cu2+-Loaded Polydopamine Nanoparticles for Magnetic Resonance Imaging-Guided pH- and Near-Infrared-Light-Stimulated Thermochemotherapy. *ACS Appl. Mater. Interfaces* **2017,** *9* (23), 19706-19716.

(18) Zhang, C.; Ou, Y.; Lei, W.-X.; Wan, L.-S.; Ji, J.; Xu, Z.-K. CuSO4/H2O2-Induced Rapid Deposition of Polydopamine Coatings with High Uniformity and Enhanced Stability. *Angew. Chem., Int. Ed.* **2016,** *55* (9), 3054-3057.

(19) Tan, Y.; Deng, W.; Li, Y.; Huang, Z.; Meng, Y.; Xie, Q.; Ma, M.; Yao, S. Polymeric Bionanocomposite Cast Thin Films with In Situ Laccase-Catalyzed Polymerization of Dopamine for Biosensing and Biofuel Cell Applications. *J. Phys. Chem. B* **2010,** *114* (15), 5016-5024.

(20) Li, N.; Wang, H.-B.; Thia, L.; Wang, J.-Y.; Wang, X. Enzymatic-reaction induced production of polydopamine nanoparticles for sensitive and visual sensing of urea. *Analyst* **2015,** *140* (2), 449-455.

(21) Lee, S. Y.; Lim, S. Y.; Seo, D.; Lee, J.-Y.; Chung, T. D. Light-Driven Highly Selective Conversion of CO_2 to Formate by Electrosynthesized Enzyme/Cofactor Thin Film Electrode. *Advanced Energy Materials* **2016,** *6* (11), 1502207.

(22) Barclay, T. G.; Hegab, H. M.; Clarke, S. R.; Ginic-Markovic, M. Versatile Surface Modification Using Polydopamine and Related Polycatecholamines: Chemistry, Structure, and Applications. *Adv. Mater. Interfaces* **2017,** *4* (19), 1601192.

(23) d'Ischia, M.; Napolitano, A.; Pezzella, A.; Meredith, P.; Sarna, T. Chemical and Structural Diversity in Eumelanins: Unexplored Bio-Optoelectronic Materials. *Angew. Chem., Int. Ed.* **2009,** *48* (22), 3914-3921.

(24) Harrington, M. J.; Masic, A.; Holten-Andersen, N.; Waite, J. H.; Fratzl, P. Iron-Clad Fibers: A Metal-Based Biological Strategy for Hard Flexible Coatings. *Science* **2010,** *328* (5975), 216.

(25) Holten-Andersen, N.; Harrington, M. J.; Birkedal, H.; Lee, B. P.; Messersmith, P. B.; Lee, K. Y. C.; Waite, J. H. pH-induced metal-ligand cross-links inspired by mussel yield self-healing polymer networks with near-covalent elastic moduli. *Proceedings of the National Academy of Sciences* **2011,** *108* (7), 2651.

(26) Hong, L.; Liu, Y.; Simon, J. D. Binding of Metal Ions to Melanin and Their Effects on the Aerobic Reactivity¶. *Photochem. Photobiol.* **2004,** *80* (3), 477-481.
(27) Hong, L.; Simon, J. D. Insight into the Binding of Divalent Cations to Sepia Eumelanin from IR Absorption Spectroscopy. *Photochem. Photobiol.* **2006,** *82* (5), 1265-1269.

(28) Im, K. M.; Kim, T.-W.; Jeon, J.-R. Metal-Chelation-Assisted Deposition of Polydopamine on Human Hair: A Ready-to-Use Eumelanin-Based Hair Dyeing Methodology. *ACS Biomaterials Science & Engineering* **2017,** *3* (4), 628-636.

(29) Li, Y.; Xie, Y.; Wang, Z.; Zang, N.; Carniato, F.; Huang, Y.; Andolina, C. M.; Parent, L. R.; Ditri, T. B.; Walter, E. D.; Botta, M.; Rinehart, J. D.; Gianneschi, N. C. Structure and Function of Iron-Loaded Synthetic Melanin. *ACS Nano* **2016,** *10* (11), 10186-10194.

(30) Wang, Z.; Xie, Y.; Li, Y.; Huang, Y.; Parent, L. R.; Ditri, T.; Zang, N.; Rinehart, J. D.; Gianneschi, N. C. Tunable, Metal-Loaded Polydopamine Nanoparticles Analyzed by Magnetometry. *Chem. Mater.* **2017,** *29* (19), 8195-8201.

(31) Fox, M. S.; Gaudet, J. M.; Foster, P. J. Fluorine-19 Mri Contrast Agents for Cell Tracking and Lung Imaging. *Magnetic Resonance Insights* **2015,** *8s1*, MRI.S23559.

(32) Na, H. B.; Song, I. C.; Hyeon, T. Inorganic Nanoparticles for MRI Contrast Agents. *Adv. Mater.* **2009,** *21* (21), 2133-2148.

(33) Caravan, P.; Ellison, J. J.; McMurry, T. J.; Lauffer, R. B. Gadolinium(III) Chelates as MRI Contrast Agents: Structure, Dynamics, and Applications. *Chem. Rev.* **1999,** *99* (9), 2293-2352.

(34) Silva, A. C.; Lee, J. H.; Aoki, I.; Koretsky, A. P. Manganese-enhanced magnetic resonance imaging (MEMRI): methodological and practical considerations. *NMR Biomed.* **2004,** *17* (8), 532-543.

(35) Schutt, E. G.; Klein, D. H.; Mattrey, R. M.; Riess, J. G. Injectable Microbubbles as Contrast Agents for Diagnostic Ultrasound Imaging: The Key Role of Perfluorochemicals. *Angew. Chem., Int. Ed.* **2003,** *42* (28), 3218-3235.

(36) Cosgrove, D. Ultrasound contrast agents: An overview. *Eur. J. Radiol.* **2006,** *60* (3), 324-330.

(37) Phillips, P.; Gardner, E. Contrast-agent detection and quantification. *Eur. Radiol.* **2004,** *14*, P4-P10.

(38) Rissanen, T. T.; Korpisalo, P.; Karvinen, H.; Liimatainen, T.; Laidinen, S.; Gröhn, O. H.; Ylä-Herttuala, S. High-Resolution Ultrasound Perfusion Imaging of Therapeutic Angiogenesis. *JACC: Cardiovascular Imaging* **2008,** *1* (1), 83-91.

(39) Ta, C. N.; Liberman, A.; Martinez, H. P.; Barback, C. V.; Mattrey, R. F.; Blair, S. L.; Trogler, W. C.; Kummel, A. C.; Wu, Z. Integrated processing of contrast pulse sequencing ultrasound imaging for enhanced active contrast of hollow gas filled silica nanoshells and microshells. *Journal of Vacuum Science & Technology B* **2012,** *30* (2), 02C104.

(40) Correas, J.-M.; Bridal, L.; Lesavre, A.; Méjean, A.; Claudon, M.; Hélénon, O. Ultrasound contrast agents: properties, principles of action, tolerance, and artifacts. *Eur. Radiol.* **2001,** *11* (8), 1316-1328.
(41) Yildirim, A.; Chattaraj, R.; Blum, N. T.; Goldscheitter, G. M.; Goodwin, A. P. Stable Encapsulation of Air in Mesoporous Silica Nanoparticles: Fluorocarbon-Free Nanoscale Ultrasound Contrast Agents. *Adv. Healthcare Mater.* **2016,** *5* (11), 1290-1298.

(42) Kwan, J. J.; Myers, R.; Coviello, C. M.; Graham, S. M.; Shah, A. R.; Stride, E.; Carlisle, R. C.; Coussios, C. C. Ultrasound-Propelled Nanocups for Drug Delivery. *Small* **2015,** *11* (39), 5305-5314.

(43) Xie, Y.; Wang, J.; Wang, Z.; Krug, K. A.; Rinehart, J. D. Perfluorocarbon-loaded polydopamine nanoparticles as ultrasound contrast agents. *Nanoscale* **2018,** *10* (26), 12813-12819.

(44) Pellow, C.; Goertz, D. E.; Zheng, G. Breaking free from vascular confinement: status and prospects for submicron ultrasound contrast agents. *Wiley Interdisciplinary Reviews: Nanomedicine and Nanobiotechnology* **2018,** *10* (4), e1502.

(45) Beard, P. Biomedical photoacoustic imaging. *Interface Focus* **2011,** *1* (4), 602-631.

(46) Zhang, D.-Y.; Zheng, Y.; Zhang, H.; Sun, J.-H.; Tan, C.-P.; He, L.; Zhang, W.; Ji, L.-N.; Mao, Z.-W. Delivery of Phosphorescent Anticancer Iridium(III) Complexes by Polydopamine Nanoparticles for Targeted Combined Photothermal-Chemotherapy and Thermal/Photoacoustic/Lifetime Imaging. *Adv. Sci.* **2018,** *5* (10), 1800581.

(47) Li, Y.; Jiang, C.; Zhang, D.; Wang, Y.; Ren, X.; Ai, K.; Chen, X.; Lu, L. Targeted polydopamine nanoparticles enable photoacoustic imaging guided chemo-photothermal synergistic therapy of tumor. *Acta Biomater.* **2017,** *47*, 124-134.

Chapter 2   Structure and Function of Iron-Loaded Synthetic Melanin

2.1 Abstract

In this chapter, we describe a synthetic method for increasing and controlling the iron loading of synthetic melanin nanoparticles and use the resulting materials to perform a systematic quantitative investigation on their structure−property relationship. A comprehensive analysis by magnetometry, electron paramagnetic resonance, and nuclear magnetic relaxation dispersion reveals the complexities of their magnetic behavior and how these intraparticle magnetic interactions manifest in useful material properties such as their performance as MRI contrast agents. This analysis allows predictions of the optimal iron loading through a quantitative modeling of antiferromagnetic coupling that arises from proximal iron ions. This study provides a detailed understanding of this complex class of synthetic biomaterials and gives insight into interactions and structures prevalent in naturally occurring melanins.

2.2 Introduction

The natural function and structure inherent to the biomaterial melanin have sparked interest in its utility across a broad range of biomedical applications.[1] Recent work has shown that through the self-oxidation polymerization of dopamine under alkaline conditions, synthetic mimics of natural melanin, with similar chemical structure as well as physical and biological properties, can be achieved.[2-3] These polydopamine (PDA)-based synthetic nanoparticles retain many of the desirable properties of natural melanin and have been studied for use in catalysis,[4] free radical quenching,[2-3] inkjet printing,[5-6] photothermal therapy,[7-8] and structural coloration.[9-10] Many of these applications rely on the strong binding

17

affinity of catechol-based functional groups, allowing robust coordination of various transition metals.[11-13] Despite the proliferation of work in this area, the complex, amorphous nature of the material necessitates a multi-technique approach to elucidate the physical, electronic, and magnetic structure.[3] Herein, we employ a host of complementary techniques to define the properties of synthetic melanin nanoparticles (SMNPs) prepared by a synthetic route that, critically, provides tunability of the Fe(III) content. A similar synthetic method to ours has been described very recently in a report focusing on morphological control in battery applications.[14] Our goal to study the evolution of magnetic and spectroscopic properties led us to focus on a synthetic strategy that provides particles that incorporate a wide range of concentrations of high-spin Fe(III).

Synthetic melanin-based materials are of particular interest as MRI contrast agents due to their excellent biocompatibility and ability to coordinate isolated paramagnetic metal centers.[15-16] The catechol-functionalized network of the nanoparticle acts as a scaffold for chelation of paramagnetic metal ions, leading to T_1-weighted MRI contrast. Although a number of studies have been published on such materials, questions remain about the origin and the path to optimization of the MRI contrast.[3] Our approach initially involved the development of synthetic methods to achieve high metal loadings, as T_1-weighted MRI contrast should scale linearly with the number of isolated paramagnetic centers. The obvious method for preparation of SMNP MRI contrast agents is to expose the already-formed SMNP to a solution containing Fe(III) cations, an approach we term the postdoping synthetic strategy (Figure 1a). The postdoping synthetic strategy is convenient and allows for the complexation of a variety of cations.[17] However, this approach generally limits the metal loading efficiency, which in our hands results in less than 1% iron by mass.[15] Although this situation can be improved somewhat by decreasing the surface-to-volume ratio of SMNPs,[15] [17]achieving ultrahigh, tunable Fe(III) loadings (i.e., >5%) for optimizing and studying the magnetic properties and resulting SMNP-based MRI contrast has remained elusive.
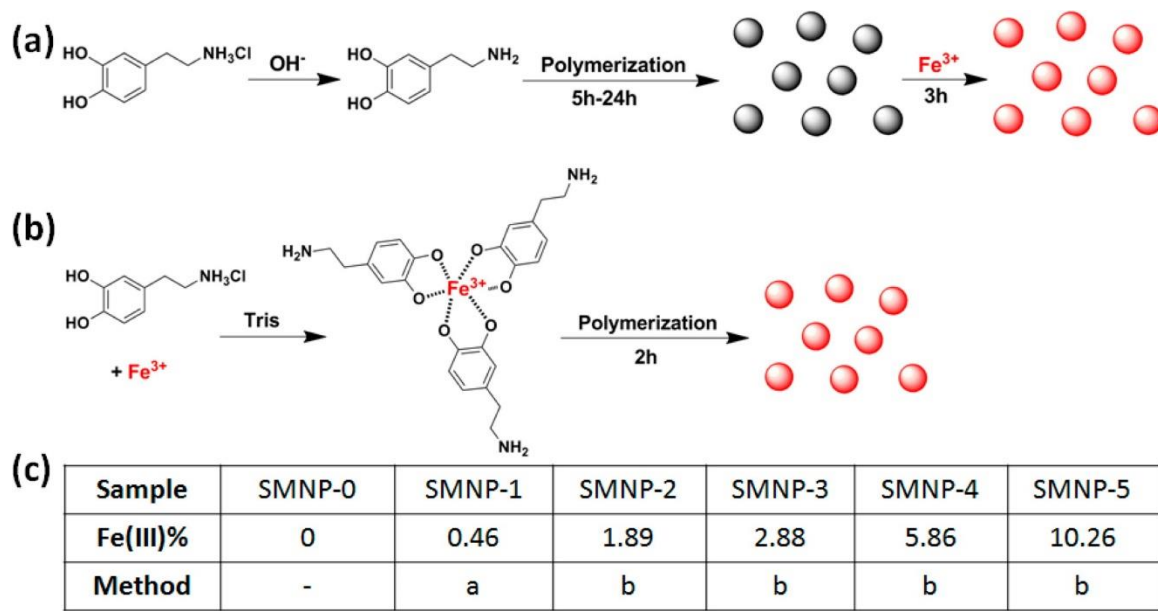
Figure 2.1 Preparation of SMNP-*i* (*i* = 0 - 5) samples: (a) postdoping strategy for SMNP-1, (b) pre-polymerization doping strategy for SMNP-2, SMNP-3, SMNP-4, and SMNP-5, and (c) SMNP-*i* (*i* = 0 - 5) samples with different Fe(III) concentrations. Copyright 2016 American Chemical Society.[18]

Another important question is how water relaxation can occur in a system with strongly chelating catechol units interacting with Fe(III). Considerable insight into the coordination environment of catechol-based materials in general has been gained through electron paramagnetic resonance (EPR) and Mössbauer spectroscopies.[19-23] EPR in particular has given a wealth of data regarding the presence or absence of radical electrons and trace metal ions. However, systems with higher quantities of Fe(III) are difficult to analyze by these techniques due to nonuniform coordination environments and interion magnetic interactions. By contrast, magnetometry excels at the analysis of higher magnetic concentrations and can also reveal details of the local anisotropy and coupling interactions that are vital to understanding the magnetic nature of highly doped materials. Notably, although a variety of analytical methods have been individually employed in characterizing natural melanins,[17, 24-25] a thorough analysis by combined methods allows us to exploit the specific strengths of each technique to understand the coordination environment and magnetic interactions of synthetic mimics of melanin and, in the future, potentially the natural biomaterial itself in all its various forms.

2.3 Results and Discussions

2.3.1 Synthesis and Characterization of SMNPs by Electron Microscopy

To prepare a series of SMNP contrast agents with a broad range of Fe(III) loadings for systematic structure–property relationship analysis, the development of a general Fe(III)-doping strategy to achieve >5% loading was required. This was accomplished through the use of a prepolymerization doping strategy, which employs a mixture of Fe(III)(dopamine)$_3$[26] and free dopamine as the precursors for the formation of Fe(III)-chelated SMNPs (Figure 2.1b). During the polymerization process, in the presence of Tris (Table 2.1),[27] Fe(III) can be continuously incorporated into the SMNP as it forms, allowing tunable, high doping levels of metal ions inside the particle. We have employed this prepolymerization doping strategy (SMNP-*i* (*i* = 2–5), Table 2.1) and the standard postdoping strategy (SMNP-1) to synthesize a series of Fe(III)-doped SMNPs with various Fe(III) concentrations (Table 2.2). Note that Fe(III) loading in SMNP-5 could even reach 10.26%. Additionally, our prepolymerization doping one-pot strategy features several advantages over the postdoping synthetic strategy including efficiency of synthesis, leading to generally higher yield reactions due to less purification work.

Table 2.1 Reactants and their formulations for the preparation of SMNP-*i* (*i* = 2, 3, 4, 5). Copyright 2016 American Chemical Society.[18]

Sample	Dopamine Hydrochloride (mg)	FeCl$_3$•6H$_2$O (mg)	Tris (mg)	Total Water (mL)	pH
SMNP-2	45	0.6	45	150	8.90
SMNP-3	45	1.3	90	150	8.91
SMNP-4	45	6.2	450	150	9.36
SMNP-5	45	20.4	1500	150	9.80

Table 2.2 Physical parameters of SMNP-*i* (*i* = 0-5). Copyright 2016 American Chemical Society.[18]

Sample	Fe(III)%	Size (nm)	Synthetic Strategy
SMNP-0	0	150±25	-
SMNP-1	0.46	150±25	Post-Doping
SMNP-2	1.89	190±20	Pre-Doping
SMNP-3	2.88	170±25	Pre-Doping
SMNP-4	5.86	140±20	Pre-Doping
SMNP-5	10.26	250±30	Pre-Doping

All SMNPs were characterized by transmission electron microscopy (TEM) (Figure 2.2) and scanning electron microscopy (SEM) (Figure 2.3) to quantify their size and uniformity. The combination of TEM, cryo-TEM, and SEM (Figure 2.2, 2.3, 2.4) shows spherical nanoparticles with diameters in the range of 140 to 250 nm (Table 2.2). The presence of metal inside the nanoparticles was evident in the high contrast they exhibit when observed via high-angle annular dark field (HAADF)-STEM and bright-field scanning transmission electron microscopy (BF-STEM) (Figure 2.5). Selected area HAADF-STEM coupled with energy-dispersive X-ray spectroscopy (EDS) further confirms the presence of Fe(III) ions localized in the nanoparticles (Figure 2.6). The EDS profiles suggest that the content of iron in the testing areas of SMNP-4 was significantly higher than that on the grid surface background, which is in good agreement with the elemental mapping analysis results (Figure 2.4). Together, these results strongly suggest that SMNP-*i* (*i* = 0–5) are morphologically similar at the nanoscale, and hence, we expect them to differ only in the average number of unpaired spins imparted by the Fe(III) ion content.
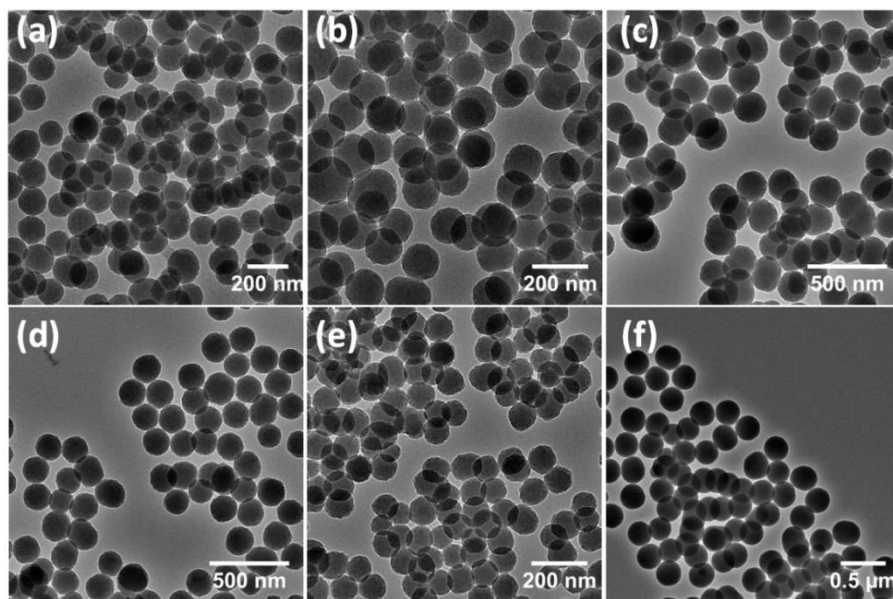
Figure 2.2 Representative TEM images of SMNP-0 (a), SMNP-1 (b), SMNP-2 (c), SMNP-3 (d), SMNP-4 (e), and SMNP-5 (f). Copyright 2016 American Chemical Society.[18]
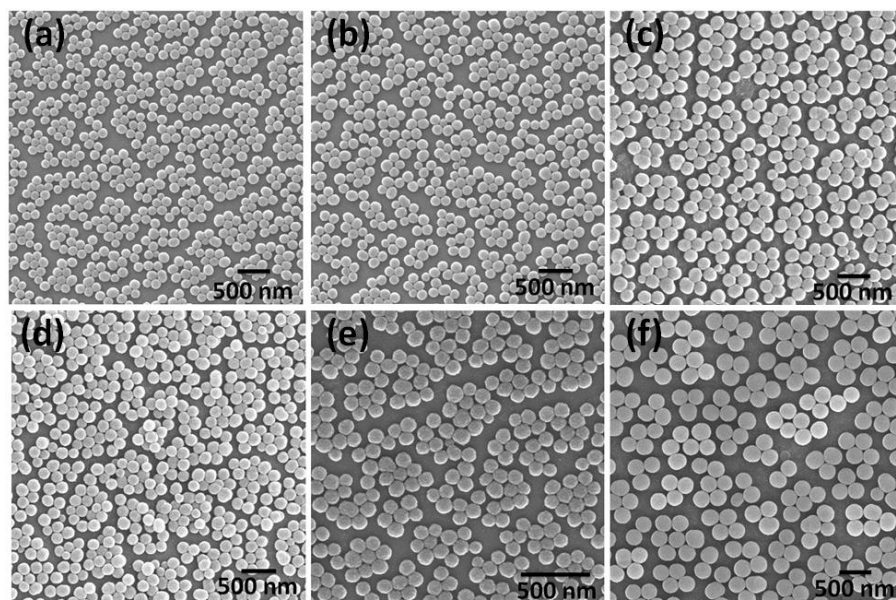
Figure 2.3 Representative SEM images of SMNP-0 (a), SMNP-1 (b), SMNP-2 (c), SMNP-3 (d), SMNP-4 (e), and SMNP-5 (f). Copyright 2016 American Chemical Society.[18]
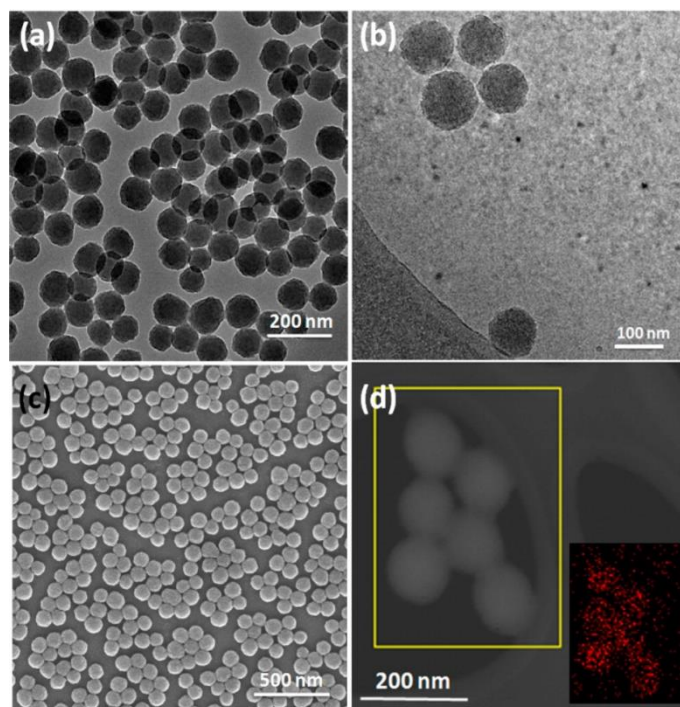
Figure 2.4 Representative electron microscopy characterization of SMNP-4: (a) TEM; (b) cryo-TEM; (c) SEM; and (d) HAADF-STEM (inset is the selected area EDS Fe elemental mapping image). Copyright 2016 American Chemical Society.[18]
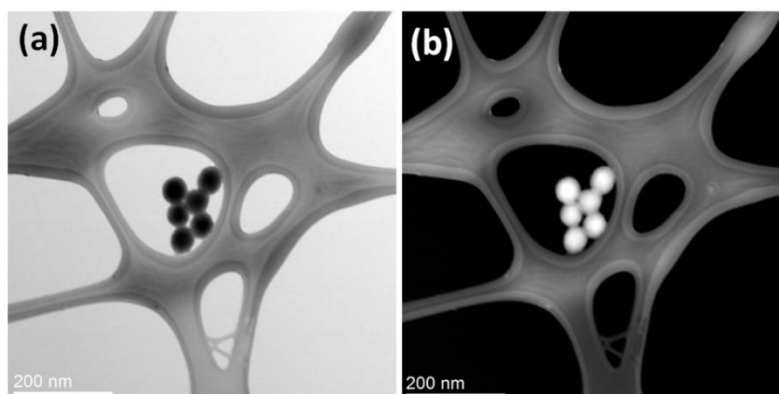
Figure 2.5 (a) BF-STEM and (b) HAADF-STEM images of SMNP-4. Copyright 2016 American Chemical Society.[18]

23
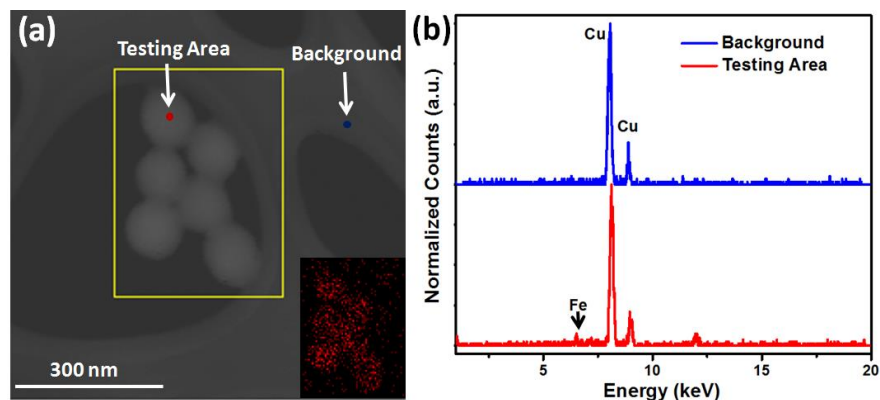
Figure 2.6 (a) HAADF-STEM image of SMNP-4 with the selected area chosen for EDS spectral mapping outlined with a yellow box. Insert in lower right is the EDS Fe elemental mapping image of selected area; (b) EDS spectra of SMNP-4 from the testing area (red) and background (blue) in (a). Copyright 2016 American Chemical Society.[18]

2.3.2 Characterization of SMNPs by NMRD and MR Imaging Analysis

Additional unpaired spins present in the higher Fe(III)-loaded samples should have a strong effect on the relaxometry of proximal solvent protons. This effect, the source of T_1 contrast enhanced MRI, was probed through measurement of the longitudinal water proton relaxation rates (R1) as a function of applied magnetic field for all SMNP samples. 1H nuclear magnetic relaxation dispersion (NMRD) allows an accurate determination of the field dependence of R1 that arises from the magnetic interaction between the metal centers and the solvent.[28-29] This takes place either through chemical exchange between the bound water and the bulk water molecules (inner sphere) or through a long-distance interaction with outer-sphere water molecules that rapidly diffuse near the paramagnetic centers (outer sphere). Shown in Figure 2.7 are the 1H NMRD profiles of SMNP-i (i = 1–5) measured at 298 K in the range 2.3 mT to 1.6 T. The data are expressed in terms of relaxivity, r_{1p}, which is defined as the relaxation rate enhancement induced by 1 mmol/L of the paramagnetic ion. With the exception of the lowest Fe(III)-loading sample, the NMRD profiles of the SMNPs show a similar shape characterized by a low-field plateau (ca. 0.1–1 MHz), followed by a dispersion around ~2–4 MHz and a relatively small increase at frequencies above ca. 30 MHz. The single dispersion displayed at about 3 MHz corresponds to a correlation time $\tau_C \approx 9 \times 10^{-11}$ s. Due to the

slow rotational dynamics (long τ_R values) of paramagnetic centers in these nanoparticles, we attribute this correlation time to the electronic relaxation time τ_S, which has been reported to fall in the range 10^{-11} to 10^{-9} s.[30] The clear increase of r_{1p} above ca. 30 MHz makes it evident that (1) τ_S is field dependent and (2) τ_S represents a predominant factor in the determination of τ_C. This behavior resembles that reported by Bertini et al. in the case of the 1H NMRD profiles of Fe(III) aqua ions in different glycerol–water mixtures.[31] By increasing the viscosity, the relative contribution of τ_R to τ_C with respect to τ_S decreases and the relaxivity in the high-field region increases. The NMRD profile of the iron-binding glycoprotein transferrin shows a similar general trend, although with a more pronounced decrease of r_{1p} with frequency in analogy with that observed for SMNP-1.[32] All these features suggest the presence of one or more water molecules bound to the metal centers (q ≥ 1), at least for a certain population of the Fe(III) centers.
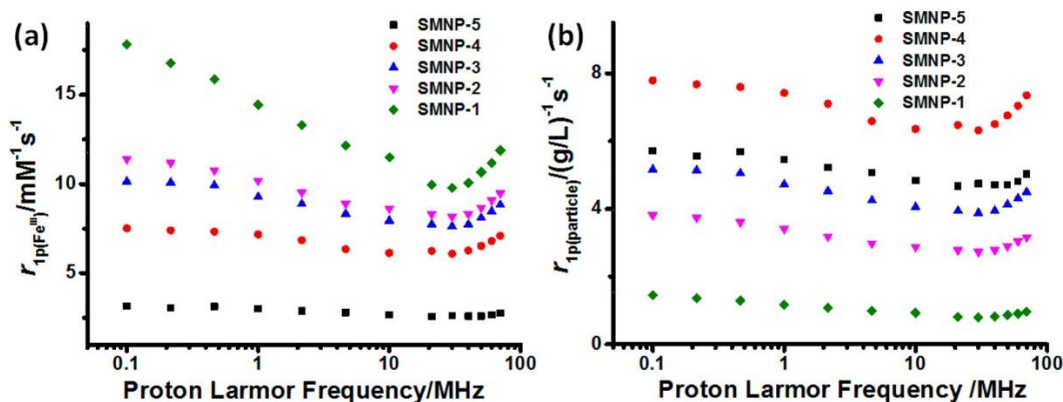
Figure 2.7 (a) ^{1}H NMRD profiles for SMNP-i (i = 1–5). The x-axis is the proton Larmor frequency; the y-axis is the r_{1p} value per Fe(III) ion ($r_{1p(Fe(III))}$) for each SMNP. (b) ^{1}H NMRD profiles for SMNP-i (i = 1–5). The x-axis is the proton Larmor frequency; the y-axis is the r_{1p} value per SMNP ($r_{1p(particle)}$). Copyright 2016 American Chemical Society.[18]

The shape and amplitude of the NMRD profiles suggest various contributions to the relaxivity. The relative complexity of the shape of the profiles reflects the distribution of different populations of species with different coordination environments and thus magnetic properties. The outer-sphere contribution to relaxivity, predominant in the case of tris-catechol-Fe(III) species (q = 0), is generally rather small and can be estimated at approximately 1–2 mM^{-1} s^{-1}.[33] When water is bound to an Fe(III) cation in a macromolecule,

the long exchange lifetime often represents a limiting effect on relaxivity. However, as shown by the case of fluoromethemoglobin,[34] high relaxivity values can be associated with fast exchanging water molecules H-bonded to hydroxide ligands on or next to Fe(III) ions (second-sphere contribution).[34] The dominant role of this mechanism has recently been discussed in the case of polycatechol nanoparticles.[35] All these contributions, with different weights, are likely to play a role in determining the relaxation behavior of these SMNPs.

Since each SMNP can contain many chelated Fe(III) ions, it is interesting to consider the per particle relaxivity ($r_{1p(particle)}$) to describe the local concentration necessary to achieve the desirable T_1 MR imaging contrast under different magnetic fields.[36] Figure 2.7b shows the calculated $r_{1p(particle)}$ of each SMNP. Interestingly, the plots of $r_{1p(particle)}$ and $r_{1p(Fe(III))}$ show different trends (i.e., see Figure 2.8 for $r_{1p(particle)}$ and $r_{1p(Fe(III))}$ results of SMNPs at 20 MHz). Whereas $r_{1p(Fe(III))}$ reveals a diminishing return for additional Fe(III), the plot of $r_{1p(particle)}$ shows there is an upper limiting doping level (i.e., SMNP-4) after which the ^{1}H NMRD shows a decrease in relaxivity over all frequencies. These data lead to the counterintuitive result that highly paramagnetically doped particles are inferior to those doped with lower levels of Fe(III) ions. The origin of this effect will be discussed in subsequent sections.
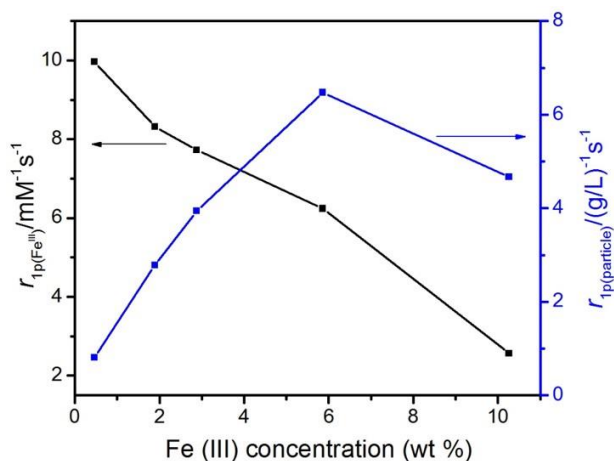
Figure 2.8 Plot of longitudinal relaxivity r_1 nomalized to Fe(III) and particle ($r_{1p(Fe(III))}$ and $r_{1p(particle)}$) versus concentration of Fe(III) at proton Larmor frequency of 20 MHz. Copyright 2016 American Chemical Society.[18]

The long-term stability of any MRI contrast agent in biological fluids is a prerequisite to ensure their *in vitro* and *in vivo* MR imaging performance. Similar to the reported SMNP-1 chelating platform,[37] SMNP-*i* (*i* = 2–5), synthesized via the predoping strategy demonstrate high stabilities (Figure 2.9). Notably, the Fe(III) content of each SMNP remains at approximately 100% of the original value after 1 week of exposure to PBS. Additionally, the long-term MRI signal-enhancing capability of Fe(III)-chelated nanoparticles was tested in a Bruker 7.0 T magnet in different media including water, PBS buffer, fetal bovine serum (FBS), and Dulbecco's modified Eagle medium (DMEM). SMNP-1 and SMNP-4 were selected as samples in this study with SMNP-0 employed as the control. SMNP-1 and SMNP-4 exhibited signal enhancement in T_1-weighted MR images in different media (Figure 2.10). After 5 days of incubation with serum and cell culture medium, the MR images for both SMNP-1 and SMNP-4 samples did not lose intensity, suggesting long-term stability of SMNP agents in biological fluids. Additionally, at the same particle concentration (1.3 mg/mL was used in this study), MR images for SMNP-4 are much brighter than those of SMNP-1 under identical conditions, in good agreement with shorter T_1 relaxation (Figure 2.10). All observations indicate that SMNP-4 enables the best *in vitro* MRI performance at a fixed particle concentration. Subsequently, a systematic study was performed to investigate the long-term MRI contrast-enhancing capability of all SMNP-*i* (*i* = 1–5) samples in different media including water and cell culture media (i.e., 90% DMEM with 10% FBS). It was observed that freshly prepared SMNP-*i* (*i* = 1–5) show similar relaxivity in cell culture medium compared with water (Figure 2.11 and Table 2.3). In addition, we note that after 5 days of incubation with cell culture medium, the relaxivity values for all SMNP samples do not decrease, confirming the materials are promising in terms of long-term stability of SMNP MRI agents in biological fluids.

27
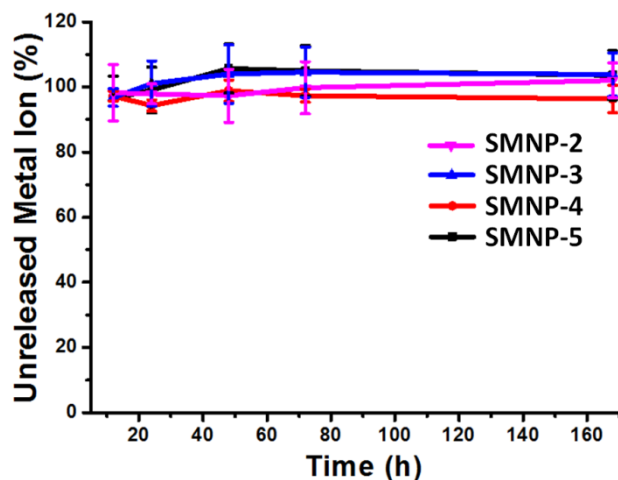
Figure 2.9 Stability study of Fe(III)-chelated SMNP-*i* (*i*=2-5) in PBS. Copyright 2016 American Chemical Society.[18]
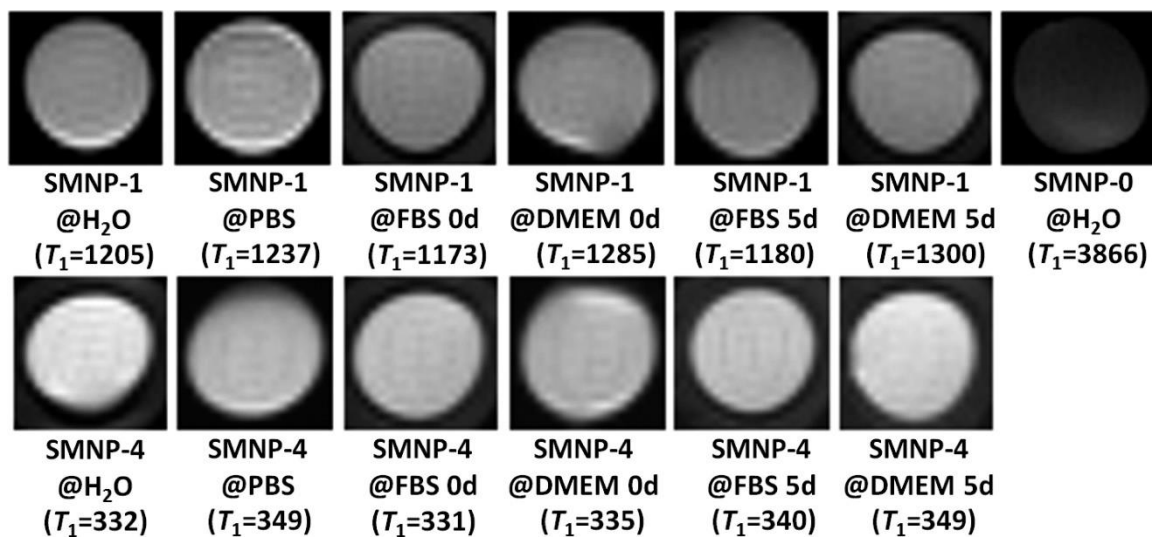
Figure 2.10 T_1-weighted MR images captured on a Bruker 7.0 T magnet from SMNP-0, SMNP-1, and SMNP-4 in different media (particle concentration is 1.3 mg/mL in each tube). T_1 results for each phantom are shown below in milliseconds, respectively. Copyright 2016 American Chemical Society.[18]

28
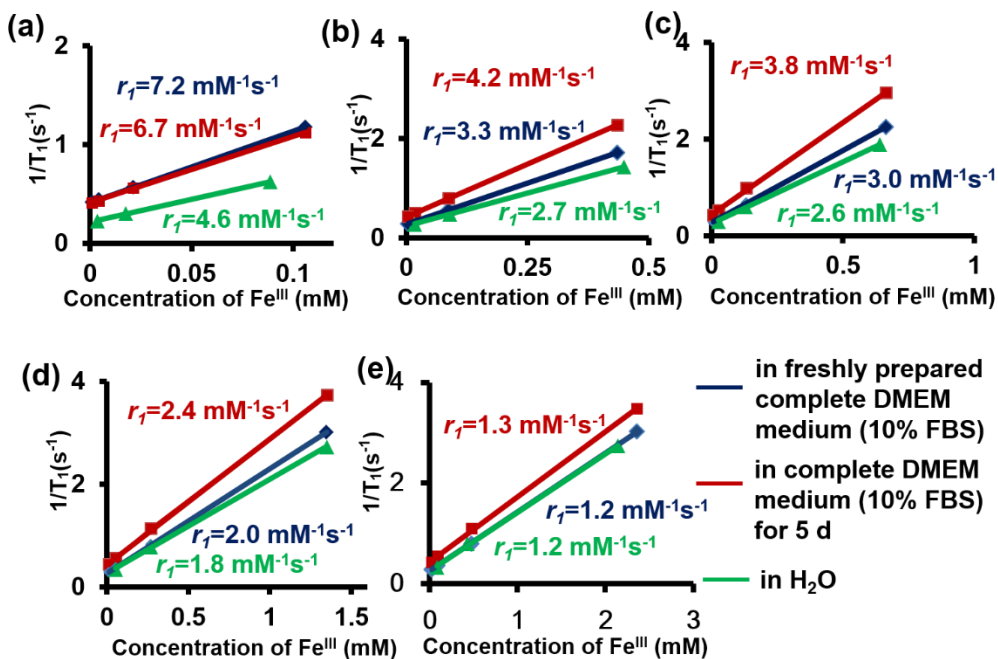
Figure 2.11 MRI characterization of SMNP-*i* (*I* = 1-5) nanoparticles on a Bruker 7.0 T magnet. Plots of $1/T_1$ versus Fe(III) concentration for SMNP-*i* in different medium with calculated r_1 (green: SMNP-*i* in water, blue: SMNP-*i* in freshly prepared complete DMEM medium (10% FBS), red: SMNP-*i* in complete DMEM medium (10% FBS) for 5 d). (a) SMNP-1, (b) SMNP-2, (c) SMNP-3, (d) SMNP-4, and (e) SMNP-5. Copyright 2016 American Chemical Society.[18]

Table 2.3 r_1 result for each sample shown in Figure 2.11

Sample	r_1 (mM^{-1}s^{-1})	Sample	r_1 (mM^{-1}s^{-1})	Sample	r_1 (mM^{-1}s^{-1})
SMNP-1@H$_2$O	4.6	SMNP-1@DMEM 0d	7.2	SMNP-1@DMEM 5d	6.7
SMNP-2@H$_2$O	2.7	SMNP-2@DMEM 0d	3.3	SMNP-2@DMEM 5d	4.2
SMNP-3@H$_2$O	2.6	SMNP-3@DMEM 0d	3.0	SMNP-3@DMEM 5d	3.8
SMNP-4@H$_2$O	1.8	SMNP-4@DMEM 0d	2.0	SMNP-4@DMEM 5d	2.4
SMNP-5@H$_2$O	1.2	SMNP-5@DMEM 0d	1.2	SMNP-5@DMEM 5d	1.3

2.3.3 Magnetochemical Analysis of SMNPs

Several intriguing questions arise from the relaxivity data: (1) Is the T_1 contrast arising from an inner-sphere binding event, despite the propensity for catechol to form strong tris-chelates in neutral and basic solutions? (2) Why is there not a linear increase in the relaxivity response with additional Fe(III) cations, as would be expected for T_1 contrast? To address these questions directly, we turned to techniques that are sensitive to the local spin states as well as the ensemble properties of the magnetic structure.

EPR spectra of frozen solutions were collected at 125 K (Figure 2.12), providing significant information regarding the distribution of radicals within Fe(III)-loaded SMNPs.[38] The characteristic spectrum of the persistent radical, which is a hallmark of all melanins, is visible in samples with less than 2% iron. As reported, paramagnetic metals can reduce the amplitude of this peak,[39] completely suppressing it at high loadings. All iron-containing samples show a peak at 1600 G (g = 4.3), which is attributed to high-spin Fe(III) in sites of low symmetry of tetrahedral or octahedral coordination.[17] The width of this peak

increases with increased iron loading due to spin–spin dipolar coupling.[40] From these data, we determined the change in the full width at half-maximum as a function of total iron, with the linear progression suggesting that the iron loading is evenly distributed in a 3-D matrix of sites, as opposed to either lower dimensional arrangements or clusters (Figure 2.13).[41]
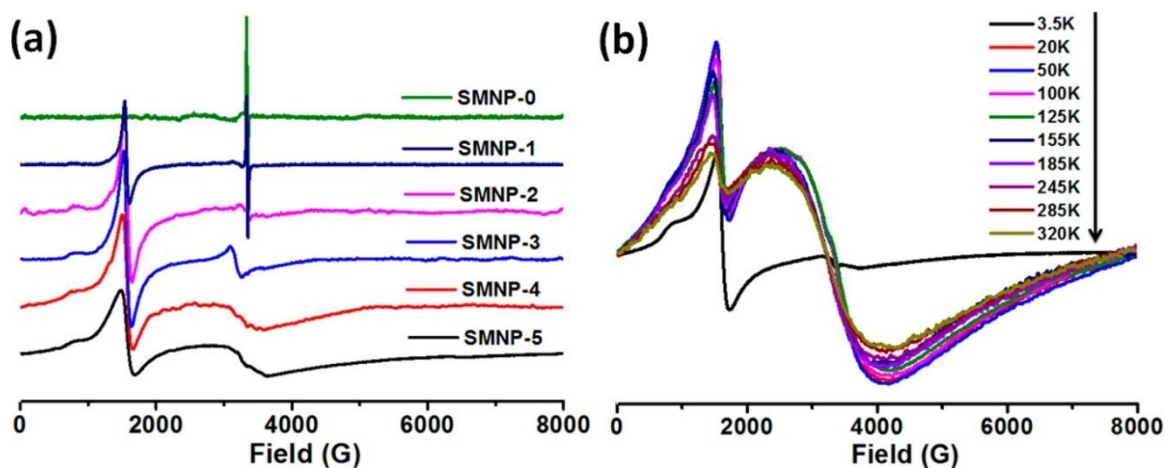
Figure 2.12 (a) Experimental EPR spectra of SMNP-i (i = 0–5). (b) Temperature-dependent EPR analysis of SMNP-5. Copyright 2016 American Chemical Society.[18]

At the highest iron loading levels, a very broad spectrum centered near $g = 2$ is evident. In many systems, a spectrum of this form is due to superparamagnetic or ferromagnetic particles. Therefore, the spectrum of SMNP-5 was recorded over a wide range of temperatures to explore the magnetic properties of this species (Figure 2.12b).[42] However, unlike a ferromagnetic material, which would have a constant intensity, or a superparamagnetic material, which would have spectra that would broaden and shift to lower field as the temperature is lowered, the spectra increase in amplitude as the temperature is lowered to 20 K, but then sharply diminish in amplitude at 3.5 K. This behavior indicates the occurrence of a more complex magnetic behavior that gains in strength with increasing Fe(III) loading.
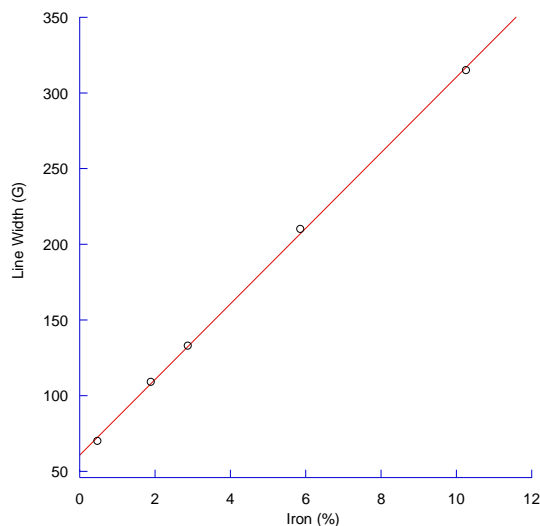
Figure 2.13 Line width of g = 4.3 EPR spectrum as a function of iron. Black circles, line width from data acquired at 125 K. Red line is first order fit of data showing that line width increases linearly with iron content. Copyright 2016 American Chemical Society.[18]

To elucidate the origin of this alteration in the magnetic structure at high Fe(III) cation concentrations, the temperature dependence of the SMNP magnetic susceptibility was investigated by superconducting quantum interference device (SQUID) magnetometry (Figure 2.14). The lowest Fe-loading sample (SMNP-1) was expected to largely exhibit characteristics of the isolated octahedral high-spin d^5 configuration of Fe(III) (S = 5/2) as demonstrated by the EPR data. Indeed, the product of magnetic susceptibility and temperature per mole Fe ($\chi_M T$) at 300 K approaches the expected spin-only value of 4.375 emu K cm^{-3} mol^{-1} for a purely Fe(III)-containing sample. This close agreement precludes the possibility of significant Fe(II) and low-spin Fe(III) populations, as they would lead to significant alterations in the $\chi_M T$ value. As temperature is decreased from 300 K, the effects of antiferromagnetic Fe(III)–Fe(III) interactions begin to manifest in the $\chi_M T$ data. For SMNP-1 with only 0.46% Fe(III) loading, the majority of Fe(III) centers are sufficiently isolated so as to display their full, uncoupled moment. However, a non-negligible subset of Fe(III) are close to other Fe(III) sites and thus display antiferromagnetic interactions that lower the overall $\chi_M T$ value. As we increase the Fe(III) concentration up to 10.26% (SMNP-5),

32

deviations from the spin-only expectation become more drastic, leading to a drop of more than 20% in the

$\chi_M T$ product at room temperature.
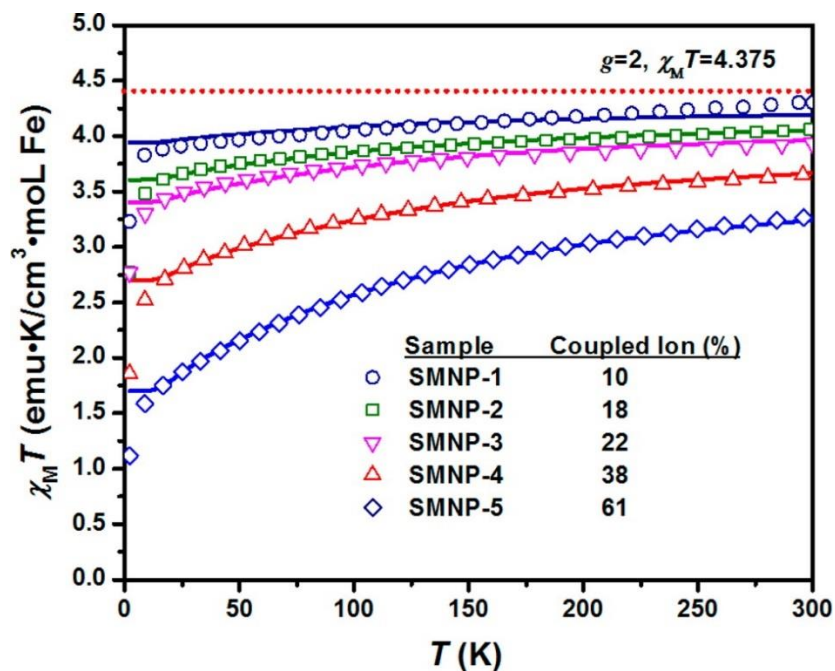
Figure 2.14 Temperature dependence of the product of magnetic susceptibility and temperature ($\chi_M T$) for SMNP-*i* (*i* = 1–5). The dotted line describes the behavior of an isolated, isotropic Fe(III) ion. Solid lines represent a global fit of the data between 25 and 300 K as described in the text. Copyright 2016 American Chemical Society.[18]

We find that a relatively simple model, incorporating an isotropic *g* value and magnetic coupling constant ($J_{Fe–Fe}$), is able to satisfactorily explain the coupling behavior of Fe(III). In this model, we need only consider two general types of Fe(III) centers: magnetically isolated Fe(III) and magnetically coupled Fe(III). This assumption is based on the weak superexchange pathway that the catechol functional groups of PDA provide. Indeed, model molecular Fe(III) catecholate dinuclear complexes display coupling constants of less than 30 cm^{-1}, even when only separated by a single catecholate oxygen.[43-45] The ratio between the uncoupled and coupled Fe(III) subsets is fitted along with an isotropic *g* and $J_{Fe–Fe}$ value by simultaneous global fitting of all susceptibility data. Uncoupled Fe(III) is modeled as an ideal paramagnetic *S* = 5/2 Fe(III), whereas coupled Fe(III) is modeled through an HDVV Hamiltonian (Eq 1) where $\hat{S}_1$ and $\hat{S}_2$ are spin operators for equivalent interacting spins. Although most natural and synthetic

melanin systems have been shown to possess some radical electron character,[3, 46-47] we do not find it necessary to include radical electrons in our model. This is corroborated by measuring magnetic susceptibility of equivalently synthesized pure melanin nanoparticles (SMNP-0) without Fe(III) loading, which shows a negligible paramagnetic moment across all temperatures (Figure 2.15). This does not imply that no radical population is present, only that it is necessarily low enough to be inconsequential to the overall magnetism. In fact, EPR spectra (Figure 2.12) confirm the presence of organic radicals in SMNP-0 and SMNP-1.

$$\hat{H} = -2J_{Fe-Fe}\,\hat{S}_1 \cdot \hat{S}_2 \qquad\qquad (Eq\ 1)$$
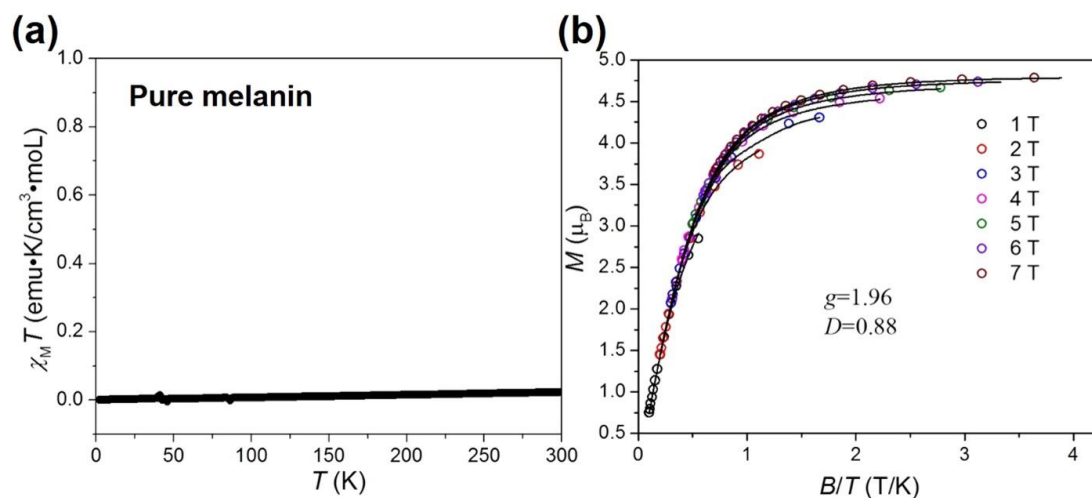
Figure 2.15 (a) Plot of the product of temperature and magnetic susceptibility vs. temperature ($\chi_M T$) for SMNP-0. (b) Low-temperature magnetization data under different applied fields for SMNP-1. The black lines represent fits to data. Copyright 2016 American Chemical Society.[18]

The fitting results reveal antiferromagnetic coupling ($g = 2.05 \pm 0.04$; $J_{Fe-Fe} = -24.8 \pm 2.7$ cm^{-1}) that corresponds well to molecular Fe-catechol systems.[43, 48-49] Of particular note is that at very high Fe(III) loadings (SMNP-5) over half of the Fe(III) is now involved in magnetic coupling interactions, leading to a significant drop in the moment even under ambient temperature conditions. This behavior tracks well with the low $r_{1p(Fe(III))}$ of the SMNP-5 sample (Figure 2.7a). From the view of MRI contrast agents, this antiferromagnetic coupling tempers the advantage of high loading because of the significant reduction in

34

room-temperature moment per iron center compared with less concentrated Fe(III) samples. Additionally, the magnetically coupled Fe(III)–Fe(III) interactions can alter the nature of the relaxation, shifting of the SMNP toward T_2-weighted agents at high concentrations. These factors indicate that there will be an optimal Fe(III) concentration. This relatively strong coupling also indicates that short Fe(III)–Fe(III) ligand-based bridges can exist within the PDA structure, an intriguing result considering that mononuclear molecular Fe(III)-catechol exists as a mixture of bis- and tris-catechol-Fe(III) species at our synthetic conditions (pH ~9). Since a tris-catechol binding mode would inhibit the formation of effective superexchange bridges, the strength of coupling we observe may indicate a low catechol coordination number for Fe(III) within the SMNP. If in fact, the PDA structure is limiting the catechol coordination, this opens the exciting possibility that water is able to directly bind to Fe(III) centers or interact with hydroxides directly bound to Fe(III) centers, thus explaining the strong MRI contrast observed for Fe(III)-coordinated synthetic melanin.[15]

Further evidence of limited Fe-catechol bonding was obtained by scrutinizing the deviations from ideal paramagnetic behavior observed at very low temperature. These deviations are caused by magnetic anisotropy induced by a low-symmetry coordination environment as well as Zeeman splitting due to the applied field. To isolate the effects of the magnetic anisotropy, we performed a series of low-temperature, variable-field measurements for SMNP-1, which has the lowest amount of coupled Fe(III) (Figure 2.16a). We focus on SMNP-1 because 90% of the Fe(III) is in the uncoupled state, and the magnetic influence of the remaining 10% is minimized due to its relative isolation in the antiferromagnetically coupled ($S = 0$) state at low temperature. Under these approximations, the molar magnetization values in Figure 2.16a are solely due to uncoupled Fe(III) ions. By fitting to an axially anisotropic Hamiltonian (Eq 2) using the MagProp module of DAVE 2.3 (Figure 2.16),[50] a small but non-negligible axial anisotropy is determined to be present ($D = 0.88 \pm 0.29$). Interestingly, this value corresponds to that observed for monocatechol-bound Fe(III) in acidic aqueous solution ($D = 0.82$), but is significantly higher than the bis- and tris-catechol-bound Fe(III) ($D = 0.42$ and $D = 0.32$, respectively).[21] High Fe(III) concentration samples

(SMNP-2 through SMNP-5) gave similar results although with less satisfactory error values due to the

added complication of large contributions from coupled Fe(III) (Figure 2.17).

$$\hat{H} = g\mu_B \hat{S} \cdot B + D[\hat{S}_z^2 - \frac{S(S+1)}{3}]$$ (Eq 2)
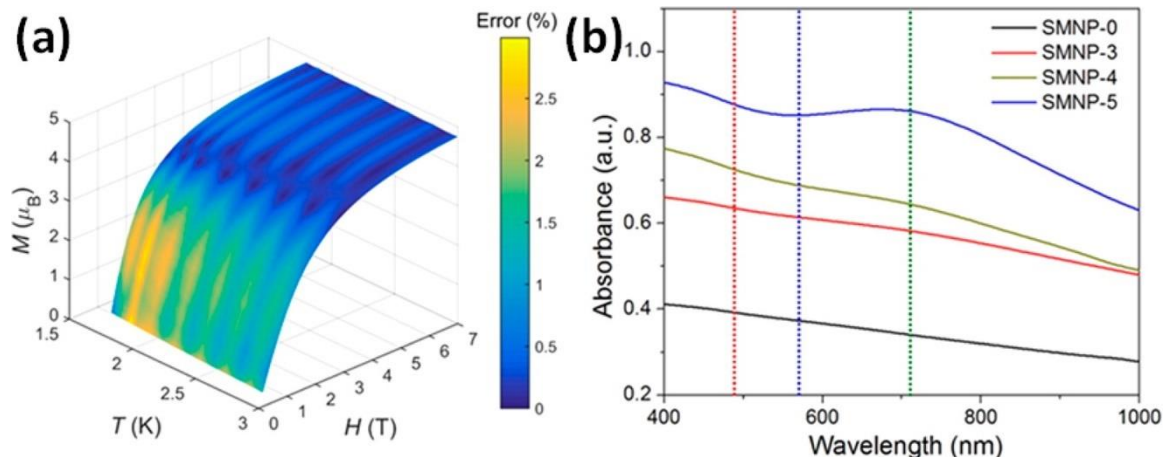
Figure 2.16 (a) Plot of variable-temperature variable-field magnetization data for SMNP-1. The color bar represents the difference between experimental data and fitting results. A standard 2D M vs H/T plot is shown in Figure 2.14b. (b) UV–vis spectra of 0.1 mg/mL SMNP showing the transition from a featureless absorption for SMNP-0 to a well-defined yet broad structure in SMNP-5. Absorption peaks for mono-($\sim$710 nm), bis- ($\sim$570 nm), and tris-catechol ($\sim$490 nm) are identified by dashed green, blue, and red lines, respectively. Copyright 2016 American Chemical Society.[18]
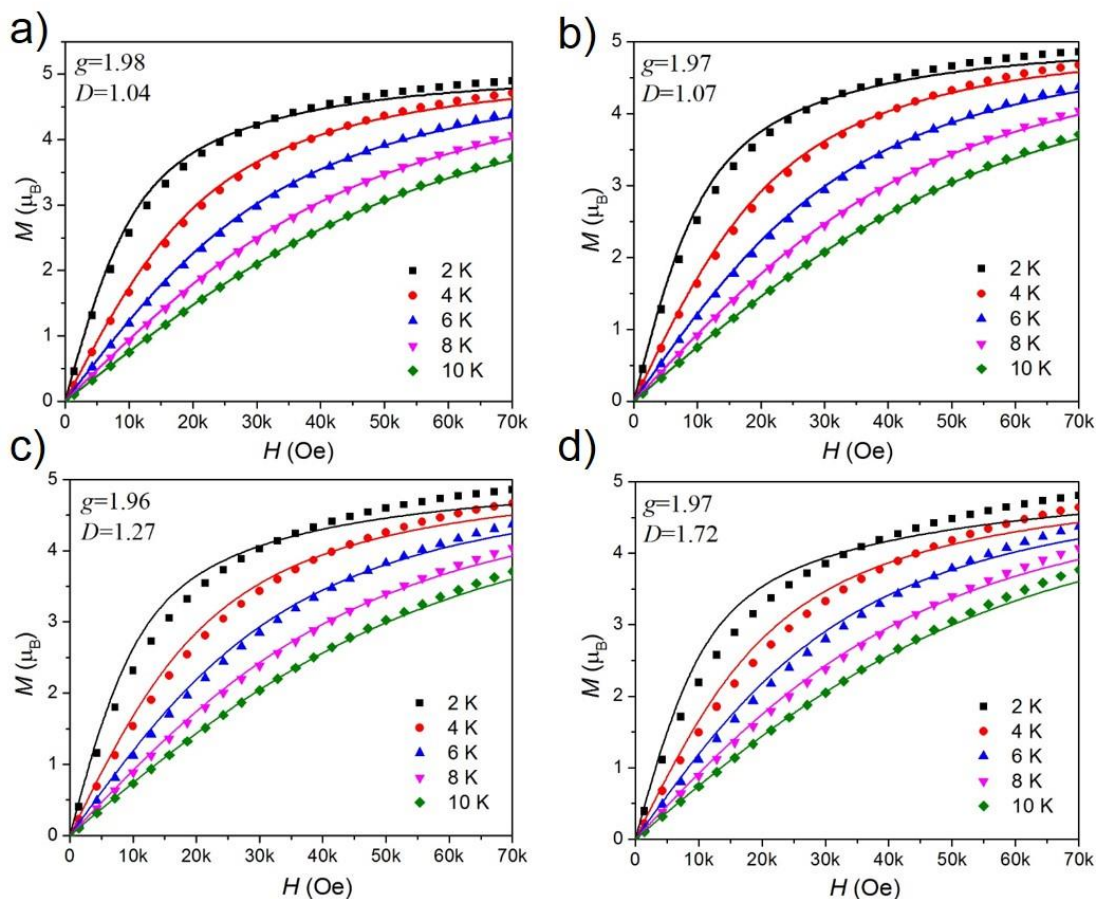
Figure 2.17 Low-temperature magnetization data under different applied fields for (a) SMNP-2; (b) SMNP-3; (c) SMNP-4; (d) SMNP-5. The black lines represent fits to data. Copyright 2016 American Chemical Society.[18]

The magnetic evidence strongly suggests that despite the high concentration of catechol in SMNP materials and pH values during synthesis that should initially favor a tris-catechol binding mode, Fe(III) is largely coordinated as the monocatechol in the final product. As this result was somewhat counterintuitive, UV–vis spectroscopy was employed to corroborate our magnetic analysis. Figure 2.16b shows that both high (SMNP-5) and low (SMNP-3) Fe(III) loadings exhibit a broad peak at 710 nm, which is indicative of monocatechol-Fe(III) complexes.[20, 51-52] In stark contrast to previously studied free Fe(III) catechol systems,[51-52] this peak persists even at very basic pH values for 24 h with no indication of bis- or tris-catechol formation (Figure 2.18). These data suggest that melanin-based MRI contrast agents may allow

for water exchange through an "inner-sphere" T_1 relaxation, even for Fe(III) embedded within the nanoparticle.[15, 53]
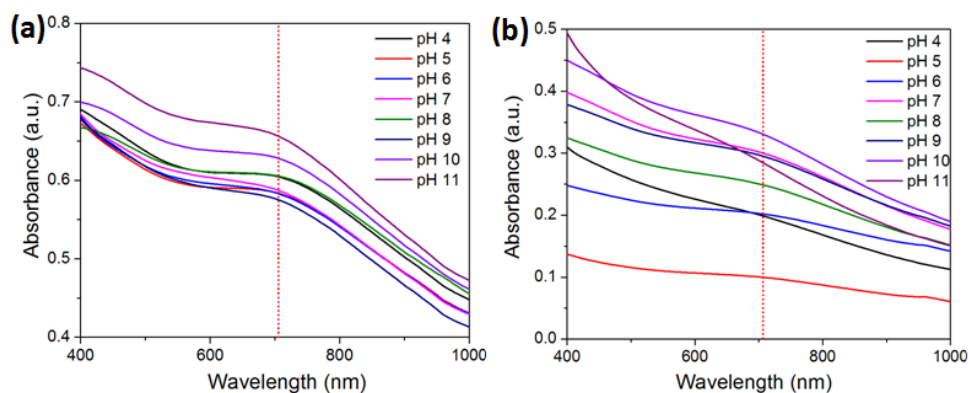
Figure 2.18 UV-vis spectra of 0.1 mg/mL SMNP-5 suspended in water at a pH of 4 to 11. Spectra collected (a) 5 min and (b) 24 h after pH change. Copyright 2016 American Chemical Society.[18]

From the combination of magnetometry and magnetic spectroscopy (EPR) we can conclude that isolated paramagnetic iron centers exist throughout the SMNPs. At higher concentrations, the Fe(III) does not form oxide particles that would show ordered magnetic behavior but does form weak antiferromagnetic superexchange interactions that effectively cancel out a significant portion of the 300 K magnetization. Additionally, the high magnetic anisotropy indicates a low-symmetry environment that is not consistent with tris-catechol coordination of Fe(III); thus the superexchange is likely mediated by diamagnetic bridging ligands and not the polymer backbone.

2.4 Experimental Section

2.4.1 Particle Synthesis and Characterization

All chemicals were purchased from Sigma-Aldrich and used without further purification. SMNP-0 and SMNP-1 were prepared according to a literature method.[15]

General synthetic method for SMNP-*i* (*i* = 2, 3, 4, 5) (prepolymerization doping strategy): 45 mg of dopamine hydrochloride and different amounts of iron(III) chloride hexahydrate were fully dissolved in 130 mL of deionized water under stirring at room temperature for 1 h. Subsequently, 20 mL of Tris (2-amino-2-hydroxymethylpropane-1,3-diol) aqueous solution (with varying Tris concentrations, Table 2.1) was quickly injected into the established solution. It was observed that the solution color immediately turned red, gradually turning black after 0.5 h. After another 1.5 h, the targeted SMNP-*i* was separated by centrifugation and washed three times with deionized water.

TEM was performed on a FEI Sphera microscope operating at 200 keV. TEM grids were prepared by depositing small (3.5 μL) aliquots of sample onto grids (~2 min, Formvar stabilized with carbon (5–10 nm) on 400 copper mesh, Ted Pella Inc.) that had previously been glow discharged using an Emitech K350 glow discharge unit and plasma-cleaned for 90 s in an E.A. Fischione 1020 unit. Micrographs were recorded on a 2 K x 2 K Gatan CCD camera.

Cryo-TEM experiments were also performed on a FEI Sphera microscope operating at 200 keV. TEM grids were prepared by depositing small (3.5 μL) aliquots of sample onto grids (Quantifoil R2/2 holey carbon) that had previously been glow discharged using an Emitech K350 glow discharge unit and plasma-cleaned for 90 s in an E.A. Fischione 1020 unit. Samples were loaded onto the grids at 4 °C, blotted with filter paper to create a thin film on the grid, plunged into liquid ethane, and transferred into a precooled Gatan 626 cryo-transfer holder, which maintained the specimen at liquid-nitrogen temperature in a FEI Sphera microscope operated at 200 kV. Micrographs were recorded on a 2 K × 2 K Gatan CCD camera.

STEM and STEM-EDS analyses were acquired on a JEOL JEM 2100F TEM equipped with an INCA (Oxford) EDS detector at the NanoScale Fabrication and Characterization Facility, Peterson Institute of Nanoscience and Engineering, University of Pittsburgh, PA. Samples were prepared by drop-casting 5 μL of sample onto TEM grids (ultrathin 5 nm A-type carbon with 400 mesh copper, Ted Pella, Inc.) followed by slow drying while covered on the benchtop for at least 3 h. Samples were then dried under

vacuum for 24–48 h to remove contamination that would interfere with STEM-EDS. Grids were loaded into a JEOL 31640 beryllium double-tilt holder. STEM-EDS data were collected for 180–600 s at specific points, using the largest probe size (1.5 nm electron beam diameter) with a 200 kV accelerating voltage. Images were collected in bright field and HAADF modes.

SEM images were acquired on a FEI XL ESEM-FEG (FEI Company) with a mica substrate. Samples were fully dried under vacuum for 12 h before the testing.

UV–vis spectra were obtained by using a PerkinElmer Lambda 35 UV/vis spectrophotometer.

2.4.2   Determination of Fe(III) Concentration

In order to determine Fe(III) concentration, the metal was first stripped from the synthetic melanin particles using the following procedure. To an aliquot of each sample (100 μL) was added 1% HNO_3 in water (1900 μL). Each mixture was then stirred for 12 h. The Fe(III) concentration was then quantified by inductively coupled plasma-optical emission spectrometry (ICP-OES) using a PerkinElmer Optima 3000DV spectrometer in the Scripps Institution of Oceanography, University of California, San Diego, CA.

2.4.3   SQUID Measurements

The magnetic properties of SMNP were characterized using a Quantum Design MPMS3 SQUID with a maximum field of 7 T. Freeze-dried solid samples (∼10 mg) were packed into standard Quantum Design plastic sample holders. Magnetization data were collected in dc mode and corrected for diamagnetic contributions using Pascal's constants. The axial anisotropy parameter D was fitted by the MagProp module in DAVE 2.3.[50]

2.4.4   EPR Experiments

Spectra in the range of 125 to 320 K were acquired on a Bruker Elexsys 580 spectrometer equipped with an SHQE resonator and a Bruker continuous flow liquid nitrogen cryostat. Spectra at temperatures

between 3.5 and 125 K were acquired on a Bruker EMX spectrometer using an ER 4116DM dual-mode resonator and an Oxford ESR910 helium continuous flow cryostat. Liquid samples for frozen solution experiments were loaded in 4 mm o.d. × 3 mm i.d. FEP tubes (Wilmad). Room-temperature liquid samples were contained in 1.8 mm o.d. × 1 mm i.d. Teflon tubing (McMaster-Carr), while powder samples were contained in traditional 4 mm o.d. × 3 mm i.d. quartz tubes (Wilmad). Microwave frequency was typically ~9.34 GHz (SHQE resonator) with a power of 20 mW. The field was swept from 0 to 8000 G in 168 s and modulated at a frequency of 100 kHz with 20 G amplitude. A time constant of 82 ms was employed.

2.4.5   1H NMRD Measurements

Proton $1/T_1$ NMRD profiles were measured on a fast field-cycling Stelar SMARTracer Relaxometer (Stelar, Mede (PV), Italy) at magnetic field strengths from 0.00024 to 0.25 T (corresponding to 0.01–10 MHz proton Larmor frequencies) at room temperature. The relaxometer operates under computer control with an absolute uncertainty in $1/T_1$ of ±1%. Additional data points in the range 15–70 MHz were obtained on a Bruker WP80 NMR electromagnet adapted to variable-field measurements (15–80 MHz proton Larmor frequency) on a Stelar Relaxometer. The ^{1}H T_1relaxation times were acquired by the standard inversion recovery method with a typical 90° pulse width of 3.5 μs, 16 experiments of 4 scans. The temperature was controlled with a Stelar VTC-91 airflow heater equipped with a calibrated copper–constantan thermocouple (uncertainty of ±0.1 °C).

2.4.6   Fe(III) Stability in PBS

To determine the stability of Fe(III) chelated in SMNP-i (i = 2–5), we redispersed these two types of nanoparticles in PBS (pH = 7.4). A 300 μL amount of SMNP-i (i = 2–5) solution (three replicates) was added in 500 μL dialysis tubes with M_w = 10 000, respectively, and dialyzed to 500 mL of PBS (pH = 7.4) under room temperature with magnetic stirring. Then 20 μL SMNP-i (i = 2–5) aliquots were taken at time points of 8 h, 24 h, 48 h, 72 h, and 7 days for ICP-OES analysis.

2.4.7   MR Imaging Measurements

The MR images were acquired on a Bruker 7.0 T magnet with Avance II hardware equipped with a 72 mm quadrature transmit/receive coil. T_1 contrast was determined by selecting regions of interest using the software ParaVision version 5.1. The parameters for 7 T MRI are T_R = 750.0 ms, T_E = 12.6 ms, echo = 1/1, FOV = 6.91/3.12 cm, slice thickness = 2 mm, nex = 2 mm, matrix = 256 × 116.

2.5 Conclusion

in summary, a technique for accessing SMNPs with tunable iron loadings has offered opportunity for their magnetostructural analysis through the combined utilization of SQUID magnetometry, EPR, and ^{1}H $1/T_1$ NMRD. The results presented herein also suggest a number of avenues for optimizing MRI contrast in synthetic melanin nanoparticles. With the current interest in metal-doped melanin and polycatechol-based nanomaterials, a fundamental understanding of the electronic and magnetic structure is vital. The conclusions herein offer potential synthetic targets that could lead to more directed syntheses of effective contrast agents. More broadly, these combined characterization tools should provide insight into natural melanins and, therefore, any potential differences or similarities between their various forms and their synthetically accessible mimics.

2.6 Acknowledgement

2.7 References

(1) d'Ischia, M.; Napolitano, A.; Ball, V.; Chen, C.-T.; Buehler, M. J. Polydopamine and Eumelanin: From Structure–Property Relationships to a Unified Tailoring Strategy. *Acc. Chem. Res.* **2014,** *47* (12), 3541-3550.

(2) Ju, K.-Y.; Lee, Y.; Lee, S.; Park, S. B.; Lee, J.-K. Bioinspired Polymerization of Dopamine to Generate Melanin-Like Nanoparticles Having an Excellent Free-Radical-Scavenging Property. *Biomacromolecules* **2011,** *12* (3), 625-632.

(3) Liu, Y.; Ai, K.; Lu, L. Polydopamine and Its Derivative Materials: Synthesis and Promising Applications in Energy, Environmental, and Biomedical Fields. *Chem. Rev.* **2014,** *114* (9), 5057-5115.
(4) Ai, K.; Liu, Y.; Ruan, C.; Lu, L.; Lu, G. Sp2 C-Dominant N-Doped Carbon Sub-micrometer Spheres with a Tunable Size: A Versatile Platform for Highly Efficient Oxygen-Reduction Catalysts. *Adv. Mater.* **2013,** *25* (7), 998-1003.

(5) Ma, S.; Liu, L.; Bromberg, V.; Singler, T. J. Electroless Copper Plating of Inkjet-Printed Polydopamine Nanoparticles: a Facile Method to Fabricate Highly Conductive Patterns at Near Room Temperature. *ACS Appl. Mater. Interfaces* **2014,** *6* (22), 19494-19498.

(6) Ma, S.; Liu, L.; Bromberg, V.; Singler, T. J. Fabrication of highly electrically conducting fine patterns via substrate-independent inkjet printing of mussel-inspired organic nano-material. *J. Mater. Chem. C* **2014,** *2* (20), 3885-3889.

(7) Liu, Y.; Ai, K.; Liu, J.; Deng, M.; He, Y.; Lu, L. Dopamine-Melanin Colloidal Nanospheres: An Efficient Near-Infrared Photothermal Therapeutic Agent for In Vivo Cancer Therapy. *Adv. Mater.* **2013,** *25* (9), 1353-1359.

(8) Stritzker, J.; Kirscher, L.; Scadeng, M.; Deliolanis, N. C.; Morscher, S.; Symvoulidis, P.; Schaefer, K.; Zhang, Q.; Buckel, L.; Hess, M.; Donat, U.; Bradley, W. G.; Ntziachristos, V.; Szalay, A. A. Vaccinia virus-mediated melanin production allows MR and optoacoustic deep tissue imaging and laser-induced thermotherapy of cancer. *Proceedings of the National Academy of Sciences* **2013,** *110* (9), 3316.

(9) Xiao, M.; Li, Y.; Allen, M. C.; Deheyn, D. D.; Yue, X.; Zhao, J.; Gianneschi, N. C.; Shawkey, M. D.; Dhinojwala, A. Bio-Inspired Structural Colors Produced via Self-Assembly of Synthetic Melanin Nanoparticles. *ACS Nano* **2015,** *9* (5), 5454-5460.

(10) Xiao, M.; Li, Y.; Zhao, J.; Wang, Z.; Gao, M.; Gianneschi, N. C.; Dhinojwala, A.; Shawkey, M. D. Stimuli-Responsive Structurally Colored Films from Bioinspired Synthetic Melanin Nanoparticles. *Chem. Mater.* **2016,** *28* (15), 5516-5521.

(11) Krogsgaard, M.; Behrens, M. A.; Pedersen, J. S.; Birkedal, H. Self-Healing Mussel-Inspired Multi-pH-Responsive Hydrogels. *Biomacromolecules* **2013,** *14* (2), 297-301.

(12) Li, L.; Smitthipong, W.; Zeng, H. Mussel-inspired hydrogels for biomedical and environmental applications. *Polym. Chem.* **2015,** *6* (3), 353-358.

(13) Guo, L.; Liu, Q.; Li, G.; Shi, J.; Liu, J.; Wang, T.; Jiang, G. A mussel-inspired polydopamine coating as a versatile platform for the in situ synthesis of graphene-based nanocomposites. *Nanoscale* **2012,** *4* (19), 5864-5867.

(14) Ang, J. M.; Du, Y.; Tay, B. Y.; Zhao, C.; Kong, J.; Stubbs, L. P.; Lu, X. One-Pot Synthesis of Fe(III)–Polydopamine Complex Nanospheres: Morphological Evolution, Mechanism, and Application of the Carbonized Hybrid Nanospheres in Catalysis and Zn–Air Battery. *Langmuir* **2016,** *32* (36), 9265-9275.

(15) Ju, K.-Y.; Lee, J. W.; Im, G. H.; Lee, S.; Pyo, J.; Park, S. B.; Lee, J. H.; Lee, J.-K. Bio-Inspired, Melanin-Like Nanoparticles as a Highly Efficient Contrast Agent for T1-Weighted Magnetic Resonance Imaging. *Biomacromolecules* **2013,** *14* (10), 3491-3497.

(16) Miao, Z.-H.; Wang, H.; Yang, H.; Li, Z.-L.; Zhen, L.; Xu, C.-Y. Intrinsically Mn2+-Chelated Polydopamine Nanoparticles for Simultaneous Magnetic Resonance Imaging and Photothermal Ablation of Cancer Cells. *ACS Appl. Mater. Interfaces* **2015,** *7* (31), 16946-16952.

(17) Aime, S.; Bergamasco, B.; Biglino, D.; Digilio, G.; Fasano, M.; Giamello, E.; Lopiano, L. EPR investigations of the iron domain in neuromelanin. *Biochim. Biophys. Acta, Mol. Basis Dis.* **1997,** *1361* (1), 49-58.

(18) Li, Y.; Xie, Y.; Wang, Z.; Zang, N.; Carniato, F.; Huang, Y.; Andolina, C. M.; Parent, L. R.; Ditri, T. B.; Walter, E. D.; Botta, M.; Rinehart, J. D.; Gianneschi, N. C. Structure and Function of Iron-Loaded Synthetic Melanin. *ACS Nano* **2016,** *10* (11), 10186-10194.

(19) Borg, D. C. TRANSIENT FREE RADICAL FORMS OF HORMONES: EPR SPECTRA FROM CATECHOLAMINES AND ADRENOCHROME. *Proc. Natl. Acad. Sci. U.S.A.* **1965,** *53* (3), 633.

(20) Sever, M. J.; Weisser, J. T.; Monahan, J.; Srinivasan, S.; Wilker, J. J. Metal-Mediated Cross-Linking in the Generation of a Marine-Mussel Adhesive. *Angew. Chem., Int. Ed.* **2004,** *43* (4), 448-450.

(21) Weisser, J. T.; Nilges, M. J.; Sever, M. J.; Wilker, J. J. EPR Investigation and Spectral Simulations of Iron−Catecholate Complexes and Iron−Peptide Models of Marine Adhesive Cross-Links. *Inorg. Chem.* **2006,** *45* (19), 7736-7747.

(22) Burlamacchi, L.; Lai, A.; Monduzzi, M.; Saba, G. NMR, EPR, and INDO Studies on the complexes of dopamine with Cu2+, Mn2+, and Fe3+ in aqueous solution. *Journal of Magnetic Resonance (1969)* **1983,** *55* (1), 39-50.

(23) Lucarini, M.; Pedulli, G. F.; Guerra, M. A Critical Evaluation of the Factors Determining the Effect of Intramolecular Hydrogen Bonding on the O   H Bond Dissociation Enthalpy of Catechol and of Flavonoid Antioxidants. *Chem. Eur. J.* **2004,** *10* (4), 933-939.

(24) Bolzoni, F.; Giraudo, S.; Lopiano, L.; Bergamasco, B.; Fasano, M.; Crippa, P. R. Magnetic investigations of human mesencephalic neuromelanin. *Biochim. Biophys. Acta, Mol. Basis Dis.* **2002,** *1586* (2), 210-218.

(25) Gerlach, M.; Trautwein, A. X.; Zecca, L.; Youdim, M. B. H.; Riederer, P. Mössbauer Spectroscopic Studies of Purified Human Neuromelanin Isolated from the Substantia Nigra. *J. Neurochem.* **1995,** *65* (2), 923-926.

(26) Charkoudian, L. K.; Franz, K. J. Fe(III)-Coordination Properties of Neuromelanin Components: 5,6-Dihydroxyindole and 5,6-Dihydroxyindole-2-carboxylic Acid. *Inorg. Chem.* **2006,** *45* (9), 3657-3664.

(27) Della Vecchia, N. F.; Luchini, A.; Napolitano, A.; D'Errico, G.; Vitiello, G.; Szekely, N.; d'Ischia, M.; Paduano, L. Tris Buffer Modulates Polydopamine Growth, Aggregation, and Paramagnetic Properties. *Langmuir* **2014,** *30* (32), 9811-9818.

(28) Koenig, S. H.; Brown, R. D.; Spiller, M.; Chakrabarti, B.; Pande, A. Intermolecular protein interactions in solutions of calf lens alpha-crystallin. Results from 1/T1 nuclear magnetic relaxation dispersion profiles. *Biophys. J.* **1992,** *61* (3), 776-785.
(29) Aime, S.; Botta, M.; Terreno, E. Gd (III)-based contrast agents for MRI. *Adv. Inorg. Chem* **2005,** *57*, 173-237.

(30) Bertini, I.; Luchinat, C.; Parigi, G. Chapter 5 Transition Metal Ions: Shift and Relaxation. *Curr. Methods Inorg. Chem* **2001,** *2*, 143-203.

(31) Bertini, I.; Capozzi, F.; Luchinat, C.; Xia, Z. Nuclear and electron relaxation of hexaaquairon (3+). *J. Phys. Chem.* **1993,** *97* (6), 1134-1137.

(32) Bertini, I.; Galas, O.; Luchinat, C.; Messori, L.; Parigi, G. A theoretical analysis of the 1H nuclear magnetic relaxation dispersion profiles of diferric transferrin. *J. Phys. Chem.* **1995,** *99* (39), 14217-14222.

(33) Bertini, I.; Luchinat, C.; Nerinovski, K.; Parigi, G.; Cross, M.; Xiao, Z.; Wedd, A. G. Application of NMRD to Hydration of Rubredoxin and a Variant Containing a (Cys-S)3FeIII(OH) Site. *Biophys. J.* **2003,** *84* (1), 545-551.

(34) Koenig, S. H.; Brown 3rd, R.; Lindstrom, T. Interactions of solvent with the heme region of methemoglobin and fluoro-methemoglobin. *Biophys. J.* **1981,** *34* (3), 397-408.

(35) Li, Y.; Huang, Y.; Wang, Z.; Carniato, F.; Xie, Y.; Patterson, J. P.; Thompson, M. P.; Andolina, C. M.; Ditri, T. B.; Millstone, J. E.; Figueroa, J. S.; Rinehart, J. D.; Scadeng, M.; Botta, M.; Gianneschi, N. C. Polycatechol Nanoparticle MRI Contrast Agents. *Small* **2016,** *12* (5), 668-677.

(36) Sitbon, G.; Bouccara, S.; Tasso, M.; Francois, A.; Bezdetnaya, L.; Marchal, F.; Beaumont, M.; Pons, T. Multimodal Mn-doped I–III–VI quantum dots for near infrared fluorescence and magnetic resonance imaging: from synthesis to in vivo application. *Nanoscale* **2014,** *6* (15), 9264-9272.

(37) Fan, Q.; Cheng, K.; Hu, X.; Ma, X.; Zhang, R.; Yang, M.; Lu, X.; Xing, L.; Huang, W.; Gambhir, S. S.; Cheng, Z. Transferring Biomarker into Molecular Probe: Melanin Nanoparticle as a Naturally Active Platform for Multimodality Imaging. *J. Am. Chem. Soc.* **2014,** *136* (43), 15185-15194.

(38) Vitiello, G.; Pezzella, A.; Zanfardino, A.; Varcamonti, M.; Silvestri, B.; Costantini, A.; Branda, F.; Luciani, G. Titania as a driving agent for DHICA polymerization: a novel strategy for the design of bioinspired antimicrobial nanomaterials. *J. Mater. Chem. B* **2015,** *3* (14), 2808-2815.

(39) Sarna, T.; Hyde, J. S.; Swartz, H. M. Ion-exchange in melanin: an electron spin resonance study with lanthanide probes. *Science* **1976,** *192* (4244), 1132-1134.

(40) Rabenstein, M. D.; Shin, Y.-K. Determination of the distance between two spin labels attached to a macromolecule. *Proc. Natl. Acad. Sci. U.S.A.* **1995,** *92* (18), 8239-8243.

(41) Sebby, K. B.; Walter, E. D.; Usselman, R. J.; Cloninger, M. J.; Singel, D. J. End-Group Distributions of Multiple Generations of Spin-Labeled PAMAM Dendrimers. *J. Phys. Chem. B* **2011,** *115* (16), 4613-4620.

(42) Usselman, R. J.; Russek, S. E.; Klem, M. T.; Allen, M. A.; Douglas, T.; Young, M.; Idzerda, Y. U.; Singel, D. J. Temperature dependence of electron magnetic resonance spectra of iron oxide nanoparticles mineralized in Listeria innocua protein cages. *J. Appl. Phys.* **2012,** *112* (8), 084701.
(43) Grillo, V. A.; Hanson, G. R.; Wang, D.; Hambley, T. W.; Gahan, L. R.; Murray, K. S.; Moubaraki, B.; Hawkins, C. J. Synthesis, X-ray Structural Determination, and Magnetic Susceptibility, Mössbauer, and EPR Studies of (Ph4P)2[Fe2(Cat)4(H2O)2]·6H2O, a Catecholato-Bridged Dimer of Iron(III). *Inorg. Chem.* **1996,** *35* (12), 3568-3576.

(44) Anderson, B. F.; Web, J.; Buckingham, D. A.; Robertson, G. B. Crystal and molecular structure of piperidinium μ-acetato-di-μ-1,2-benzenediolato-bis-1,2-benzenediolatoferrate(III), (C5H12N)3 [(CH3COO){Fe(C6H4O2)2}2]: a compound of relevance to the 2Fe-active site of the respiratory protein hemerythrin. *J. Inorg. Biochem.* **1982,** *16* (1), 21-32.

(45) Ainscough, E. W.; Brodie, A. M.; McLachlan, S. J.; Brown, K. L. The reaction of 1,1′-biphenyl-2,2′-dial with iron(III) and the crystal structure of piperidinium bis[μ-(1,1′-biphenyl-2,2′-diolato-O,μ-O′)(1,1′-biphenyl-2,2′-diolato-O,O′)ferrate(III)]–ethanol(½). *J. Chem. Soc., Dalton Trans.* **1983,** (7), 1385-1389.

(46) Fisher, O. Z.; Larson, B. L.; Hill, P. S.; Graupner, D.; Nguyen-Kim, M.-T.; Kehr, N. S.; De Cola, L.; Langer, R.; Anderson, D. G. Melanin-like Hydrogels Derived from Gallic Macromers. *Adv. Mater.* **2012,** *24* (22), 3032-3036.

(47) Felix, C. C.; Hyde, J. S.; Sarna, T.; Sealy, R. C. Interactions of melanin with metal ions. Electron spin resonance evidence for chelate complexes of metal ions with free radicals. *J. Am. Chem. Soc.* **1978,** *100* (12), 3922-3926.

(48) Gorun, S. M.; Lippard, S. J. Magnetostructural correlations in magnetically coupled (.mu.-oxo)diiron(III) complexes. *Inorg. Chem.* **1991,** *30* (7), 1625-1630.

(49) Taylor, S. W.; Chase, D. B.; Emptage, M. H.; Nelson, M. J.; Waite, J. H. Ferric Ion Complexes of a DOPA-Containing Adhesive Protein from Mytilus edulis. *Inorg. Chem.* **1996,** *35* (26), 7572-7577.

(50) Azuah, R. T.; Kneller, L. R.; Qiu, Y.; Tregenna-Piggott, P. L.; Brown, C. M.; Copley, J. R.; Dimeo, R. M. DAVE: a comprehensive software suite for the reduction, visualization, and analysis of low energy neutron spectroscopic data. *J. Res. Natl. Inst. Stand. Technol.* **2009,** *114* (6), 341.

(51) Holten-Andersen, N.; Harrington, M. J.; Birkedal, H.; Lee, B. P.; Messersmith, P. B.; Lee, K. Y. C.; Waite, J. H. pH-induced metal-ligand cross-links inspired by mussel yield self-healing polymer networks with near-covalent elastic moduli. *Proceedings of the National Academy of Sciences* **2011,** *108* (7), 2651.

(52) Sever, M. J.; Wilker, J. J. Visible absorption spectra of metal–catecholate and metal–tironate complexes. *Dalton Trans.* **2004,** (7), 1061-1072.

(53) Prodi, L.; Rampazzo, E.; Rastrelli, F.; Speghini, A.; Zaccheroni, N. Imaging agents based on lanthanide doped nanoparticles. *Chem. Soc. Rev.* **2015,** *44* (14), 4922-4952.

Chapter 3 Perfluorocarbon-loaded polydopamine nanoparticles as ultrasound contrast agents

3.1 Abstract

In this chapter, PDA materials was used as another type of contrast agents. A versatile platform for the development of new ultrasound contrast agents is demonstrated through a one-pot synthesis and fluorination of submicron polydopamine (PDA-F) nanoparticles. The fluorophilicity of these particles allows loading with perfluoropentane (PFP) droplets that display strong and persistent ultrasound contrast in aqueous suspension and *ex vivo* tissue samples. Contrast under continuous imaging by color Doppler persists for 1 h in 135 nm PDA-F samples, even at maximum clinical imaging power (MI = 1.9). Additionally, use of a Cadence Contrast Pulse Sequence (CPS) results in a non-linear response suitable for imaging at 0.5 mg/mL. Despite the PFP volatility and the lack of a hollow core, PDA-F particles display minimal signal loss after storage for over a week. The ability to tune size, metal-chelation, and add covalently-bound organic functionality offers myriad possibilities for extending this work to multimodal imaging, targeted delivery, and therapeutic functionality.

3.2 Introduction

Medical ultrasound imaging is an essential modern diagnostic technique due to its affordability, lack of ionizing radiation, portability, tissue penetration, and real-time display. It serves as a valuable complement to more costly imaging modalities such as magnetic resonance imaging (MRI), positron emission tomography (PET), and computed tomography (CT).[1-3] As in many other medical imaging methods, ultrasound can be enhanced through the introduction of a contrast agent. These agents generate

48

contrast against surrounding tissue via a non-linear resonance interaction with the impinging ultrasound waves and thus do not require magnetic or radioactive properties to achieve strong signal to noise ratios. In fact, the current clinically-employed ultrasound agents are all inert low-boiling perfluorocarbons (PFC) stabilized within simple phospholipid or protein coatings.[2, 4] Under ultrasonic stimulation, these PFC droplets undergo large pressure changes resulting in a transition to a gaseous microbubble which can provide contrast under various ultrasound modalities.[5] Additionally, these microbubbles can potentially re-condense and provide long-term imaging through subsequent cavitational oscillations.[6] The large size of current ultrasound contrast agents (1-5 μm) is advantageous because it allows for high PFC-loading; however, it also restricts particle circulation time, displays poor accumulation and retention in target tissues, and only generates strong contrast at low frequencies, thus limiting resolution.[6] To improve upon these properties, a range of inorganic ultrasound contrast agents have been developed with better size control including hollow/porous silica,[1, 7-15] carbon nanotubes,[16] calcium carbonate nanoparticles,[17] and others.[18-19] The rigid shell structure of these materials allows for robust particles of sub-micron diameter and can encapsulate PFC in a more stable fashion. While structurally versatile, many inorganic contrast agents have limited size tunability due to the need for thin shells, and, in some cases, biocompatibility is limited or unknown. Ideally, an ultrasound contrast agent combines the biocompatibility of commercial organic structures with the structural versatility of the inorganic materials. One such approach is with polymer nanoparticles such as polydopamine (PDA), which is structurally very similar to naturally occurring melanin.[20] Many studies have demonstrated the biocompatibility of PDA, and coatings of PDA are frequently used to enhance the biocompatibility of other materials.[21-23] The chemical functionality present in PDA allows for a range of modifications via covalent bond formation and metal chelation leading to applications in MRI contrast,[21, 24-27] drug delivery,[28] cell imaging,[29] and photothermal therapeutics.[30-31] It is also tolerant of acidic and basic environments, forms stable aqueous suspensions, and can be synthesized at sub-micron sizes. While it lacks native ultrasound contrast and it is neither porous or fluorophilic enough to encapsulate or adsorb PFC, functionalization with fluorinated molecules has been demonstrated to facilitate the uptake of PFC in other polymer nanoparticles.[32-34] Herein, we demonstrate that < 0.5 μm

fluorine-functionalized PDA nanoparticles (PDA–F NPs) are capable of stabilizing perfluoropentane (PFP, b.p. = 29.2 C) droplets under aqueous conditions for use in color Doppler and cadence contrast pulse sequencing (CPS) ultrasound imaging.

3.3 Results and Discussions

3.3.1 Synthesis and Characterization of PDA-F NPs

Without significant porosity or fluorophilicity, PDA is predicted to show minimal uptake of PFCs and therefore minimal ultrasound contrast. Control samples of fluorine-free PDA were synthesized by previously described methods. Briefly, dopamine was dissolved in the mixture of ethanol and water under alkaline conditions and allowed to react for 24 h with stirring.[35] The dopamine polymerization process is briefly described in Figure 3.1. Typical transmission electron microscopy (TEM) and scanning electron microscopy (SEM) images are shown in Figure 3.2 and Fig. 3.3. By varying the dopamine hydrochloride (DA) concentration of the starting solution, particles of 74±10, 174±28, and 350±40 nm (PDA-74, PDA-174, and PDA-350, respectively) were obtained as determined by transmission electron microscopy (TEM) (Figure 3.2(a-c)). Fluorine-functionalized PDA (PDA-F) NPs were similarly prepared with the only variation being an *in situ* Michael addition reaction commonly shown to functionalize catechols with thiol and amino groups under mild alkaline conditions.[31, 36-37] Specifically, perfluorodecanethiol was added after 9 h of reaction time such that the growing PDA incorporated the perfluorinated side-chain as has been demonstrated previously for the synthesis of superhydrophobic surfaces.[38-39] PDA-F NPs of 41±14, 135±28, and 242±33 nm PDA-F (PDA-41-F, PDA-135-F, and PDA-242-F, respectively) were synthesized to allow comparison to unfluorinated PDA of roughly equivalent size (Figure 3.2 (d-f); Figure 3.3 (d-f)). The presence of C–F bonds at the particle surface was confirmed by X-ray photoelectron spectroscopy (XPS) on all three PDA-F samples.[40] (Figure 3.4). Energy dispersive X-ray spectra (EDS) was used to quantify S and F content of PDA-F NPs (Figure 3.5). PDA-135-F

and PDA-242-F show ~8 wt% F with a S ratio roughly corresponding to that expected for the

perfluorodecanethiol unit. However, PDA-41-F has far higher F and S content, consistent with the

low-density interparticle linking structures visible by TEM. Interestingly, direct addition of

perfluorodecanethiol prior to PDA nucleation did not result in any particle formation, likely due to

excessive termination of the polymer growth sites by the thiol.
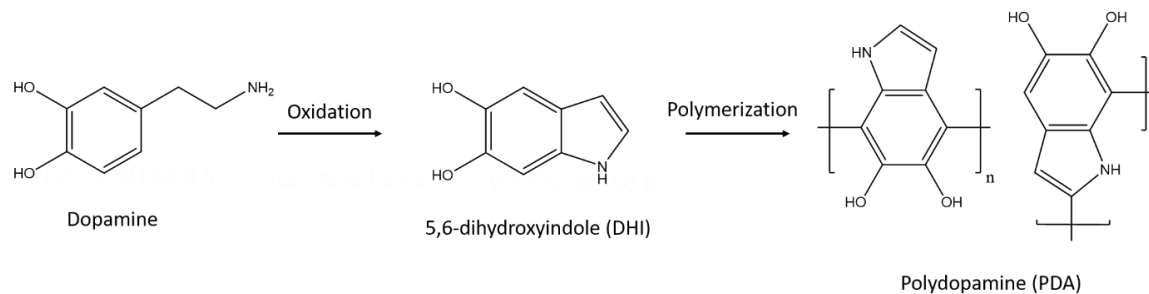
Figure 3.1 The schematic figure for dopamine polymerization. Copyright 2018 Royal Society of Chemistry.[41]
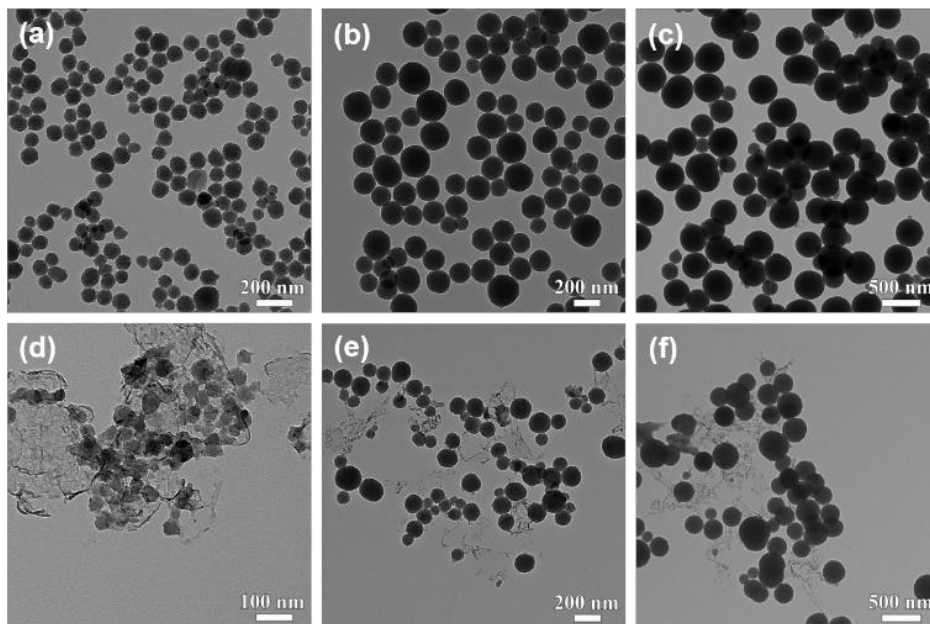
Figure 3.2 TEM images of (a) PDA-74, (b) PDA-174, (c) PDA-350, (d) PDA-41-F, (e) PDA-135-F, and (f) PDA-242-F. Copyright 2018 Royal Society of Chemistry.[41]
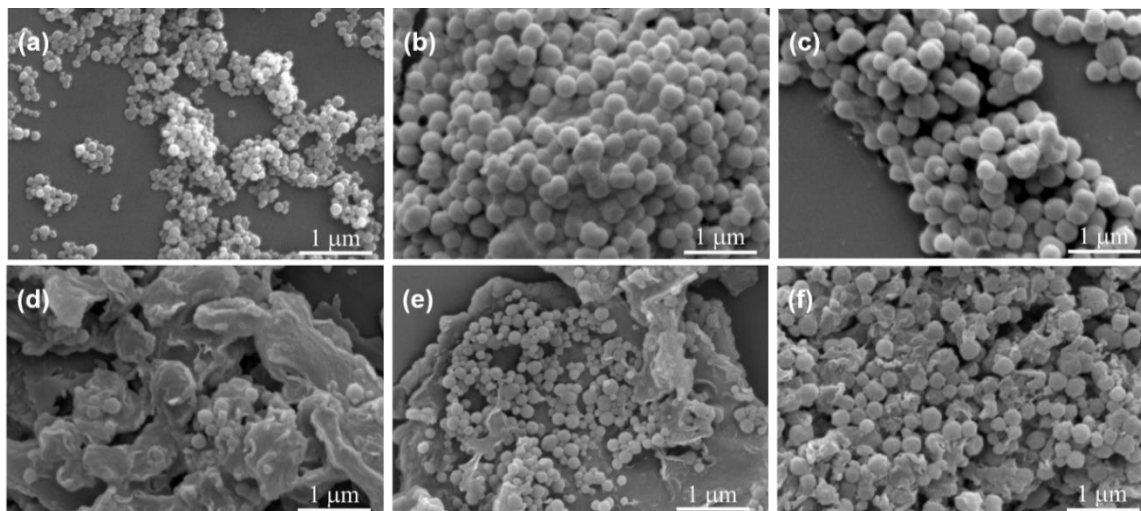
Figure 3.3 SEM images of (a) PDA-74, (b) PDA-174, (c) PDA-350, (d) PDA-41-F, (e) PDA-135-F, and (f) PDA-242-F. Copyright 2018 Royal Society of Chemistry.[41]
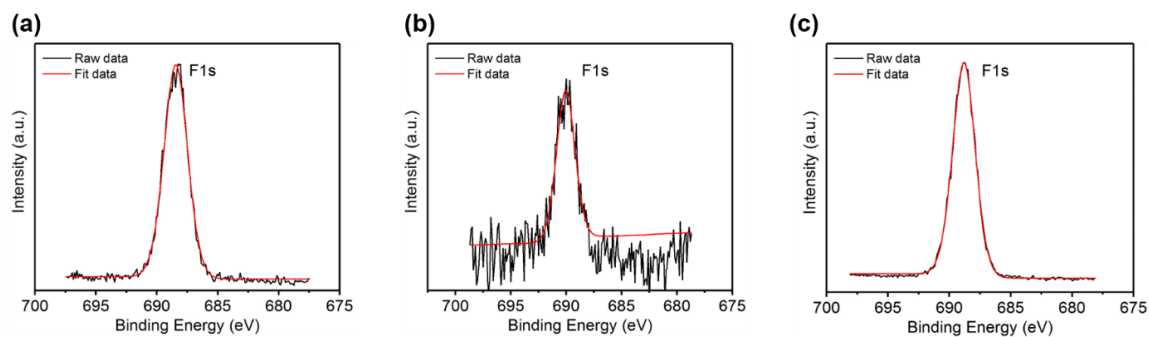
Figure 3.4 F1s XPS spectra of (a) PDA-41-F, (b) PDA-135-F, and (c) PDA-242-F. Copyright 2018 Royal Society of Chemistry.[41]
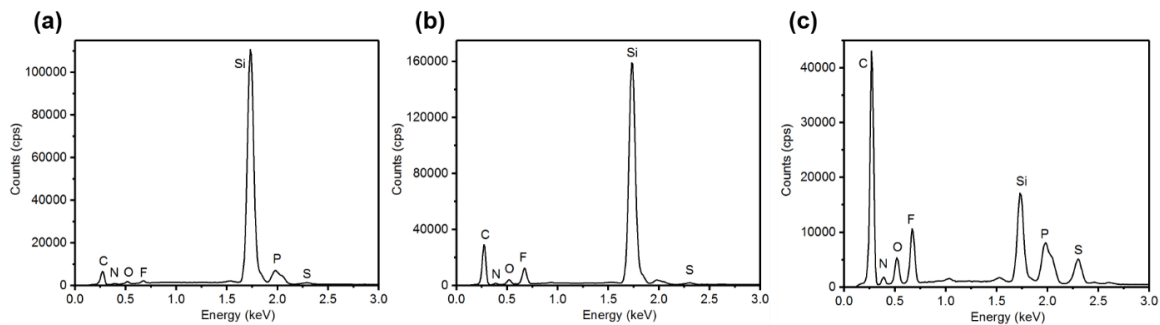
Figure 3.5 EDS spectrum of (a) PDA-41-F, (b) PDA-135-F, and (c) PDA-242-F. Copyright 2018 Royal Society of Chemistry.[41]

52

Alterations in the particle morphology between PDA and PDA-F can be observed by TEM, with interparticle polymeric linkages clearly forming in the case of PDA-41-F. To examine the extent of these linkages, Dynamic Light Scattering (DLS) was employed to determine the average hydrodynamic radius (R_{hyd}) of PDA-41-F (R_{hyd} = 220 nm), PDA-135-F (R_{hyd} = 250 nm), and PDA-242-F (R_{hyd} = 400 nm) suspensions. These results corroborate the TEM data wherein PDA-41-F displays significant covalent interparticle linkage while both PDA-135-F and PDA-242-F show little to no linkage or aggregation (Figure 3.6). Zeta potentials of PDA-41-F, PDA-135-F, and PDA-242-F were -9.6±1.3, -13.7±0.7 and -23.8±1.4 mV, respectively, showing moderate stability in aqueous solution. Even the largest of our particles are significantly smaller than current clinical ultrasound contrast agent sizes (R_{hyd} = 1−7 μm)[42] thus increasing their potential for cell permeability and use in extravascular space.
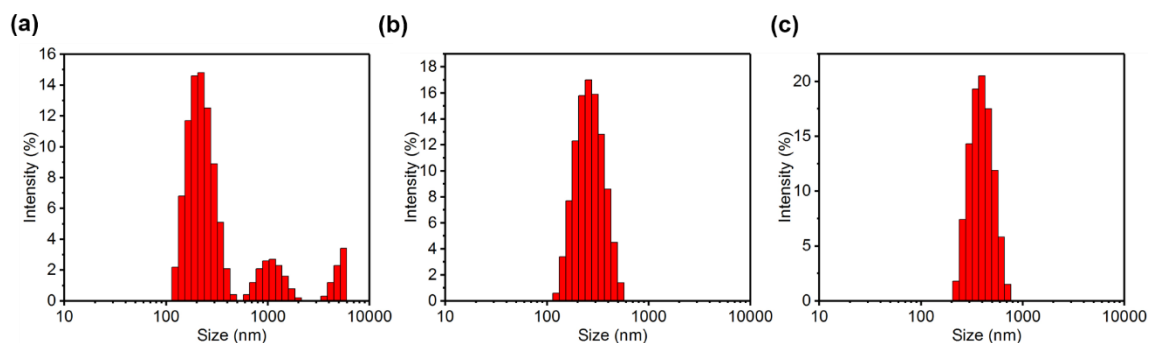
Figure 3.6 DLS size distributions of (a) PDA-41-F, (b) PDA-135-F, and (c) PDA-242-F. Copyright 2018 Royal Society of Chemistry. [41]

To function as an ultrasound contrast agent, PDA-F requires enough fluorophilicity to nucleate a liquid droplet of low boiling point PFC. Similar to other ultrasound agents, PDA-F can then generate contrast from a phase shift of the probe ultrasound pulse. Uniquely, our PFC droplet is external to the stabilizing unit (PDA-F) instead of being encapsulated by it as in all other ultrasound agents reported to date. Loading of PDA-F with perfluoropentane (PFP, T_b = 29.2 °C) was achieved by suspending the NPs in

200 µL of PFP liquid, sonicating for 30 s, and allowing the residual to evaporate. Dynamic Light Scattering (DLS) data of PFP-loaded PDA-F demonstrates an increase in hydrodynamic radius size compared with pure PDA-F samples, consistent with PFP-loading on the surface (Figure 3.7).
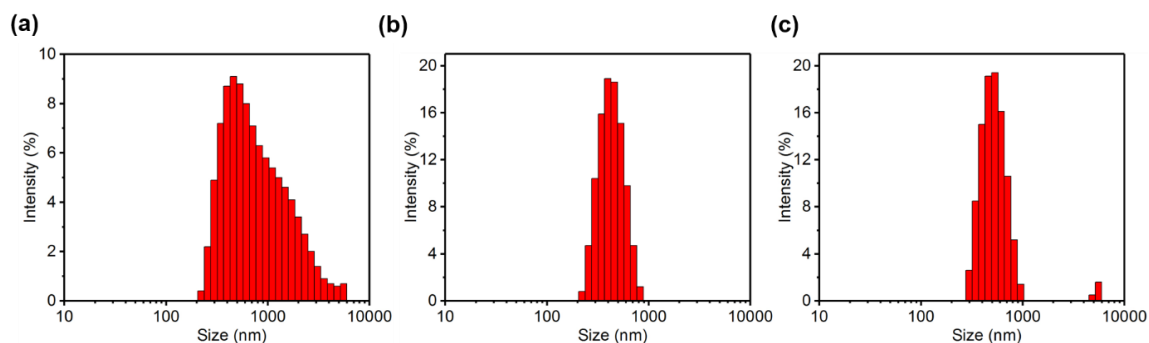
Figure 3.7 DLS size distributions of PFP-loaded (a) PDA-41-F, (b) PDA-135-F, and (c) PDA-242-F. Copyright 2018 Royal Society of Chemistry.[41]

3.3.2   In vitro Ultrasound Imaging Test of PFP-loaded PDA-F NPs

Subsequent to exposure to PFP, both PDA and PDA-F samples were examined using two ultrasound imaging modes: Color Doppler and Contrast Pulse Sequencing (CPS). Unlike standard B mode imaging, CPS does not show contrast in the absence of an effective contrast agent and color Doppler will only show contrast in a flowing medium. Color Doppler signal is a result of cavitation and release of PFP gas which can then be imaged as blue- or redshifted signal from the moving gas.[8] Color Doppler imaging was performed on stable aqueous suspensions of 0.5 mg/mL PDA and PDA-F at an optimized frequency ($f = 7$ MHz) with a clinically-safe Mechanical Index (MI ≤ 1.9). Color Doppler of PDA-F reveals a far stronger response than the unfluorinated PDA NPs (Figure 3.8). The drastic increase in signal upon fluorination of the polymer NPs indicates a much higher uptake of PFP in PDA-F samples. Control experiments on aqueous dispersions of 0.5 mg/mL PDA-74, PDA-174 and PDA-350 without PFP treatment reveal that pure PDA particles do not show color Doppler signal above background (Figure 3.9).
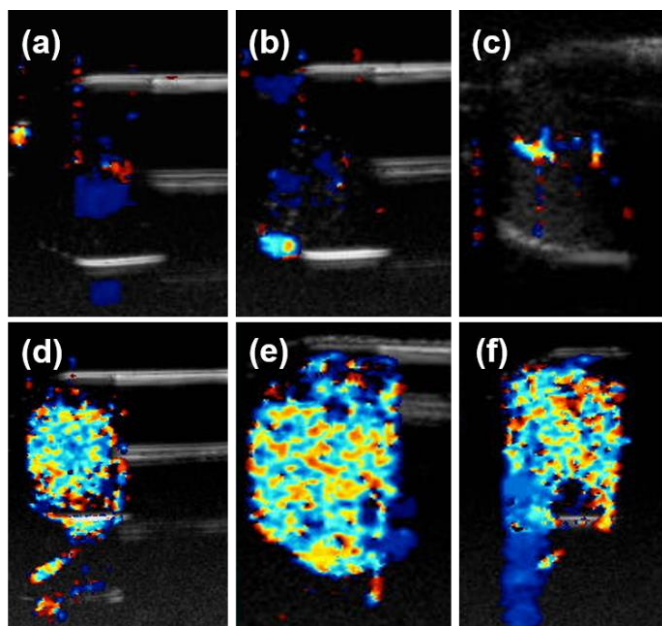
Figure 3.8 Color Doppler imaging of (a) PDA-74, (b) PDA-174, (c) PDA-350, (d) PDA-41-F, (e) PDA-135-F, and (f) PDA-242-F at MI=1.9. Copyright 2018 Royal Society of Chemistry.[41]
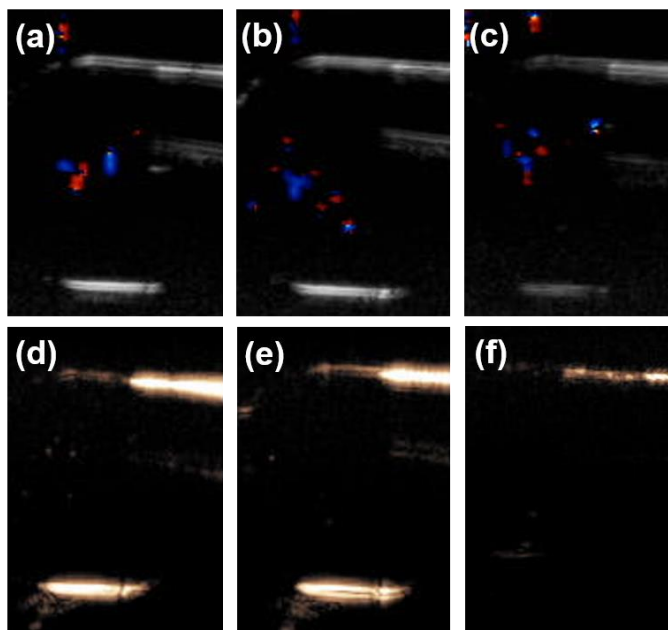
Figure 3.9 Color Doppler imaging of (a) PDA-74, (b) PDA-174, and (c) PDA-350; CPS imaging of (d) PDA-74, (e) PDA-174, and (f) PDA-350 at MI=1.9 in aqueous solution without PFP treatment. Copyright 2018 Royal Society of Chemistry.[41]

One factor of particular importance in color Doppler imaging is the temporal persistence of signal. We found that all three PDA-F sizes show significant color Doppler signal persistence

(Figure 3.8d-f), with PDA-135-F providing approximately 1 h of imaging time (Figure 3.10d and Figure 3.11). Although the color Doppler signal is difficult to quantify, continuous imaging for 1 h is not achievable with current commercial ultrasound contrast agents.[7, 43] By comparison, commercially-available Definity (Perflutren Lipid Microspheres) retain a color Doppler signal for approximately 5 min (Figure 3.11c).
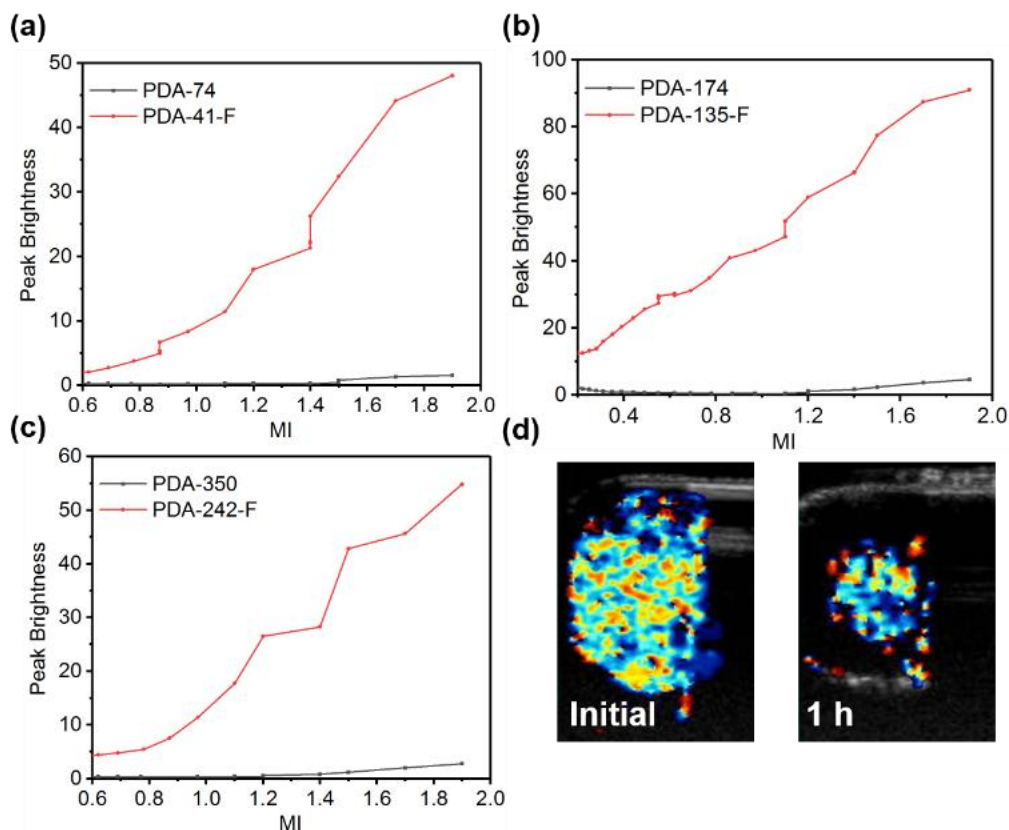
Figure 3.10 Quantitative plot of brightness on CPS imaging versus MI for (a) PDA-74 & PDA-41-F, (b) PDA-174 & PDA-135-F, (c) PDA-350 & PDA-242-F, (d) Color Doppler signal detected at (a) beginning and 1 h for PDA-135-F. Copyright 2018 Royal Society of Chemistry.[41]
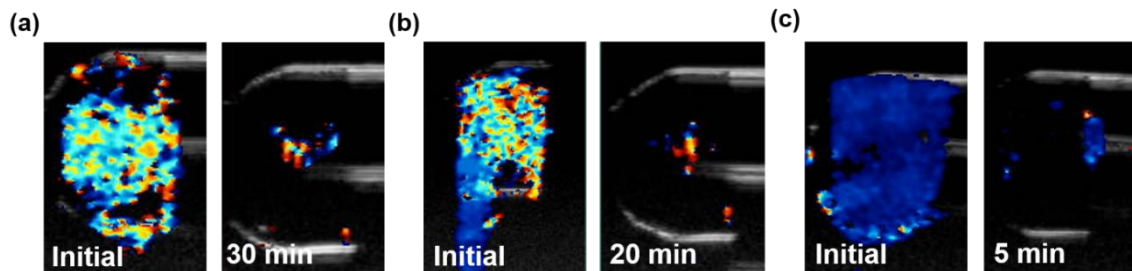
Figure 3.11 Color Doppler signal detected at (a) beginning and 30 min for PDA-41-F, (b) beginning and 20 min for PDA-242-F, (c) beginning and 5 min for commercial Definity contrast agents at MI=1.9. Copyright 2018 Royal Society of Chemistry.[41]

Given the long imaging times, testing of stability of PFC loading allows for delayed imaging and periodic imaging without reintroduction of contrast agent. To demonstrate the long-term stability of PFP-loaded PDA-F particles, PDA-135-F was charged with PFP and stored at 4 °C for one week. Color Doppler imaging reveals a strong signal roughly equivalent to that of freshly prepared samples (Figure 3.12).
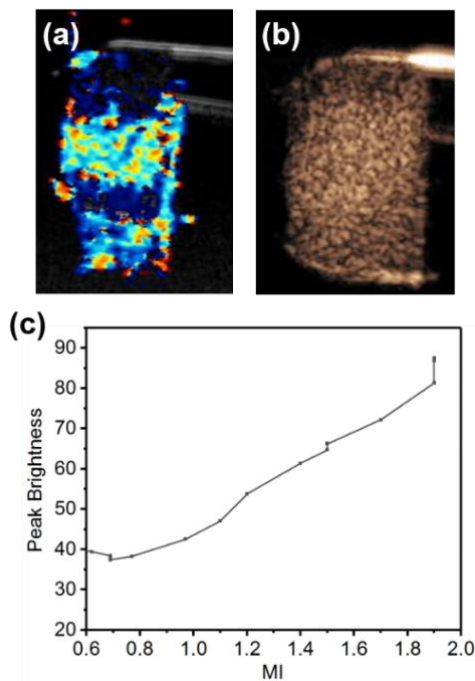
Figure 3.12 One-week shelf life test of PDA-135-F for (a) Color Doppler imaging, (b) CPS imaging, and (c) quantitative plot on brightness of CPS imaging versus MI. Copyright 2018 Royal Society of Chemistry.[41]

To provide a more quantitative analysis of the ultrasound contrast ability of pure PDA and PDA-F NPs, CPS imaging was performed as a function of MI (Figure 3.13). CPS signal is achieved via a non-linear response designed to improve specificity to the contrast agent. CPS brightness quantification was adapted from Liberman *et al.*[44] Briefly, the gold specks in the CPS correspond to echo decorrelation events and signal generation from PFP gas. An average brightness was determined from the signal intensity of a fixed region of interest. In parallel to the color Doppler results, PDA-F demonstrates strong contrast compared to unfluorinated PDA samples (Fig. 3.13). In fact, there is no significant contrast difference between PDA samples and deionized water (Figure 3.14), confirming PFP as the source of the CPS contrast. Unlike commercial ultrasound agents, the CPS signal was found to increase continuously with increasing MI, up to 1.9. These results indicate the robust nature of PFP adhesion to PDA-F NPs, despite its volatility. Particles of the intermediately-sized PDA-135-F shows the highest contrast intensity among three PDA-F samples, with approximately twice the brightness of PDA-41-F and PDA-242-F (Figure 3.10a-c). The CPS signal of our PDA-F is also comparable to the commercial agent Definity (Figure 3.15) as well as promising new contrast agents such as perfluorocarbon-loaded hollow silica.[8] We also note that quantitative CPS analysis (Figure 3.12c) shows that after one-week, PDA-135-F particles still retain 96% of the brightness of freshly prepared samples (Figure 3.12b).
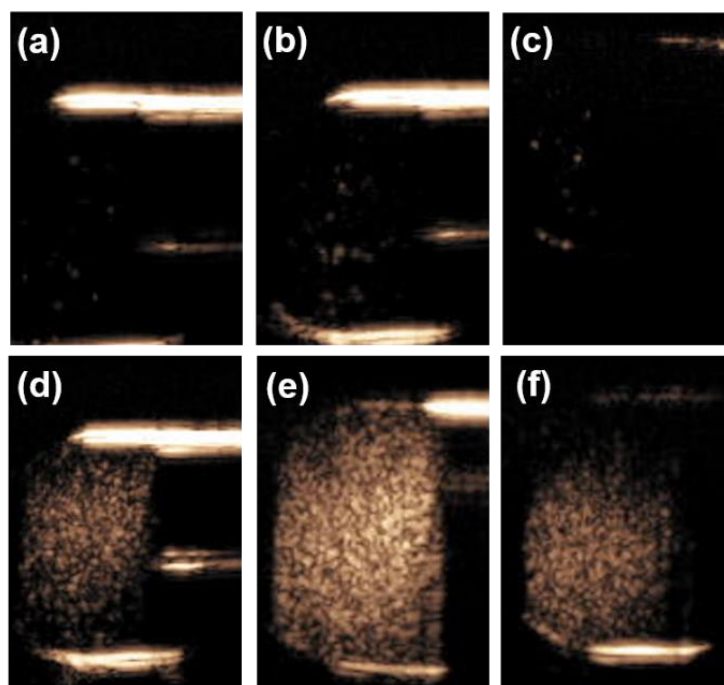
Figure 3.13 CPS imaging of (a) PDA-74, (b) PDA-174, (c) PDA-350, (d) PDA-41-F, (e) PDA-135-F, and (f) PDA-242-F at MI=1.9. Copyright 2018 Royal Society of Chemistry.[41]
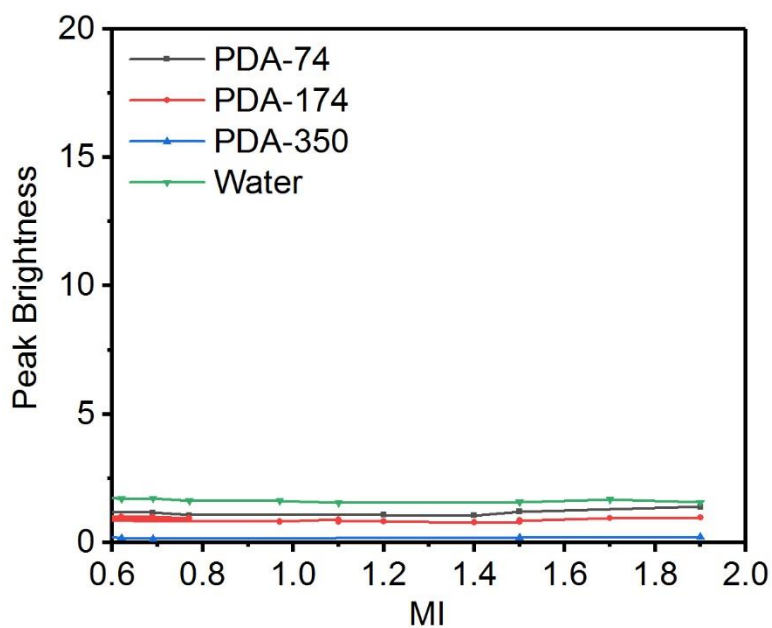

Figure 3.14 Quantitative plot of brightness on CPS imaging versus MI for (a) PDA-74, (b) PDA-174, and (c) PDA-350 in aqueous solution without PFP treatment. Copyright 2018 Royal Society of Chemistry.[41]
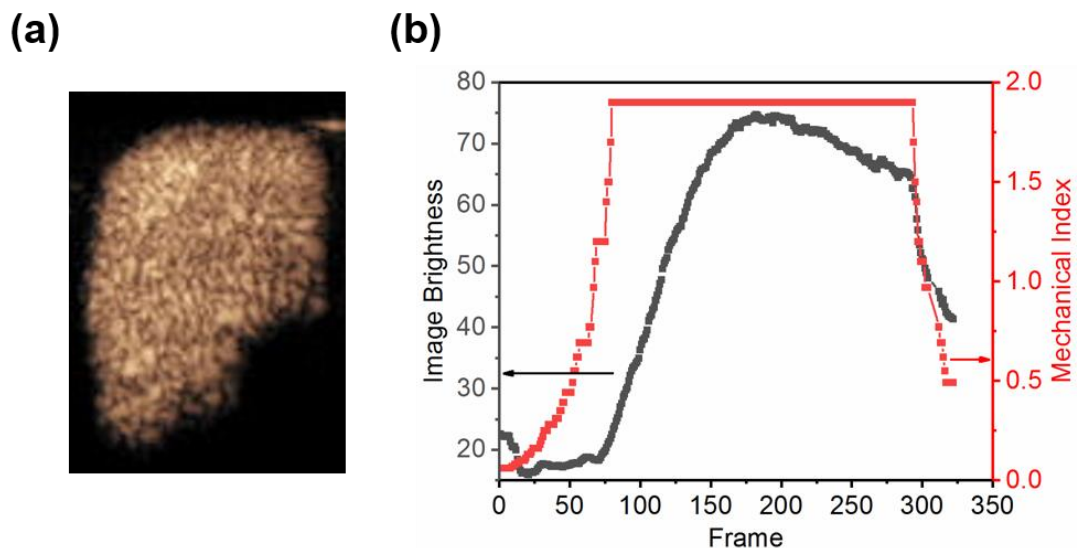
Figure 3.15 (a) CPS imaging, and (b) quantitative average pixel brightness and MI for CPS imaging of the commercial contrast agent Definity. Copyright 2018 Royal Society of Chemistry.[41]

To investigate whether the morphology of PDA-F was impacted by ultrasound imaging, TEM images were collected of the samples after ultrasound imaging at MI = 1.9 immediately. Although aggregation is observed, the PDA-F NPs remain intact, with no evidence of broken or deformed particles (Fig. 3.16).
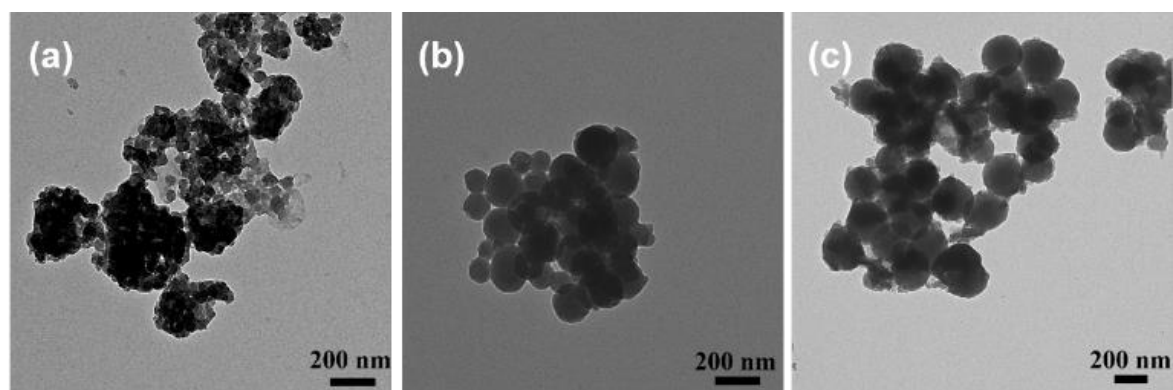
Figure 3.16 TEM of PDA-F samples after ultrasound imaging measurement for (a) PDA-41-F, (b) PDA-135-F, and (c) PDA-242-F at MI=1.9. Copyright 2018 Royal Society of Chemistry.[41]

3.3.3   In vitro Cell viability and Ex vivo Ultrasound Imaging Test of PFP-loaded PDA-F NPs

PDA has been demonstrated to be a robust material under a wide range of conditions, including those relevant to *in vivo* ultrasound. In fact, natural melanin is a ubiquitous polymeric biomaterial that shares many structural characteristics with PDA. As a preliminary demonstration of the biological stability. Preliminary *in vitro* cytotoxicity of PDA-41-F, PDA-135-F, and PDA-242-F (c = 10 to 500 µg/mL) was assessed by incubation with HCT116 cells for 24 h. Analysis via MTS (3-(4,5-dimethylthiazol-2-yl)-5-(3-carboxymethoxyphenyl)-2-(4-sulfophenyl)-2H-tetrazolium) assay indicates cell viability greater than 90% for all samples at all concentrations (Figure 3.17).
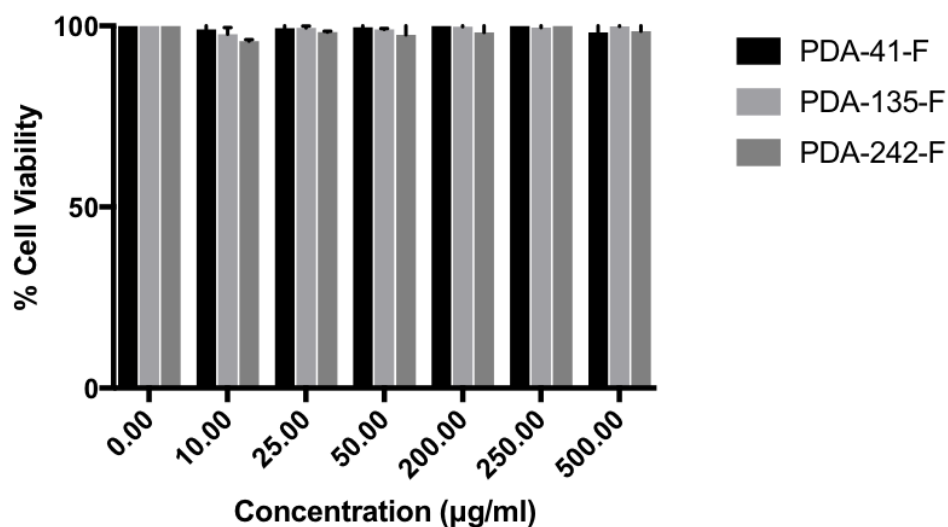
Figure 3.17 Cell viability of HCT116 cells after incubation with different concentrations of PDA-41-F, PDA-135-F, and PDA-242-F for 24 h. Copyright 2018 Royal Society of Chemistry.[41]

As an additional probe of the biological stability and bioimaging capability of PDA-F, an *ex vivo* imaging study was performed in fresh porcine liver tissue (Figure 3.18). Liver tissue was chosen because hepatic clearance plays a major role in nanoparticle biomedical applications.[45] Furthermore, liver is highly vascularized and can be used as an easily accessible preliminary demonstration for tissue compatibility of the PDA nanoparticles. PDA-F was injected 2 cm into three separate tissue locations and immediately imaged via color Doppler, giving signal persistence roughly equivalent to that observed *in vitro*. It has been

demonstrated that at an MI of 1.9, PDA-F was visible via color Doppler at up to 2 cm tissue depth. Although commercial microbubbles usually operate at a lower MI via bubble oscillation, the PDA-F nanoparticles generated ultrasound signal from surface condensed PFP that was phase changed under ultrasound insonation, which may require a higher ultrasound pressure (MI = 1.9). Nevertheless, the unique mosaic pattern of the color Doppler signal generated from the PDA-F remains an obvious contrast to B-mode ultrasound signal from the liver tissue. The signal footprint on the Doppler graph was on average 4 cm^3, (40 times the initial injection volume of 100 μL), demonstrating effective tissue perfusion in the liver. Additionally, *in vivo* blood flow patterns typically exhibit solid color Doppler signals due to their fixed directional flow. As a result, PDA-F perfused tissue, or potentially tumors, can be easily identified via ultrasound imaging.
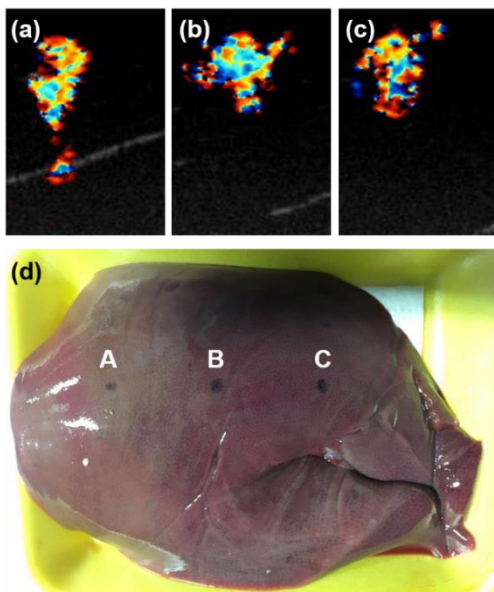
Figure 3.18 Color Doppler imaging of (a) PDA-41-F, (b) PDA-135-F, (c) PDA-242-F in fresh porcine liver at MI=1.9. (d) The photograph of the fresh pork liver; PDA-41-F, PDA-135-F, and PDA-242-F was injected into the position of A, B, C, respectively. Copyright 2018 Royal Society of Chemistry.[41]

3.4 Experimental Section

3.4.1 Materials

Dopamine hydrochloride (99%) and Tris(hydroxymethyl)aminomethane (Tris, 99%) were purchased from Alfa Aesar. 1H,1H,2H,2H-Perfluorodecanethiol (97%) was purchased from Sigma-Aldrich. Perfluoropentane (PFP) was purchased from Strem Chemicals. Ethanol (100%) was obtained from Fisher Scientific. All chemicals and solvents were used without further purification. Fresh pork liver for *ex vivo* tissue imaging was purchased from Ranch 99 Market and used as received.

3.4.2   Characterization

TEM images were collected on an FEI Tecnai G2 Spirit TEM operating at 120 kV. SEM images and elemental composition were collected on an FEI Quanta 250 SEM equipped with a Thermo Fisher Scientific Energy-dispersive X-ray spectroscopy (EDS) detector. Size of dispersed PDA and PDA-F nanoparticles in aqueous solution and zeta potentials were determined by Dynamic Light Scattering (DLS) measured with a Malvern Zetasizer Nano ZS90. XPS data were collected on a Thermo Scientific ESCALAB 250 Xi spectrometer using monochromated Al Kα radiation. The carbon 1s peak at 284.8 eV was used for calibration. Ultrasound data were collected on a Siemens Sequoia 512 with an Acuson 15L8 transducer.

3.4.3   Synthesis of PDA NPs

Unfluorinated PDA NPs were synthesized according to a previously reported method.[35] For the synthesis of PDA-174, dopamine hydrochloride (30 mg) was dissolved in a solution of ethanol (20 mL) and water (15 mL) with magnetic stirring. Tris solution (30 mg in 10 mL H_2O) was added and the solution was stirred continuously for 24 h at room temperature. The resulting colloidal black suspension was separated by centrifugation and washed with DI water three times. PDA-74 and PDA-350 NPs were prepared similarly with 20 mg and 40 mg of dopamine hydrochloride, respectively.

3.4.4 Synthesis of PDA-F NPs

For the synthesis of PDA-135-F NPs, dopamine hydrochloride (30 mg) was dissolved in an ethanol (20 mL) and H_2O (15 mL) mixture with magnetic stirring. Tris (30 mg in 10 mL H_2O) was added and the system stirred continuously for 9 h. To the resulting black colloidal suspension, 1H,1H,2H,2H-Perfluorodecanethiol (50 µL) was added and stirring was continued for another 15 h. The product was separated by centrifugation and washed with DI water three times. PDA-41-F and PDA-242-F NPs were prepared by identical methods with 20 mg and 40 mg of dopamine hydrochloride, respectively.

3.4.5 Preparation of PFP loaded PDA and PDA-F NPs

PFP loaded PDA NPs were prepared through a typical immersion method.[33] Particles were freeze dried at −55 °C and 0.04 mbar for 12 h. The subsequent PDA or PDA-F NPs (~1 mg) were dispersed in PFP (200 µL) and sonicated for 30 s. DI water (2 mL) was added to the mixture and another sonication cycle was performed (30 s).

3.4.6 Ultrasound experiments

Aqueous dispersions of PFP-loaded PDA or PDA-F NPs (0.5 mg/mL) were used for all ultrasound experiments. Imaging experiments were performed in both color Doppler and CPS modes. To determine the MI dependence, images were acquired continuously with the increase of MI from 0.06 to 1.9 over the course of 10 s. CPS imaging was performed at 7 MHz and the image brightness was quantified by averaging pixel brightness over the entire sample using MATLAB R2016b. Imaging lifetimes were determined by continuous color Doppler imaging at 1.9 MI until the signal fell to the level of the DI water signal intensity.

3.4.7 Ex vivo porcine liver ultrasound experiments

PFP-loaded PDA-F NPs (4 mg/mL) were injected into fresh pork liver tissue (21 cm×14 cm) with 100 µL volume. Color Doppler images were acquired continuously with the increase of MI from 0.06 to 1.9 immediately after injection. Signal acquisition across MI range allows for the determination of the minimum MI required to generate color Doppler signal in tissue.

3.5 Conclusion

Perfluorodecanethiol-functionalized PDA NPs (PDA-F NPs) have been demonstrated to load the perfluorocarbon PFP and function as stable, bright, long-lived contrast agents in two clinically-relevant ultrasound modalities: Color Doppler and CPS. A series of PDA-F NPs with size from 70 nm to 350 nm were synthesized with 170 nm PDA-F NPs demonstrating the best signal to noise ratio and longevity. Compared with commercial contrast agents, PDA-135-F NPs show favorable color Doppler imaging lifetime (~1 h) and comparable CPS signal, despite being volumetrically two orders of magnitude smaller. Even more intriguing may be their facile synthetic tunability. Not only does this offer the possibility to improve upon their contrast characteristics, but also (1) size can be tuned across a wide range allowing for variable extravasation, passive targeting of cells, and increased retention time, (2) surface functionality can be tuned to allow specific targeting of biomolecules in vivo, and (3) chelation of metals at the catechol units of PDA can be tuned to install multi-functionality such as MRI contrast.[21, 24-27]

3.6 Acknowledgement

Chapter 3 is a full reprint of materials published in the following paper: **Perfluorocarbon-loaded polydopamine nanoparticles as ultrasound contrast agent**, Yijun Xie, James Wang, Zhao Wang, Kelsey A. Krug, Jeffery D. Rinehart, *Nanoscale* **2018**, 10, 12813-12819, with permission from The Royal Society of Chemistry, 2018. The dissertation author is the first author of this paper.

3.7 References

(1) Yildirim, A.; Chattaraj, R.; Blum, N. T.; Goldscheitter, G. M.; Goodwin, A. P. Stable Encapsulation of Air in Mesoporous Silica Nanoparticles: Fluorocarbon-Free Nanoscale Ultrasound Contrast Agents. *Adv. Healthcare Mater.* **2016,** *5* (11), 1290-1298.

(2) Schutt, E. G.; Klein, D. H.; Mattrey, R. M.; Riess, J. G. Injectable Microbubbles as Contrast Agents for Diagnostic Ultrasound Imaging: The Key Role of Perfluorochemicals. *Angew. Chem., Int. Ed.* **2003,** *42* (28), 3218-3235.

(3) Lindner, J. R. Microbubbles in medical imaging: current applications and future directions. *Nat. Rev. Drug Discovery* **2004,** *3*, 527.

(4) Szabo, T. L. *Diagnostic ultrasound imaging: inside out*, 2nd ed.; Academic Press: 2013; p 832.

(5) Lo, A. H.; Kripfgans, O. D.; Carson, P. L.; Rothman, E. D.; Fowlkes, J. B. Acoustic droplet vaporization threshold: effects of pulse duration and contrast agent. *IEEE Trans. Ultrason., Ferroelectr., Freq. Control* **2007,** *54* (5), 933-946.

(6) Fabiilli, M. L.; Haworth, K. J.; Fakhri, N. H.; Kripfgans, O. D.; Carson, P. L.; Fowlkes, J. B. The role of inertial cavitation in acoustic droplet vaporization. *IEEE Trans. Ultrason., Ferroelectr., Freq. Control* **2009,** *56* (5), 1006-1017.

(7) Wang, J.; Barback, C. V.; Ta, C. N.; Weeks, J.; Gude, N.; Mattrey, R. F.; Blair, S. L.; Trogler, W. C.; Lee, H.; Kummel, A. C. Extended Lifetime In Vivo Pulse Stimulated Ultrasound Imaging. *IEEE Trans. Med. Imaging* **2017,** *37* (1), 222-229.

(8) Liberman, A.; Wang, J.; Lu, N.; Viveros, R. D.; Allen, C. A.; Mattrey, R. F.; Blair, S. L.; Trogler, W. C.; Kim, M. J.; Kummel, A. C. Mechanically Tunable Hollow Silica Ultrathin Nanoshells for Ultrasound Contrast Agents. *Adv. Funct. Mater.* **2015,** *25* (26), 4049-4057.

(9) Wang, X.; Chen, H.; Chen, Y.; Ma, M.; Zhang, K.; Li, F.; Zheng, Y.; Zeng, D.; Wang, Q.; Shi, J. Perfluorohexane-Encapsulated Mesoporous Silica Nanocapsules as Enhancement Agents for Highly Efficient High Intensity Focused Ultrasound (HIFU). *Adv. Mater.* **2012,** *24* (6), 785-791.

(10) Chen, Y.; Chen, H.; Sun, Y.; Zheng, Y.; Zeng, D.; Li, F.; Zhang, S.; Wang, X.; Zhang, K.; Ma, M.; He, Q.; Zhang, L.; Shi, J. Multifunctional Mesoporous Composite Nanocapsules for Highly Efficient MRI-Guided High-Intensity Focused Ultrasound Cancer Surgery. *Angew. Chem., Int. Ed.* **2011,** *50* (52), 12505-12509.

(11) Ma, M.; Xu, H.; Chen, H.; Jia, X.; Zhang, K.; Wang, Q.; Zheng, S.; Wu, R.; Yao, M.; Cai, X.; Li, F.; Shi, J. A Drug–Perfluorocarbon Nanoemulsion with an Ultrathin Silica Coating for the Synergistic Effect

of Chemotherapy and Ablation by High-Intensity Focused Ultrasound. *Adv. Mater.* **2014,** *26* (43), 7378-7385.

(12) An, L.; Hu, H.; Du, J.; Wei, J.; Wang, L.; Yang, H.; Wu, D.; Shi, H.; Li, F.; Yang, S. Paramagnetic hollow silica nanospheres for in vivo targeted ultrasound and magnetic resonance imaging. *Biomaterials* **2014,** *35* (20), 5381-5392.

(13) Wang, X.; Chen, H.; Zhang, K.; Ma, M.; Li, F.; Zeng, D.; Zheng, S.; Chen, Y.; Jiang, L.; Xu, H.; Shi, J. An Intelligent Nanotheranostic Agent for Targeting, Redox-Responsive Ultrasound Imaging, and Imaging-Guided High-Intensity Focused Ultrasound Synergistic Therapy. *Small* **2014,** *10* (7), 1403-1411.

(14) Wang, X.; Chen, H.; Zheng, Y.; Ma, M.; Chen, Y.; Zhang, K.; Zeng, D.; Shi, J. Au-nanoparticle coated mesoporous silica nanocapsule-based multifunctional platform for ultrasound mediated imaging, cytoclasis and tumor ablation. *Biomaterials* **2013,** *34* (8), 2057-2068.

(15) Yildirim, A.; Chattaraj, R.; Blum, N. T.; Goodwin, A. P. Understanding Acoustic Cavitation Initiation by Porous Nanoparticles: Toward Nanoscale Agents for Ultrasound Imaging and Therapy. *Chem. Mater.* **2016,** *28* (16), 5962-5972.

(16) Wu, H.; Shi, H.; Zhang, H.; Wang, X.; Yang, Y.; Yu, C.; Hao, C.; Du, J.; Hu, H.; Yang, S. Prostate stem cell antigen antibody-conjugated multiwalled carbon nanotubes for targeted ultrasound imaging and drug delivery. *Biomaterials* **2014,** *35* (20), 5369-5380.

(17) Feng, Q.; Zhang, W.; Yang, X.; Li, Y.; Hao, Y.; Zhang, H.; Hou, L.; Zhang, Z. pH/Ultrasound Dual-Responsive Gas Generator for Ultrasound Imaging-Guided Therapeutic Inertial Cavitation and Sonodynamic Therapy. *Adv. Healthcare Mater.* **2017,** *7* (5), 1700957-n/a.

(18) Jia, X.; Cai, X.; Chen, Y.; Wang, S.; Xu, H.; Zhang, K.; Ma, M.; Wu, H.; Shi, J.; Chen, H. Perfluoropentane-Encapsulated Hollow Mesoporous Prussian Blue Nanocubes for Activated Ultrasound Imaging and Photothermal Therapy of Cancer. *ACS Appl. Mater. Interfaces* **2015,** *7* (8), 4579-4588.

(19) Min, H. S.; Son, S.; Lee, T. W.; Koo, H.; Yoon, H. Y.; Na, J. H.; Choi, Y.; Park, J. H.; Lee, J.; Han, M. H.; Park, R.-W.; Kim, I.-S.; Jeong, S. Y.; Rhee, K.; Kim, S. H.; Kwon, I. C.; Kim, K. Liver-Specific and Echogenic Hyaluronic Acid Nanoparticles Facilitating Liver Cancer Discrimination. *Adv. Funct. Mater.* **2013,** *23* (44), 5518-5529.

(20) Liu, Y.; Ai, K.; Lu, L. Polydopamine and Its Derivative Materials: Synthesis and Promising Applications in Energy, Environmental, and Biomedical Fields. *Chem. Rev.* **2014,** *114* (9), 5057-5115.

(21) Wang, Z.; Carniato, F.; Xie, Y.; Huang, Y.; Li, Y.; He, S.; Zang, N.; Rinehart, J. D.; Botta, M.; Gianneschi, N. C. High Relaxivity Gadolinium-Polydopamine Nanoparticles. *Small* **2017,** *13* (43), 1701830-n/a.

(22) Wu, Q.; Niu, M.; Chen, X.; Tan, L.; Fu, C.; Ren, X.; Ren, J.; Li, L.; Xu, K.; Zhong, H.; Meng, X. Biocompatible and biodegradable zeolitic imidazolate framework/polydopamine nanocarriers for dual stimulus triggered tumor thermo-chemotherapy. *Biomaterials* **2018,** *162*, 132-143.

(23) Ju, K.-Y.; Lee, J. W.; Im, G. H.; Lee, S.; Pyo, J.; Park, S. B.; Lee, J. H.; Lee, J.-K. Bio-Inspired, Melanin-Like Nanoparticles as a Highly Efficient Contrast Agent for T1-Weighted Magnetic Resonance Imaging. *Biomacromolecules* **2013,** *14* (10), 3491-3497.

(24) Casula, M. F.; Conca, E.; Bakaimi, I.; Sathya, A.; Materia, M. E.; Casu, A.; Falqui, A.; Sogne, E.; Pellegrino, T.; Kanaras, A. G. Manganese doped-iron oxide nanoparticle clusters and their potential as agents for magnetic resonance imaging and hyperthermia. *Phys. Chem. Chem. Phys.* **2016,** *18* (25), 16848-16855.

(25) Ge, R.; Lin, M.; Li, X.; Liu, S.; Wang, W.; Li, S.; Zhang, X.; Liu, Y.; Liu, L.; Shi, F.; Sun, H.; Zhang, H.; Yang, B. Cu2+-Loaded Polydopamine Nanoparticles for Magnetic Resonance Imaging-Guided pH- and Near-Infrared-Light-Stimulated Thermochemotherapy. *ACS Appl. Mater. Interfaces* **2017,** *9* (23), 19706-19716.

(26) Wang, Z.; Xie, Y.; Li, Y.; Huang, Y.; Parent, L. R.; Ditri, T.; Zang, N.; Rinehart, J. D.; Gianneschi, N. C. Tunable, Metal-Loaded Polydopamine Nanoparticles Analyzed by Magnetometry. *Chem. Mater.* **2017,** *29* (19), 8195-8201.

(27) Li, Y.; Xie, Y.; Wang, Z.; Zang, N.; Carniato, F.; Huang, Y.; Andolina, C. M.; Parent, L. R.; Ditri, T. B.; Walter, E. D.; Botta, M.; Rinehart, J. D.; Gianneschi, N. C. Structure and Function of Iron-Loaded Synthetic Melanin. *ACS Nano* **2016,** *10* (11), 10186-10194.

(28) Cui, J.; Yan, Y.; Such, G. K.; Liang, K.; Ochs, C. J.; Postma, A.; Caruso, F. Immobilization and Intracellular Delivery of an Anticancer Drug Using Mussel-Inspired Polydopamine Capsules. *Biomacromolecules* **2012,** *13* (8), 2225-2228.

(29) Chen, X.; Yan, Y.; Müllner, M.; van Koeverden, M. P.; Noi, K. F.; Zhu, W.; Caruso, F. Engineering Fluorescent Poly(dopamine) Capsules. *Langmuir* **2014,** *30* (10), 2921-2925.

(30) Liu, Y.; Ai, K.; Liu, J.; Deng, M.; He, Y.; Lu, L. Dopamine-Melanin Colloidal Nanospheres: An Efficient Near-Infrared Photothermal Therapeutic Agent for In Vivo Cancer Therapy. *Adv. Mater.* **2013,** *25* (9), 1353-1359.

(31) Miao, Z.-H.; Wang, H.; Yang, H.; Li, Z.-L.; Zhen, L.; Xu, C.-Y. Intrinsically Mn2+-Chelated Polydopamine Nanoparticles for Simultaneous Magnetic Resonance Imaging and Photothermal Ablation of Cancer Cells. *ACS Appl. Mater. Interfaces* **2015,** *7* (31), 16946-16952.
(32) Huang, Y.; Vezeridis, A. M.; Wang, J.; Wang, Z.; Thompson, M.; Mattrey, R. F.; Gianneschi, N. C. Polymer-Stabilized Perfluorobutane Nanodroplets for Ultrasound Imaging Agents. *J. Am. Chem. Soc.* **2017,** *139* (1), 15-18.

(33) Picheth, G.; Houvenagel, S.; Dejean, C.; Couture, O.; Alves de Freitas, R.; Moine, L.; Tsapis, N. Echogenicity enhancement by end-fluorinated polylactide perfluorohexane nanocapsules: Towards ultrasound-activable nanosystems. *Acta Biomater.* **2017,** *64*, 313-322.

(34) Astafyeva, K.; Somaglino, L.; Desgranges, S.; Berti, R.; Patinote, C.; Langevin, D.; Lazeyras, F.; Salomir, R.; Polidori, A.; Contino-Pepin, C.; Urbach, W.; Taulier, N. Perfluorocarbon nanodroplets stabilized by fluorinated surfactants: characterization and potentiality as theranostic agents. *J. Mater. Chem. B* **2015,** *3* (14), 2892-2907.

(35) Yue, Q.; Wang, M.; Sun, Z.; Wang, C.; Wang, C.; Deng, Y.; Zhao, D. A versatile ethanol-mediated polymerization of dopamine for efficient surface modification and the construction of functional core-shell nanostructures. *J. Mater. Chem. B* **2013,** *1* (44), 6085-6093.

(36) Xu, L. Q.; Yang, W. J.; Neoh, K.-G.; Kang, E.-T.; Fu, G. D. Dopamine-Induced Reduction and Functionalization of Graphene Oxide Nanosheets. *Macromolecules* **2010,** *43* (20), 8336-8339.

(37) Cao, Y.; Zhang, X.; Tao, L.; Li, K.; Xue, Z.; Feng, L.; Wei, Y. Mussel-Inspired Chemistry and Michael Addition Reaction for Efficient Oil/Water Separation. *ACS Appl. Mater. Interfaces* **2013,** *5* (10), 4438-4442.

(38) Zhang, L.; Wu, J.; Wang, Y.; Long, Y.; Zhao, N.; Xu, J. Combination of Bioinspiration: A General Route to Superhydrophobic Particles. *J. Am. Chem. Soc.* **2012,** *134* (24), 9879-9881.

(39) Wang, B.; Liu, Y.; Zhang, Y.; Guo, Z.; Zhang, H.; Xin, J. H.; Zhang, L. Bioinspired Superhydrophobic Fe3O4@Polydopamine@Ag Hybrid Nanoparticles for Liquid Marble and Oil Spill. *Adv. Mater. Interfaces* **2015,** *2* (13), 1500234-n/a.

(40) Veith, G. M.; Dudney, N. J. Current collectors for rechargeable Li-air batteries. *J. Electrochem. Soc.* **2011,** *158* (6), A658-A663.

(41) Xie, Y.; Wang, J.; Wang, Z.; Krug, K. A.; Rinehart, J. D. Perfluorocarbon-loaded polydopamine nanoparticles as ultrasound contrast agents. *Nanoscale* **2018,** *10* (26), 12813-12819.

(42) Deshpande, N.; Needles, A.; Willmann, J. K. Molecular ultrasound imaging: current status and future directions. *Clin. Radiol.* **2011,** *65* (7), 567-581.

(43) Garg, S.; Thomas, A. A.; Borden, M. A. The effect of lipid monolayer in-plane rigidity on in vivo microbubble circulation persistence. *Biomaterials* **2013,** *34* (28), 6862-6870.

(44) Liberman, A.; Martinez, H. P.; Ta, C. N.; Barback, C. V.; Mattrey, R. F.; Kono, Y.; Blair, S. L.; Trogler, W. C.; Kummel, A. C.; Wu, Z. Hollow silica and silica-boron nano/microparticles for contrast-enhanced ultrasound to detect small tumors. *Biomaterials* **2012,** *33* (20), 5124-5129.

(45) Longmire, M.; Choyke, P. L.; Kobayashi, H. Clearance properties of nano-sized particles and molecules as imaging agents: considerations and caveats. *Nanomed.* **2008,** *3* (5), 703-717.

Chapter 4 Tuning the ultrasonic and photoacoustic response of PDA-stabilized perfluorocarbon contrast agents

4.1 Abstract

In this chapter, Fe^{3+}-loaded PDA ultrasound/photoacoustic contrast agents are developed to give them extra capability for imaging. contrast-enhanced ultrasound (CEUS) offers the exciting prospect of retaining the ease of ultrasound imaging while enhancing imaging clarity, diagnostic specificity, and theranostic capability. To advance the capabilities of CEUS, the synthesis and understanding of new ultrasound contrast agents (UCAs) is a necessity. Many UCAs are nano- or micro-scale materials composed of a perfluorocarbon (PFC) and stabilizer that synergistically induce an ultrasound response that is both information-rich and easily differentiated from natural tissue. In this work, we probe the extent to which CEUS is modulated through variation in a PFC stabilized with fluorine-modified polydopamine nanoparticles (PDA NPs). The high level of synthetic tunability in this system allows us to study signal as a function of particle aggregation and PFC volatility in a systematic manner. Separation of aggregated and non-aggregated nanoparticles lead to a fundamentally different signal response, and for this system, PFC volatility has little effect on CEUS intensity despite a range of over 50°C in boiling point. To further explore the imaging tunability and multimodality, Fe^{3+}-chelation was employed to generate an enhanced photoacoustic (PA) signal in addition to the US signal. *In vitro* and *In vivo* results demonstrate that PFC-loaded PDA NPs show stronger PA signal than the non-PFC ones, indicating that the PA signal can be used

for in situ differentiation between PFC-loading levels. In sum, these data evince the rich role synthetic chemistry can play in guiding new directions of development for UCAs.

4.2 Introduction

In many ways, ultrasonography is an ideal medical imaging technique – equipment and maintenance costs are comparatively minor, safety concerns are minimal, portability is high, and time resolution can exceed high-frame-rate cinema by orders of magnitude. As a complement to more intensive techniques such as magnetic resonance imaging (MRI), positron emission tomography (PET) and computed tomography (CT), US has become ubiquitous in diagnostic imaging.[1-4] By introducing an ultrasound contrast agent (UCA), utility can be further enhanced, allowing better tracking of blood flow rates, sharpening of contrast in tissue density, and enhanced resolution.[5-6] Although there are many ways in which an ultrasound wave can interact with a contrast agent to generate a detectable signal, they involve classical wave mechanics describing the motion, density, and elasticity of the agent relative to the medium. Thus, a balance must be struck between tissue penetration, signal resolution, and contrast with surrounding tissue. Strong contrast signals at common ultrasound transducer frequencies can be obtained with inert gases or encased volatile liquid droplets due to their low densities relative to biological tissue. Many commercial ultrasound agents employ perfluorocarbons (PFC) stabilized by protein, polymer or lipid shells, as these are biocompatible and their compressibility and low boiling point enhances the interaction with ultrasound energy.[7-9] While ideal for many applications, US contrast agents of this type have several limiting factors. One challenge is fine-tuning the strength of PFC encapsulation. Weaker encapsulation leads to strong bursts of contrast with minimal ultrasound power, but it also limits the useful imaging time window due to the volatility of PFC. Another challenge is the synthetic complexity required for tuning the ultrasonic response, altering the size, or introducing new functionality.

Previously we demonstrated a system where instead of encapsulation within a core-shell structure, PFC could be stabilized in aqueous suspension by association with non-porous polydopamine nanoparticles (PDA NPs) functionalized with a perfluorinated alkane.[10] This system shows a surprisingly strong and long-lived contrast response with reasonable colloidal stability, which may arise from the balance of fluorous components (PDA NPs and PFC) and polar components (PDA NPs and H_2O).[11-12] This long-lived, strong signal and highly tunable synthetic platform offers an intriguing system to explore both the fundamental nature of the acoustic response and the extent to which its properties can be enhanced for potential implementation in CEUS. To advance these aims, we have improved upon our initial synthetic methods to prepare 1H,1H,2H,2H-perfluorodecanethiol-functionalized PDA with better aqueous colloidal stability and greater control over aggregation. Importantly, our new synthetic methods allow study of how aggregation of PDA/PFC within aqueous suspension affects the ultrasound response. Results show that there is a fundamentally different power response between the isolated particles and Pickering microscale emulsion aggregates in the colloidal suspension of our material.[13-15] Additionally, this work explores the ways in which imaging contrast, stability, and multimodality are controlled and enhanced including introduction of chelating metals, decreased PFC volatility, and long timescale storage and measurement of materials. We probe the system's durability under *ex vivo*, *in vitro* cell viability, and *in vivo* conditions and its multimodality with photoacoustic (PA) contrast–a hybrid technique that combines optical contrast and acoustic spatial/temporal resolution.[16-17] The combination of PDA-based imaging by CEUS and PA adds additional modalities to complement and track the myriad biomedical applications currently under exploration for PDA and other synthetic melanin particles.[18-24]

4.3 Results and Discussions

4.3.1 Preparation and Characterization of PDAF-i% NPs

PDA NPs with chelated Fe(III) ions were synthesized by a modification of a previously reported method (Figure 4.1a).[25] Briefly, $FeCl_3$ and 2-(3,4-dihydroxyphenyl)ethylamine (dopamine) were dissolved in a 1:5 ethanol:H_2O solution and allowed to oxidatively polymerize under basic conditions (initial pH around 10.2) for 24 h.

Isolated PDA-Fe NPs were made fluorophilic through post-synthetic attachment of 1H,1H,2H,2H-Perfluorodecanethiol via thiol Michael addition (PDAF-i%, i represents the weight percent of Fe^{3+}, i = 0.13, 1.0, 1.7, 2.4). Size and morphology of the modified particles were determined by transmission electron microscope (TEM) and scanning electron microscope (SEM) (Figure 4.1b-f, 4.2). With increasing initial Fe^{3+} concentration, the final NP sizes were found to show some increase in the final size (PDAF-0.13%, d = 85±6 nm; PDAF-1.0%, d = 103±12 nm; PDAF-1.7%, d = 95±13 nm; PDAF-2.4%, d = 137±15 nm). Weight percentages of the Fe^{3+} cation concentration were determined by inductively coupled plasma mass spectrometry (ICP-MS). Further decreasing the initial Fe^{3+} ion concentration does not lower the amount incorporated, nor does it decrease the NP size (Figure 4.3). As discussed in previous studies,[18] when present during the polymerization, Fe^{3+} cation distribution in PDA is roughly homogeneous. Scanning transmission electron microscopy with energy-dispersive X-ray spectroscopy (STEM-EDS) confirm that this is also true for our NPs (Figure 4.1g, 4.1h).
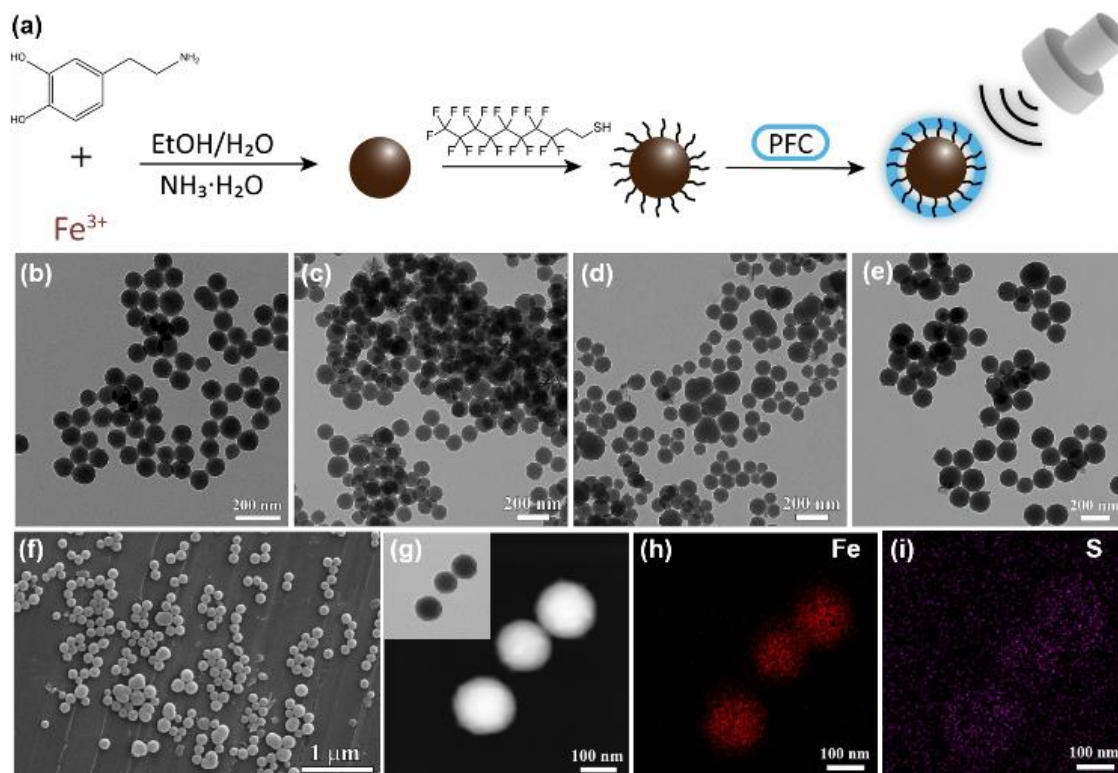
Figure 4.1 (a) Schematic illustration of the synthetic procedure of PDAF-*i*% NPs. TEM images of (b) PDAF-0.13% NPs, (c) PDAF-1.0% NPs, (d) PDAF-1.7% NPs, (e) PDAF-2.4% NPs, (f) SEM image of PDAF-2.4%, (g) HAADF-STEM image of PDAF-2.4% NPs with an inset of TEM image of (e), and elemental mapping of (h) Fe, (i) S elements on PDAF-2.4% NPs.
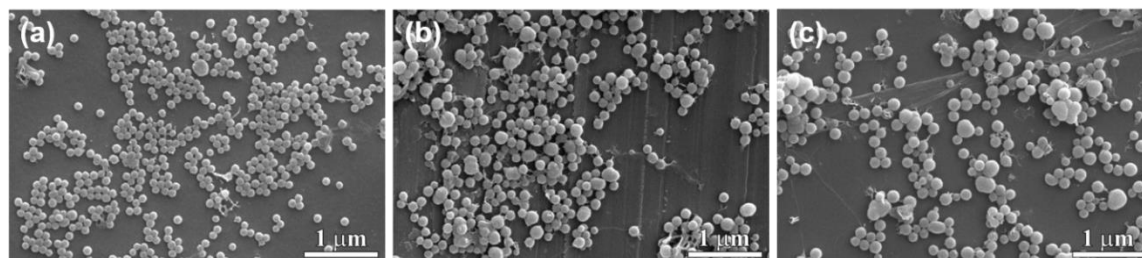
Figure 4.2 SEM images for (a) PDAF-0.13%, (b) PDAF-1.0%, (c) PDAF-1.7%.
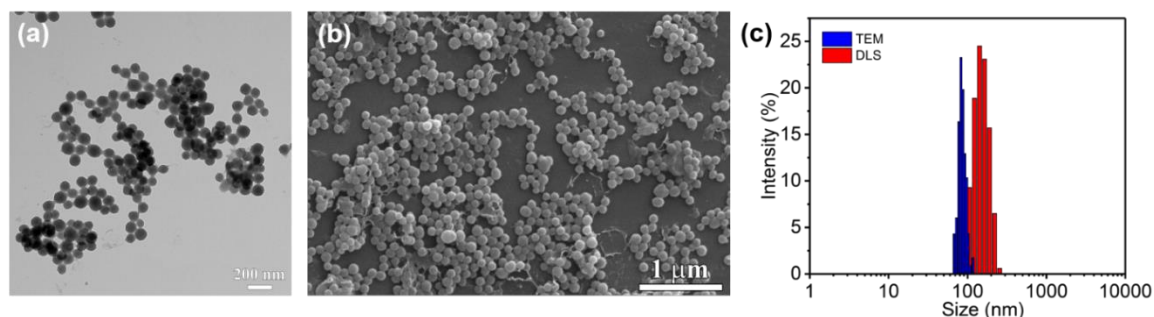
Figure 4.3 Comparison of structural data for a representative sample of PDAF NPs doped to 0.14% Fe ion content by ICP-MS analysis with 6 mg of initial $FeCl_3$ loading amount. (a) TEM, (b) SEM, and (c) comparative analysis of diameters determined by TEM and DLS.

SEM images (Figure 4.1f and 4.2) confirm the spherical morphology and lack of significant cross-linking of particles as observed in our previous results.[10] In fact, no significant morphological or size alterations were observed after 1H,1H,2H,2H-perfluorodecanethiol functionalization, indicating that these steps are independently modifiable without the need for re-optimization of the overall experimental parameters (Figure 4.4). As the imaging properties of UCAs strongly depend on the particle aggregation state, dynamic light scattering (DLS) measurements were used to compare the hydrodynamic and physical sizes measured by TEM analysis. The hydrodynamic radii displayed by PDAF-i% display expected diameter increases that are still consistent with minimal aggregation and low polydispersity (PDAF-0.13%, $d_H = 167\pm57$ nm, PDI = 0.117; PDAF-1.0%, $d_H = 196\pm53$ nm, PDI = 0.074; PDAF-1.7%, $d_H = 214\pm55$ nm, PDI = 0.067; PDAF-2.4%, $d_H = 202\pm57$ nm, PDI = 0.081, Figure 4.5). Zeta potentials of PDAF-0.13%, PDAF-1.0%, PDAF-1.7%, and PDAF-2.4% were -32.2 ± 0.2, -30.4 ± 1.9, -35.3 ± 0.2, -31.6 ± 0.4 mV, respectively, indicating good stability in aqueous solution. After PFP loading, DLS data show a detectable level of aggregation in PDAF-1.0% (PDI = 0.204) and PDAF-2.4% (PDI = 0.284), which is postulated to arise from condensation of "Pickering" PDAF-stabilized PFP-emulsion droplets in the aqueous phase (Figure 4.6).
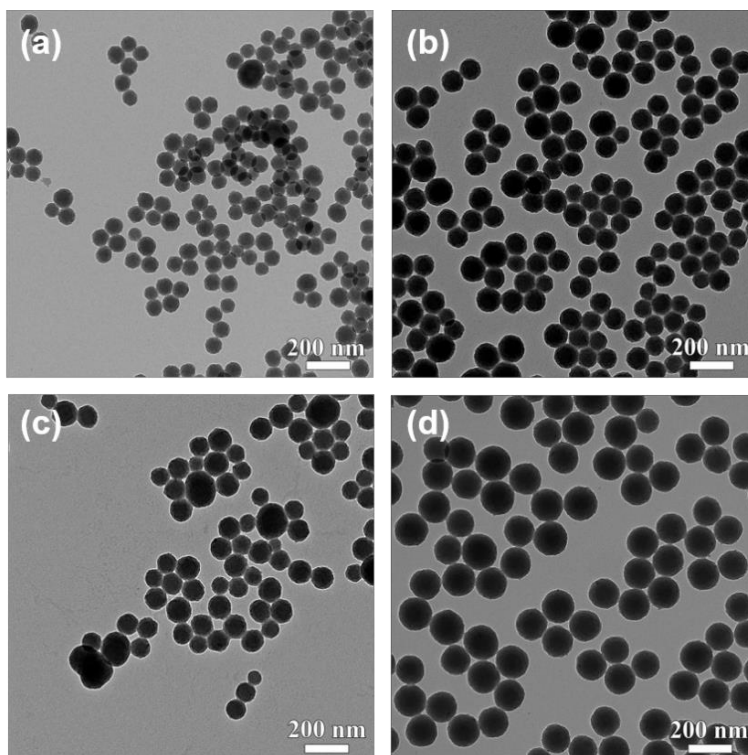
Figure 4.4 TEM images for (a) PDA-Fe-0.13%, (b) PDA-Fe-1.0%, (c) PDA-Fe-1.7%, (d) PDA-Fe-2.4%.
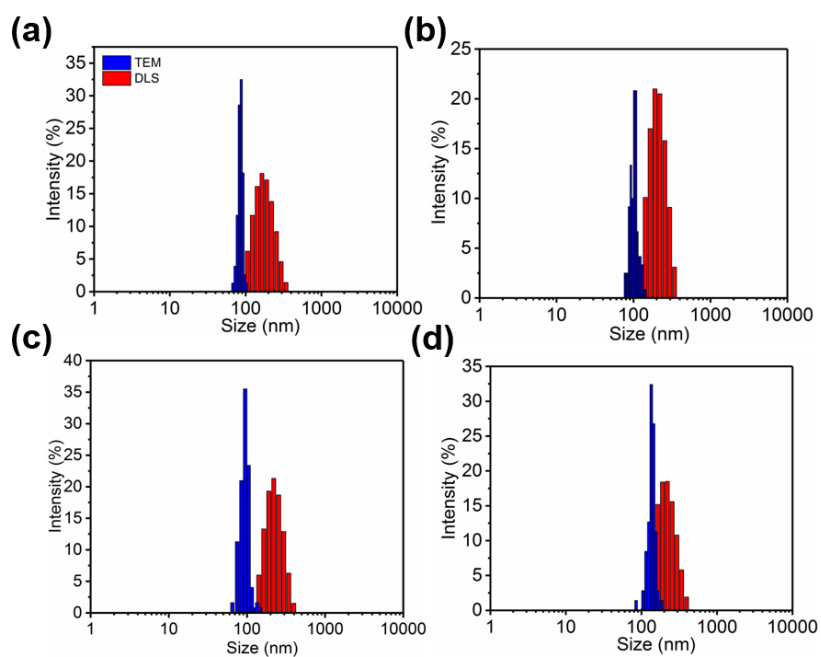
Figure 4.5 Comparison between the particle and hydrodynamic diameters as measured by TEM and DLS for (a) PDAF-0.13%, (b) PDAF-1.0%, (c) PDAF-1.7%, (d) PDAF-2.4%.
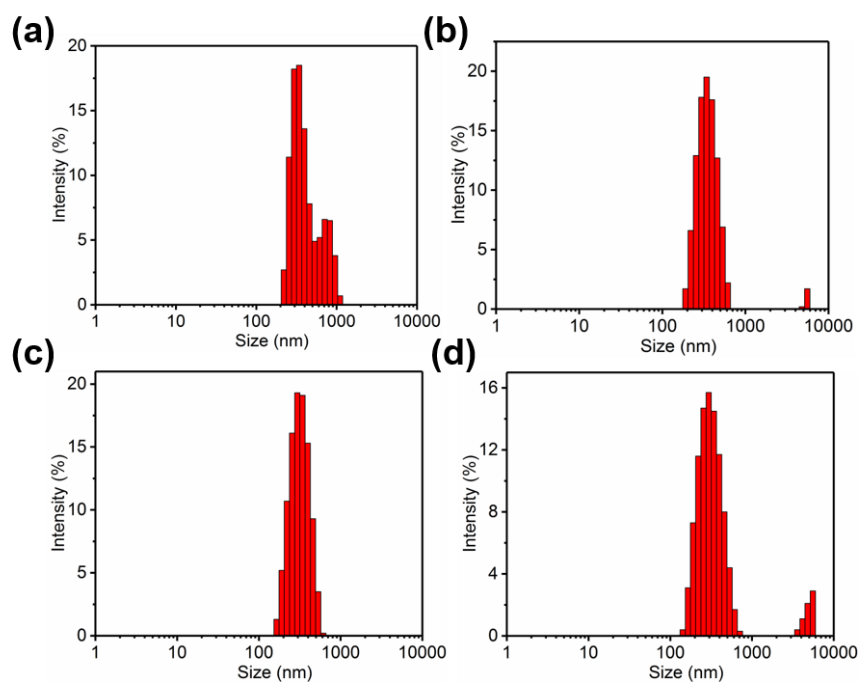
Figure 4.6 DLS size distributions of PFP-loaded (a) PDAF-0.13%, (b) PDAF-1.0%, (c) PDAF-1.7%, (d) PDAF-2.4%.

To further confirm the successful functionalization of the surface of PDA-Fe NPs with 1H,1H,2H,2H-perfluorodecanethiol, energy-dispersive X-ray spectroscopy (EDS) was employed for elemental analysis (Figure 4.7). The wt. % of sulfur is similar for all NP samples (4.0% for PDAF-0.13%, 3.7% for PDAF-1.0%, 2.3% for PDAF-1.7% NPs, and 3.7% for PDAF-2.4%) and indicates a surface coverage of 0.84 ± 0.19 S/nm^2. STEM-EDS mapping of S element shows that S element is present uniformly on the PDAF-2.4% NPs, consistent with intact incorporation (Figure 4.1i). To characterize fluorine in the PDA sample, X-ray photoelectron spectroscopy (XPS) was performed. The binding energy of 688 eV was attributed to the fluorine of perfluorodecanethiol (Figure 4.8).[26]
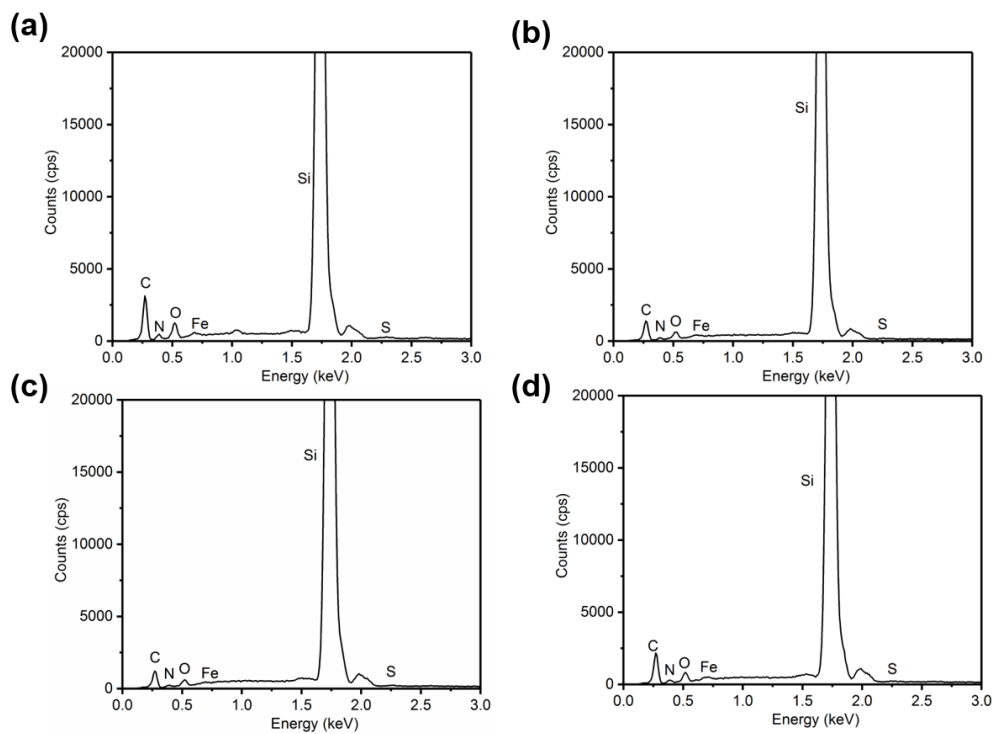
Figure 4.7 EDS spectrum of (a) PDAF-0.13%, (b) PDAF-1.0%, (c) PDAF-1.7%, (d) PDAF-2.4%.
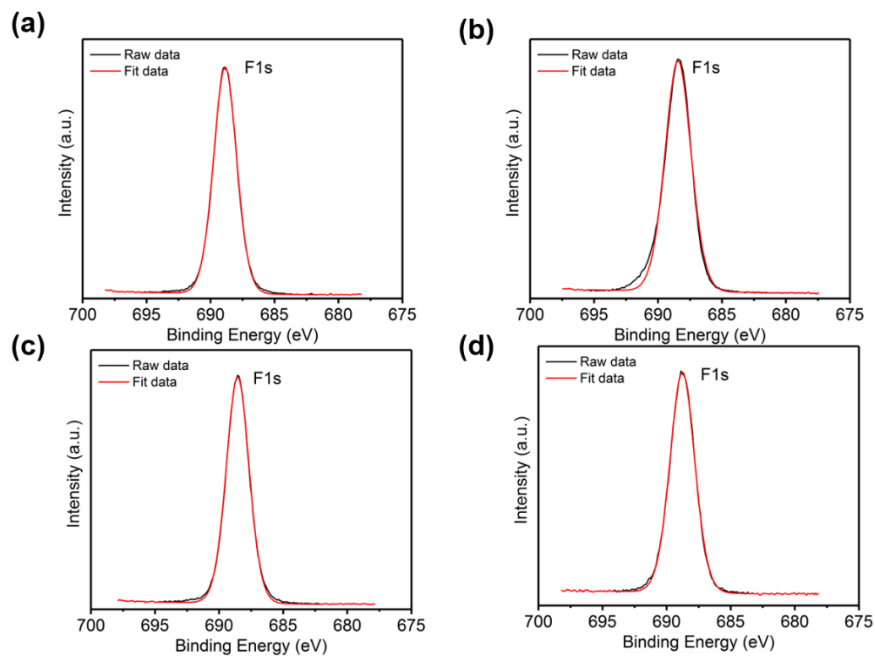
Figure 4.8 F1s XPS spectra of (a) PDAF-0.13%, (b) PDAF-1.0%, (c) PDAF-1.7%, (d) PDAF-2.4%.

4.3.2   In vitro Ultrasound Imaging Study of PDAF-i% NPs

To activate PDAF-*i*% NPs for use as UCAs, they must be loaded with a US responsive volatile liquid. Perfluorocarbons (PFCs) were chosen for their proven safety, chemical inertness, and ultrasound responsivity at common medical transducer frequencies.[8]   In our previous work, 1H,1H,2H,2H-perfluorodecanethiol functionalization of PDA was shown to associate with and stabilize perfluoropentane (PFP, $T_b = 28°C$) in aqueous solution, thus PFP was employed to benchmark the basic capabilities of PDAF-*i*% NPs by two important UCA modalities: color Doppler and contrast pulse sequence (CPS) imaging (Figure 4.9). Color Doppler is the imaging signal arising from a blue or red shift of the transducer frequency usually attributed to the Doppler effect caused by fluid motion.[27] As it shows strong and directional contrast in the presence flow, its most common use is cardiac imaging.[28] Non-flowing UCA samples can also show color Doppler signal where it appears as a high-contrast speckle pattern of random Doppler shifts.[29] Strong color Doppler signal is observed for all PDAF-*i*% samples with peak brightness at the maximum mechanical index (MI = 1.9) (Figure 4.9, 4.10a-b). Although speckle patterns are difficult to quantify, the image quality roughly scaled with the particle size, with PDAF-0.13% showing the weakest signal and PDAF-2.4% showing the strongest. This trend is logical, given that stronger acoustic cavitation and nonlinear backscattering is expected for larger particles.[9, 30] Compared to our previous fluorinated PDA UCAs,[10] PDAF-*i*% shows stronger color Doppler signal and better colloidal stability. These properties are likely due to the post-synthetic F-functionalization method which prevents interparticle crosslinking during the initial particle synthesis. PFP-loaded PDA-Fe particles without fluorine functionalization and PFP-H_2O emulsion mixtures without any particles, were also imaged using color Doppler mode. Unfunctionalized PDA NPs exhibit no color Doppler signal even at MI = 1.9, indicating that both PFP and the functionalization to induce fluorophilic stabilization are required to generate signal (Figure 4.9a and 4.10c-e). PFP-H_2O control samples also show no signal up to MI = 1.9 without stabilizing PDAF-*i*% (Figure 4.11), demonstrating the importance of the particle in stabilizing the volatile PFP.
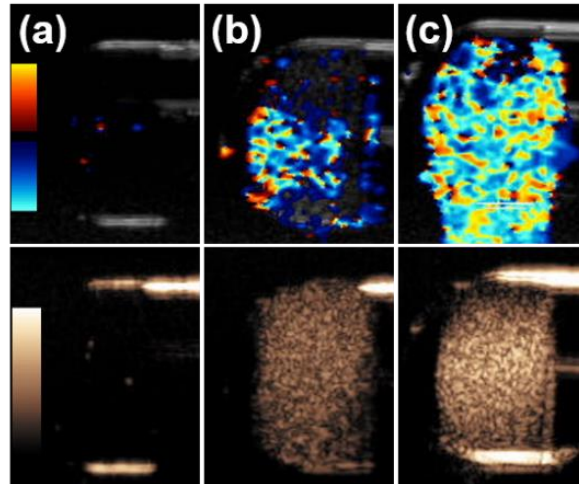
Figure 4.9 Color Doppler (up) and CPS imaging (down) of PFP-loaded (a) PDA-Fe-2.4%, (b) PDAF-0.13%, (c) PDAF-2.4% (MI = 1.9). For Color Doppler, black corresponds to no frequency shift. Warm and cool colors represent opposing frequency shifts. The grayscale signal is from simultaneously-collected B-mode imaging. For CPS images, black and white represent minimum and maximum signal intensity.
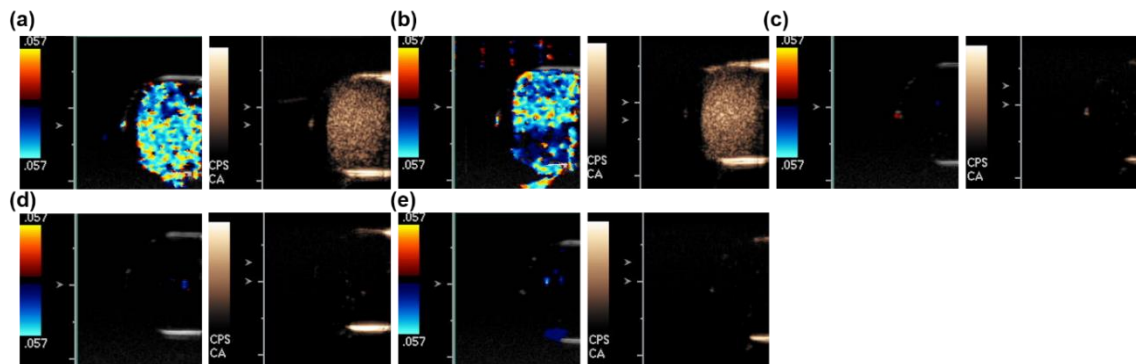
Figure 4.10 Color Doppler and CPS imaging of PFP-loaded (a) PDAF-1.0 %, (b) PDAF-1.7%, (c) PDA-Fe-0.13%, (d) PDA-Fe-1.0%, and (e) PDA-Fe-1.7% at room temperature with MI=1.9.
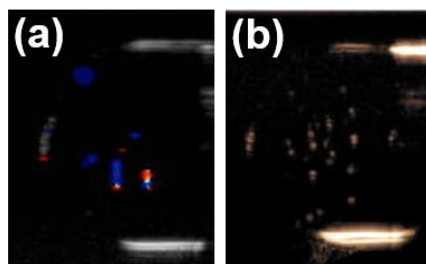
Figure 4.11 Color Doppler and CPS imaging of (a) PFH-loaded, (b) PFB-loaded PDAF-2.4% NPs at 7 MHz at room temperature with MI=1.9.

In addition to color Doppler, PDAF-i% were imaged using the Contrast Pulse Sequence (CPS) method. In this method, the non-linear ultrasound response of PFCs due to expansion and contraction is exploited to detect shifts in the phase angle. By subtraction of the linear response, virtually back-ground-free signals can be obtained. Figure 4.9b-c (bottom) and 4.10a-b show representative CPS images for PDAF-i% with the golden grain pattern quantifying clear CPS response from all samples (Figure 4.12a-d). Quantification is performed by averaging pixel intensities such that a fully saturated signal area will result in an intensity of 255. Room temperature values for PDAF-i% at mechanical index (MI) = 1.9 fall in the range of 60-100 (Figure 4.12a-d), comparable to PFC-loaded hollow silica, and commercial UCAs. [10, 27]
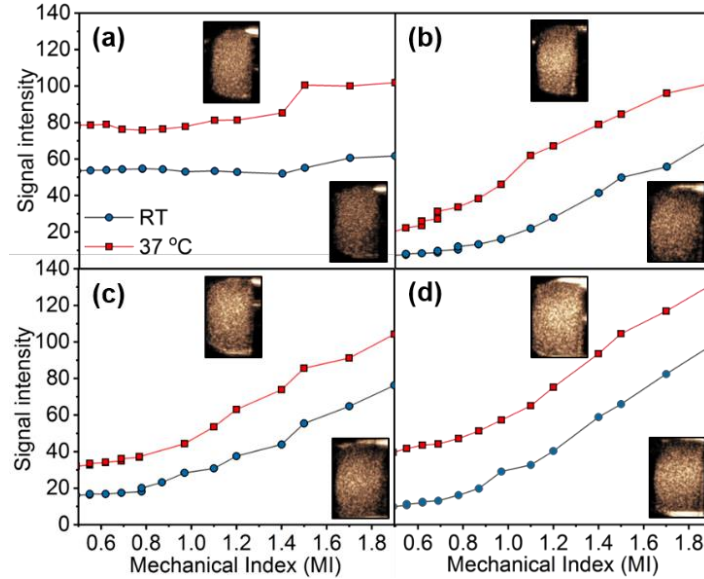
Figure 4.12 CPS signal brightness versus Mechanical Index (MI) for (a) PDAF-0.13% NPs, (b) PDAF-1.0% NPs, (c) PDAF-1.7% NPs, and (d) PDAF-2.4%; The MI is a unitless measure of the maximum reduction in pressure induced by the ultrasound wave defined as MI = peak negative pressure / √(center frequency of the US beam). Signal brightness is determined by averaging the 8-bit pixel intensities over equivalent ROI for all data. Images in inset are representative CPS data at MI=1.9 for each sample.

The interaction between the PFC and PDAF is crucial to stability and the timescale of imaging. It is expected from previous results on PFH nanoemulsions,[9] that the imaging characteristics will be altered by changes in available thermal energy. To ensure that our UCAs are viable at body temperature, color Doppler and CPS imaging was performed at 37°C with all other experimental conditions identical (Figure 4.12, 4.13). At higher temperature, PDAF-*i*% show enhanced signals at all MI, with maximum enhancements over room temperature values by 34%. Color Doppler is also shown with transducer signals requiring less than half of the power those at room temperature (MI = 0.87 vs. MI = 1.9, Figure 4.13).
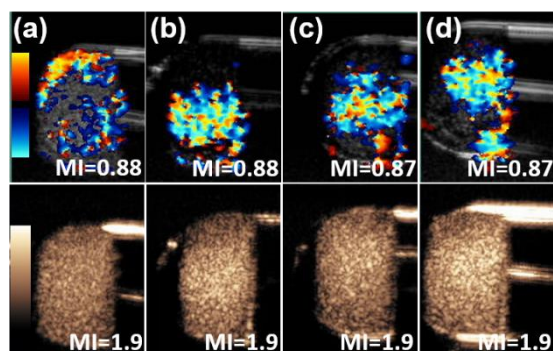
Figure 4.13 Color Doppler and CPS imaging of (a) PDAF-0.13% NPs, (b) PDAF-1.0% NPs, (c) PDAF-1.7% NPs, (d) PDAF-2.4% NPs at 37°C.

These results demonstrate that the interaction between PFP and PDAF-i% is strong enough to maintain stability at body temperature, where the PFP response to 7 MHz US is significantly enhanced. The nature of this stabilization is complex but has been demonstrated in biphasic molecular solutions.[31-32] Prior to 1H,1H,2H,2H-perfluorodecanethiol functionalization, the PDA forms a colloidal suspension that is stabilized by the negative zeta potential. This provides the polarity necessary for solvation by water and the Coulombic repulsion required to prevent particle aggregation. Upon functionalization with 1H,1H,2H,2H-perfluorodecanethiol, the fluorous areas of the PDAF-i% surface become the most stable position for PFP loading. If this loading process induces PDAF-i% aggregation, surface-stabilized Pickering emulsions will form (*vide infra*). To demonstrate the importance of the fluorophilic interaction to stabilization, PFP-loading was attempted on samples of PDA-Fe prior to fluorine functionalization. Negligible color Doppler signal was observed at room temperature, confirming that PFP is not retained in this case (Figure 4.9a and 4.10c-e).

Given that the robust nature of the fluorophilic stabilization provided by PDAF-i% permits strong imaging signals even with elevated temperatures, we were interested in whether we could utilize PFCs with widely differing physical properties to alter the UCA without any redesign of the particle itself. This would increase their versatility towards different imaging targets emphasizing

deep tissue penetration (low frequency) or high resolution (high frequency). For example, Goodwin et al. reported that greater MI was required to induce the vaporization of PFH than PFP, such that high intensity focused ultrasound (HIFU) was required.[33] As probes of the versatility of our particles, both PFCs with enhanced (perfluorobutane (PFB), T_b = −1.7°C) and diminished (perfluorohexane (PFH), T_b = −56°C) volatility were imaged using color Doppler and CPS modalities (Figure 4.14). Despite a range of over 50°C in T_b, the imaging characteristics are remarkably stable (Figure 4.15), quantitatively in the range of 80-100 at MI = 1.9. These data indicate that a mechanism other than irreversible cavitation may be leading to imaging contrast from these materials, since bubble dynamics will depend strongly on the physical characteristics of the PFC. If imaging can occur without PFC dissolution from the NP, then it may be possible to design UCAs that image persistently until cleared.
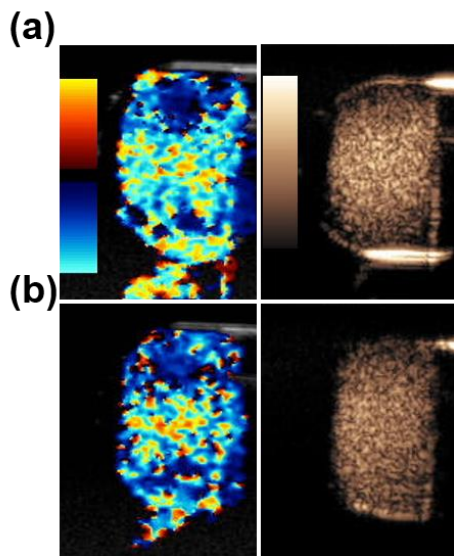
Figure 4.14 Color Doppler and CPS imaging of (a) PFH-loaded, (b) PFB-loaded PDAF-2.4% NPs at 7 MHz at room temperature with MI=1.9.
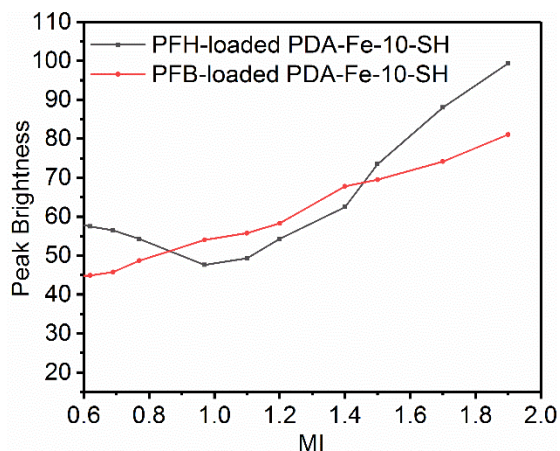
Figure 4.15 Quantitative plot of brightness for CPS imaging of PFH-loaded and PFB-loaded PDAF-2.4% NPs at room temperature.

To test long-term continuous imaging capability, PFP-loaded PDAF-i% were subjected to continuous MI = 1.5 and 1.9 color Doppler imaging (Figure 4.16). Commercial UCAs can generally be imaged for less than 30 min before losing signal,[34] yet PDAF-2.4% exhibited 6 h of imaging lifetime without dropping to background levels. Given the ability to stabilize during continuous imaging, periodic imaging after long-term storage was also tested. Storage of pre-mixed UCA is generally not possible due to the volatility of PFCs, and so a kit is required to form emulsions for immediate use. To test the stability of PFP-loaded PDAF-i%, fully prepared samples in aqueous solution were stored at 4°C and imaged over the course of 50 d (Figure 4.17). Both color Doppler imaging and CPS remain strong after 50 d indicating long shelf life.
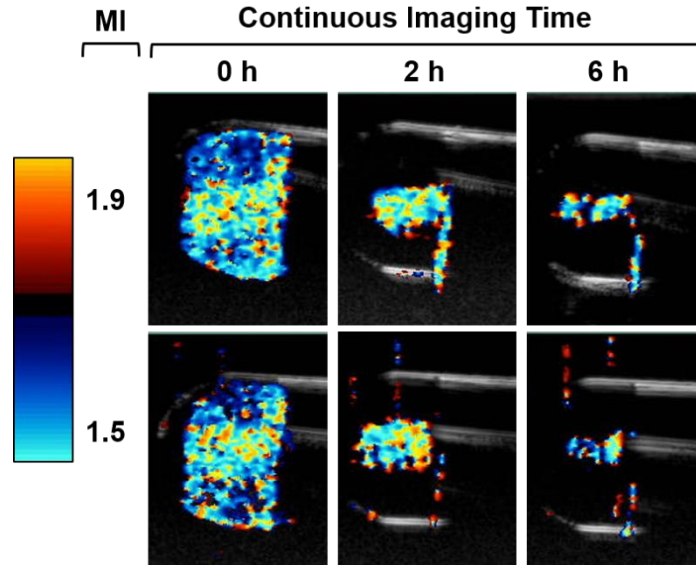
Figure 4.16 Continuous color Doppler imaging of PDAF-2.4% detected at room temperature with MI=1.9 and MI=1.5.
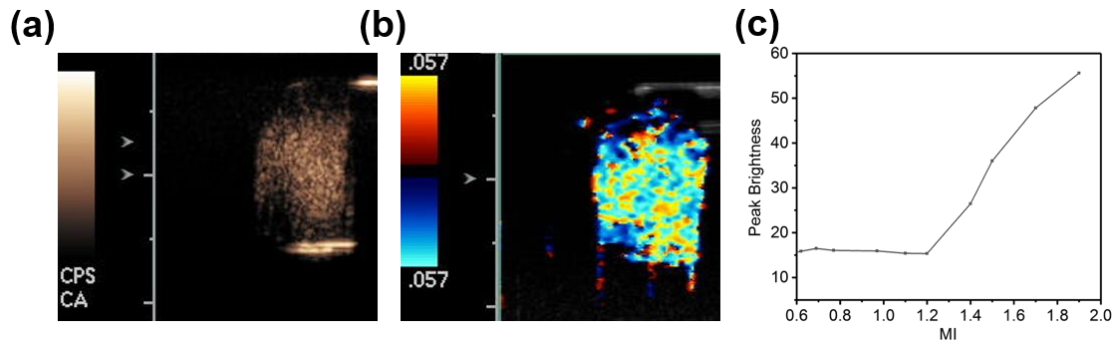
Figure 4.17 50-day storage lifetime test of PDAF-2.4% NPs using (a) CPS imaging, (b) color Doppler imaging, and (c) quantitative analysis of brightness for CPS imaging versus MI.

As shown in Figure 4.6, some amount of aggregation is demonstrated to occur after PFP loading. The ultrasound mechanism and optimization strategy of microparticle and nanoparticle UCAs is fundamentally different and thus determining the signal derived from each subpopulation of PDAF sample is important. In order to distinguish the contribution of ultrasound signal between small nanoparticles and large aggregates, the PFP-loaded PDAF-2.4% particles were separated by low speed centrifugation (2500 rpm, 3 min). Sub-populations from supernatant (named as PDAF-small) and precipitate (PDAF-large) were

collected and compared with the original sample (PDAF-mix). DLS data (Figure 4.18a-c) shows that the hydrodynamic size of PDAF-small (d = 256 nm; PDI = 0.11) is comparable to the non-PFP loaded sample (202 nm, PDI = 0.081; Figure 4.5d). Both PDAF-large and PDAF-mix (Figure 4.18b-c) show aggregation with many particles in the 1-5 µm range as expected from the original DLS data (Figure 4.6). In addition to DLS, we performed optical microscopy on particles before, during, and after exposure to 5 MHz ultrasound excitation (Figure 4.19). While aggregates were observable in PDAF-large and PDAF-mix, the application of ultrasound did not induce further aggregation in the system. The organization of solid particles to stabilize an interface, known as a Pickering emulsion,[35] has been incorporated into ultrasound contrast agents in a number of systems.[36-37] To investigate whether the observed aggregates were the source of ultrasound contrast in our samples, individual size sub-populations were analyzed by ultrasound contrast techniques.
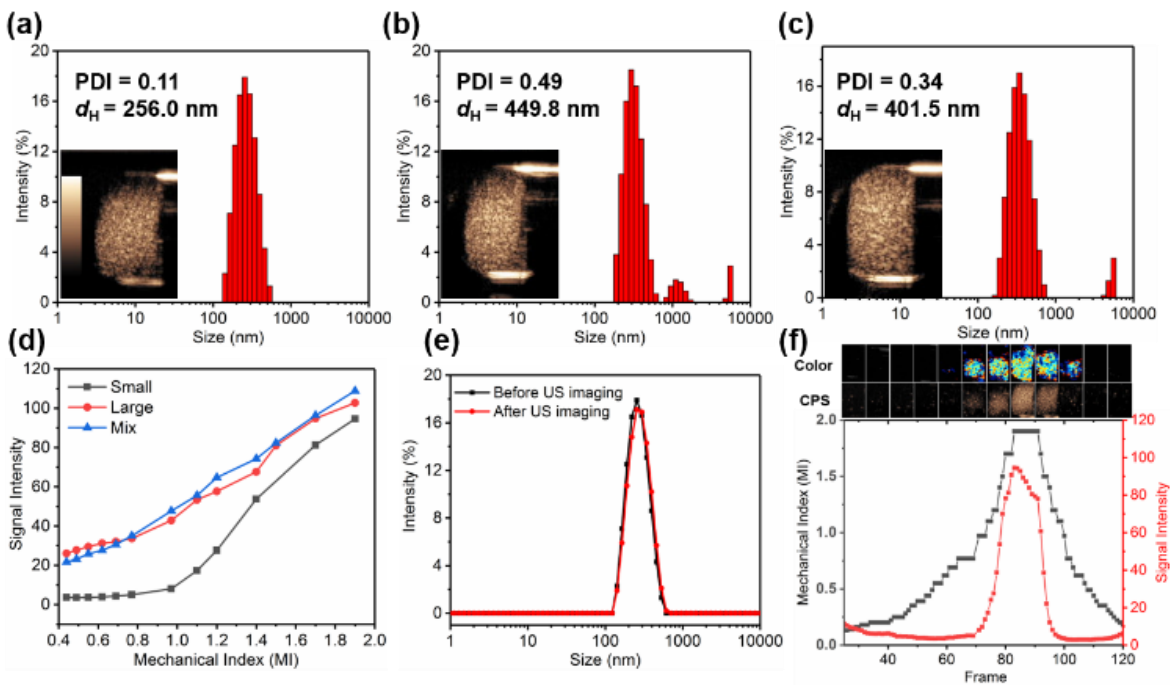
Figure 4.18 DLS size distribution of PFP-loaded (a) PDAF-small, (b) PDAF-large, (c) PDAF-mix with the insets of CPS imaging. (d) Quantitative plot of signal intensity for CPS imaging for PFP-loaded PDAF-small, PDAF-large and PDAF-mix. (e) DLS size distribution of PFP-loaded PDAF-small before and after three cycles of ultrasound imaging. (f) Quantitative analysis of image signal intensity (red) and MI (black) versus frame number for CPS imaging of PFP-loaded PDAF-small particles. The insets are corresponding color doppler and CPS images according to different frame number.
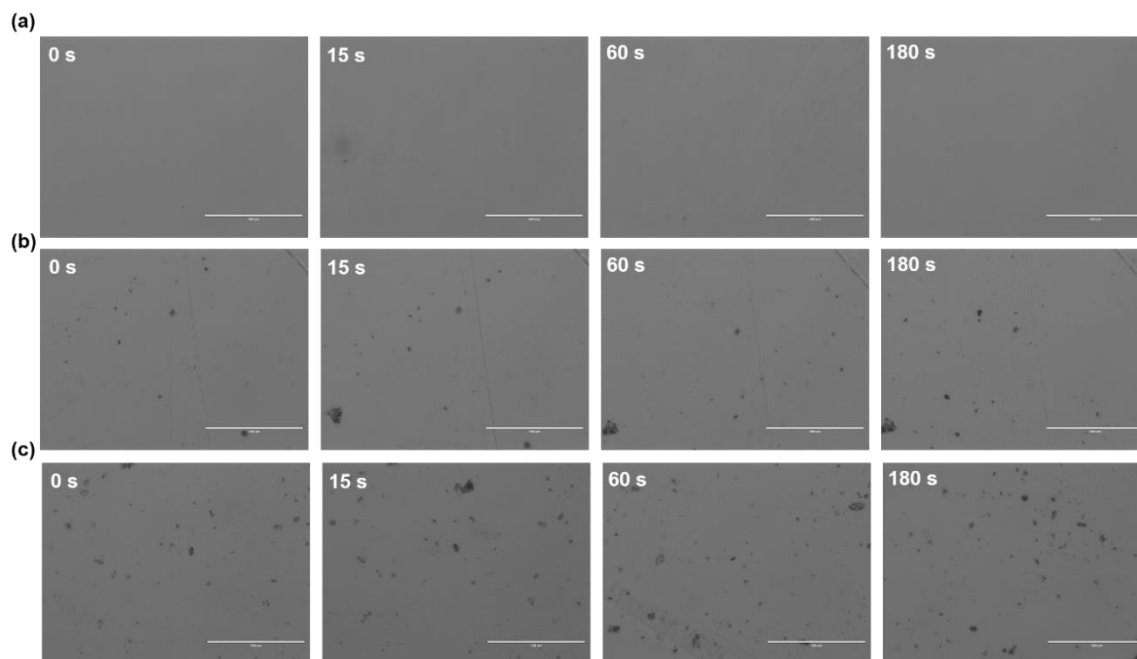
Figure 4.19 Optical microscope images of PFP-loaded (a) PDAF-small, (b) PDAF-large, and (c) PDAF-mix under 5 MHz ultrasound for different time. Scale bar represents 100 μm.

After confirming the aggregation state by DLS and optical microscopy, immediate CPS and color Doppler imaging studies were performed on PDAF-small, PDAF-large, and PDAF-mix (Qualitative CPS and color Doppler images were shown in insets of Figure 4.18a-c, 4.20c). All samples show strong signal indicative of the presence of an effective contrast agent. By quantitative analysis of CPS data (Figure 4.18d), both PDAF-large and PDAF-mix demonstrate an enhancement over the signal intensity of PDAF-small, as aggregated particles could contribute strong ultrasound contrast;[38] however, this difference decreases with increasing MI and is largely gone by MI = 1.9. It could be inferred from this data that PDAF-small is forming aggregation with increasing MI, and thus the similarity at high MI is simply a result of converting PDAF-small into PDAF-large. However, the DLS data shows remarkably stable particle size distribution before and after ultrasound imaging (Figure 4.18e), and the MI measurement can be cycled repeatedly without a change in the signal response (Figure 4.20d-e). Perhaps the most interesting finding from the aggregation study is the starkly different curvature to the MI-response between samples. While both PDAF-mix and PDAF-large show a roughly linear signal response to increased MI (Figure 4.18d, Figure 4.20a-b),

PDAF-small shows negligible response levels until MI = 1.0. At MI > 1.0, the response begins to rapidly increase with MI (Figure 4.18d). This behavior is seen more clearly when MI and CPS signal are plotted vs individual frame number (Figure 4.18f, 4.20d-e). Both CPS and Doppler signals show a "turn on" response consistently around MI = 1.0. Since the transducer frequency is fixed for these studies, this corresponds to either a threshold peak negative pressure (PNP) or a threshold MI (MI = PNP / √center frequency) for this UCA formulation. Overall, these data suggest that both small particles (PDAF-small) and large aggregation (PDAF-large) can contribute ultrasound signal in our system, though their signals have important fundamental differences that will be the subject of future study. For the remainder of the studies discussed, the unseparated PDAF-mixed samples will be used except where explicitly indicated.
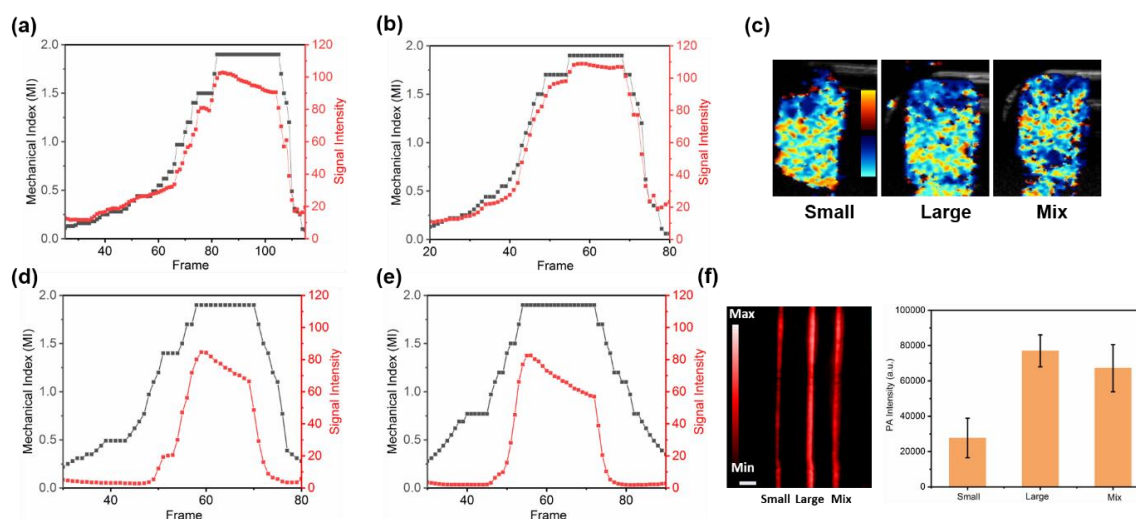
Figure 4.20 Quantitative analysis of image signal intensity and MI versus frame number for CPS imaging of PFP-loaded (a) PDAF-large, and (b) PDAF-mix. (c) Corresponding color Doppler images for PDAF-small, PDAF-large, and PDAF-mix. Quantitative analysis of (d) second, (e) third cycle of CPS imaging for PDAF-small particles (Figure 5f is the first cycle). (f) PA imaging of PFP-loaded PDAF-small, PDAF-large, and PDAF-mix, and their quantitative analysis of PA signal. Scale bar = 3 mm.

4.3.3 Ex vivo Ultrasound Study of PDAF-i% NPs

Previous results have demonstrated that the imaging characteristics of PDA translate well between aqueous solution, biological buffer, serum, and *ex vivo* tissue.[10, 22] To ensure the stable and bright contrast of PDAF-*i*% are not limited to solution measurements, *ex vivo* tissue imaging experiments were performed. PFP-loaded PDAF-2.4% was injected into the ventricle of a chicken heart and imaged with color Doppler, B-mode, and CPS ultrasound signals (Figure 4.21). The most intense area of B-mode imaging shows the position of nanoparticles after injection. However, the signal is difficult to differentiate from surround tissue, which also exhibits B-mode contrast. Corresponding regions in color Doppler and CPS signal demonstrate the low-background, millimeter-level imaging capabilities of contrast-enhanced ultrasound. The color Doppler speckle pattern reflects the lack of flow in the tissue, indicating the promise of PDAF-*i*% for the *in vivo* studies where differentiation between flow rates is vital for assessing tissue health. For comparison, water injected into the chicken heart tissue shows no signal by either contrast mode (Figure 4.22).
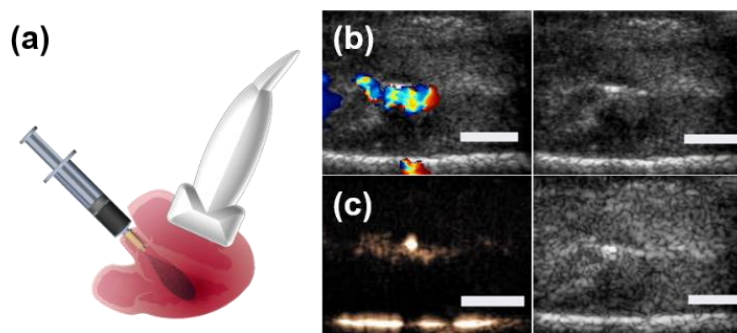
Figure 4.21 Representative data for chicken heart *Ex vivo* tissue experiments. (a) Schematic illustration of the imaging geometry and method for introducing contrast agent to the left ventricle and imaging through (b) Color Doppler and (c) CPS modes with PDAF-2.4% NPs. The black and white images at right are the underlying B-mode signal. The scale bar in panel (b) and (c) is 5 mm.
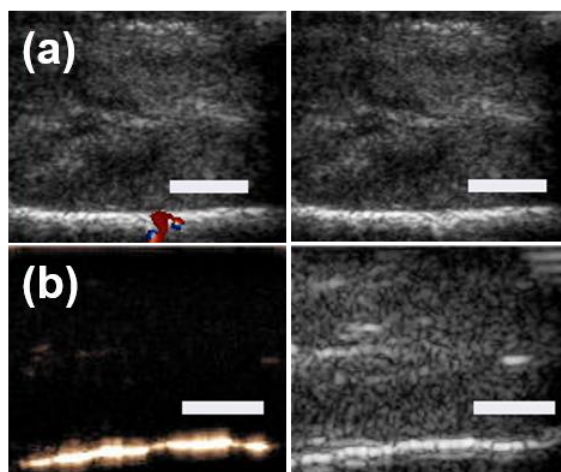
Figure 4.22 *Ex vivo* US imaging of deionized water in the left ventricle imaged through cardiac tissue of a chicken heart. The bright line at the bottom of (b) is an artifact. The scale bar in panel (b) and (c) is 5 mm.

4.3.4   In vitro and Ex vivo Photoacoustic Imaging of PDAF-i% NPs

As a complementary tool to conventional ultrasound imaging, photoacoustic (PA) imaging has attracted great research interest because it combines the high contrast and spectral nature of optics with the spatial and temporal resolution of ultrasound.[39-42] The PA signal arises from an optical pulse generating localized pressure waves within a strongly absorbing material such as a plasmonic nanoparticle and organic semiconductors.[43-48] Recent work has shown that PDA-based materials show strong PA imaging performance due to their high absorption in the NIR region.[39, 49] Additionally, traditional UCAs have demonstrated that US/PA dual-modal contrast is a viable technique for biological tissue imaging.[50] Given the strong absorption of PDAF-i% through 1000 nm (Figure 4.23), it could be expected that PFC-loaded PDAF-i% would display a bright PA signal in addition to US. In our study, a Vevo 2100 LAZA PA imaging system (Visualsonics) was used to scan the *in vitro* PA signal of PFP and non-PFP-loaded PDAF-2.4% in aqueous solution (Figure 4.24). PA imaging and its quantitative analysis are shown in Figure 4.24a and 4.24b. Not only is PA imaging possible in PFP-loaded PDAF-2.4%, but it is enhanced by roughly 40% compared with the equivalent non-PFP loaded sample, fitting with previously results on microbubble contrast

agents.[31, 50-52] As shown in ultrasound contrast, particle aggregation in the presence of PFC can be expected to play a role in the PA signal as well. Likely an effect of the enhanced absorption in the aggregates, a stronger signal is indeed observed for PDAF-large (Figure 4.20f). In addition, the Fe concentration of PDAF-*i*% was expected to play a role in PA imaging contrast due to charge transfer absorption involving the chelation to the PDA catecholate (Figure 4.25a,b).[18] Interestingly, this Fe^{3+} enhancement is most drastic when comparing PDAF-0.13% and all other samples. These data are consistent with the much lower extinction coefficient of PDAF-0.13% compared to that of other PDAF-*i*% samples (Figure 4.25c).
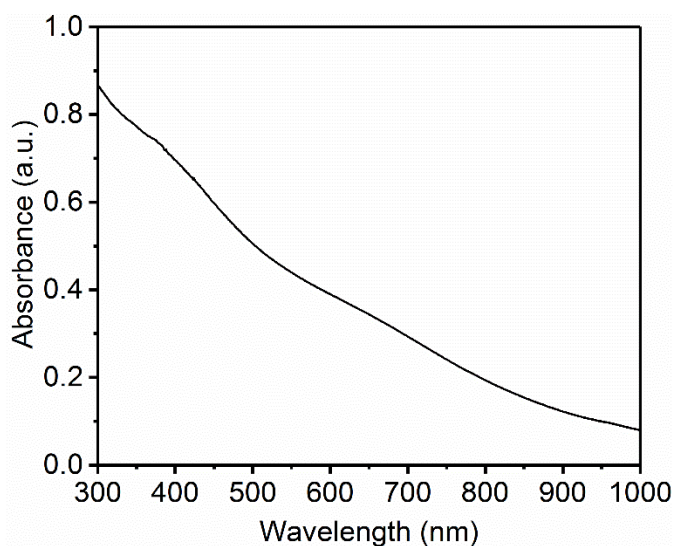
Figure 4.23 UV-vis spectrum of PDAF-2.4%.
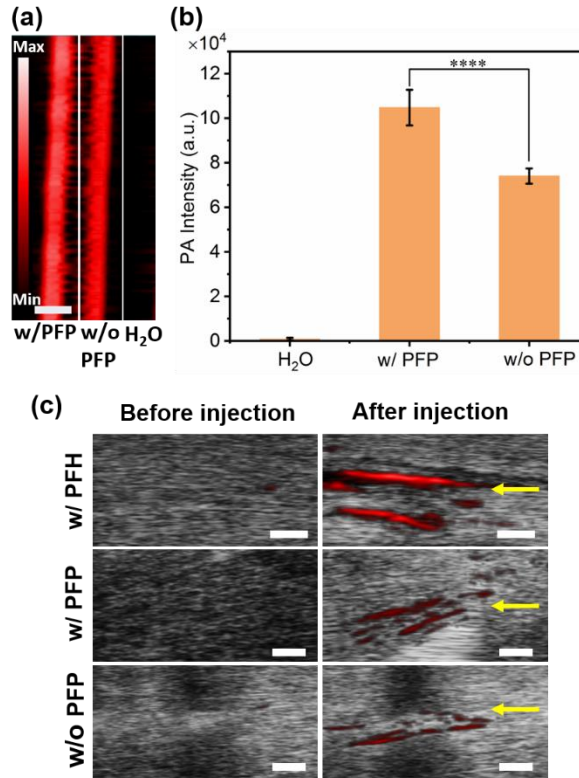
Figure 4.24 (a) *In vitro* PA imaging of PDAF-2.4% NPs, with (w/) or without (w/o) PFP loaded at 21 MHz. Scale bar = 2 mm. (b) the corresponding quantitative analysis of PA signal in (a), and the statistical significance was determined with t test, ****$p < 0.0001$, (c) *Ex vivo* PA and B-mode imaging of PDAF-2.4% in chicken breast tissue. The scale bar in panel (c) is 1 mm.
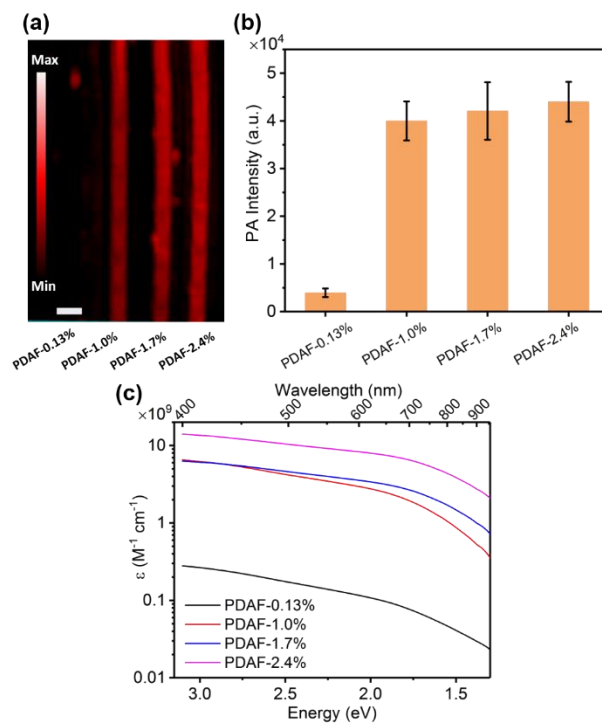
Figure 4.25 (a) *In vitro* PA imaging of PDAF-i% NPs under 0.5 mg mL^{-1} at 21 MHz, (b) the corresponding quantitative analysis of PA signal in (a), (c) molar volume extinction coefficient of PDAF-i%. The scale bar in panel (a) is 2 mm.

Ex vivo PA imaging of PDA particles in chicken breast tissue was also performed (Figure 4.24c, 4.26). PFH-, PFP- and no PFC-loaded PDAF-2.4% were injected 1 cm into the chicken breast tissue and subsequently imaged at the injection site at 40 MHz. The PA signal appears in the striations of the muscle fiber in the chicken breast tissue after the injection of nanoparticles, indicated by the red line in the Figure 4.24c. It should be noted that there is observable signal increase with PFC-loaded PDA samples compared with no PFC-loaded PDA samples, in agreement with the *in vitro* PA imaging results.

PDA is chemically similar to natural melanin and has been shown to be biocompatible in various synthetic forms. Figure 4.27 reveals that cell viability of all PDAF-*i*% is greater than 80% at all concentrations for HCT116 cells, indicating good biocompatibility for PDAF-*i*%.

Figure 4.26 Experimental setup for *ex vivo* PA imaging.
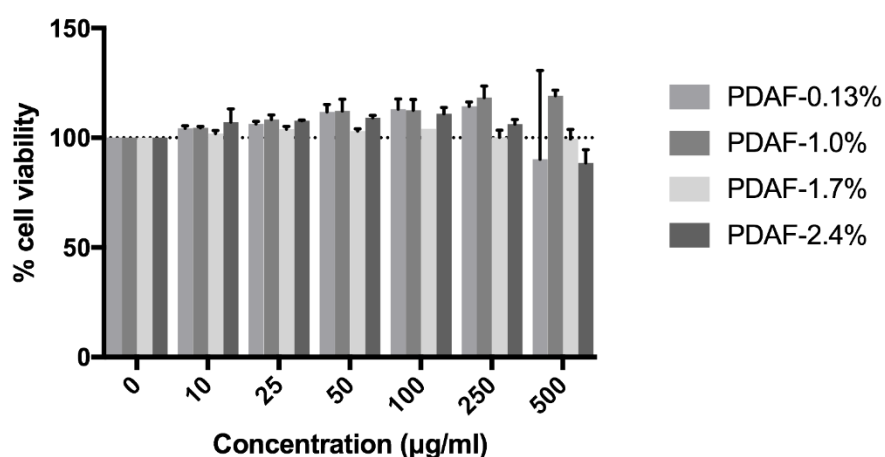
Figure 4.27 Cell viability of HCT116 cells after incubation with the concentration of PDAF-0.13%, PDAF-1.0%, PDAF-1.7%, and PDAF-2.4% increase from 0-500 µg/mL for 24 h.

4.3.5　In vivo Photoacoustic and Ultrasound Imaging of PDAF-i% NPs

The PFH-loaded PDAF-*i*% exhibits stable *in vivo* PA and color Doppler signal under constant laser exposure. The subcutaneously injected PFH-loaded PDAF-2.4% had 1.5 and 146.2-fold stronger PA intensity, with significantly higher color Doppler signal, than the negative controls PDAF-2.4% and Millipore water (Figure 4.28). Furthermore, the PA and color Doppler signal of the PFH-loaded PDAF-2.4% remained stable (RSD < 2.3%, Figure 4.29) during constant 700 nm laser excitation for 30 minutes with a detection limit of 0.12 mg/mL in the PA mode and ~2.0

mg/mL in the color Doppler mode (Figure 4.30). These results demonstrated the long-term *in vivo* utility of the PFH loaded PDAF-*i*% particles.

Overall, PDAF-*i*% demonstrate promising characteristics as UCAs: (1) They display strong contrast by both color Doppler and CPS imaging techniques; (2) the fluorophilic mode of PFC stabilization presents a way to image that is largely orthogonal to other tunable characteristics. Thus, synthetic handles such as size, metal content, constituent monomer can be repurposed to control tissue penetration, deliver alternate modes of contrast, or trigger therapeutic responses; (3) the stability of the PFC/particle interaction allows for long-term continuous imaging ability. This long-timescale ability could allow for long-term tracking of flow patterns and analysis of flow on tissue perfusion timescales.
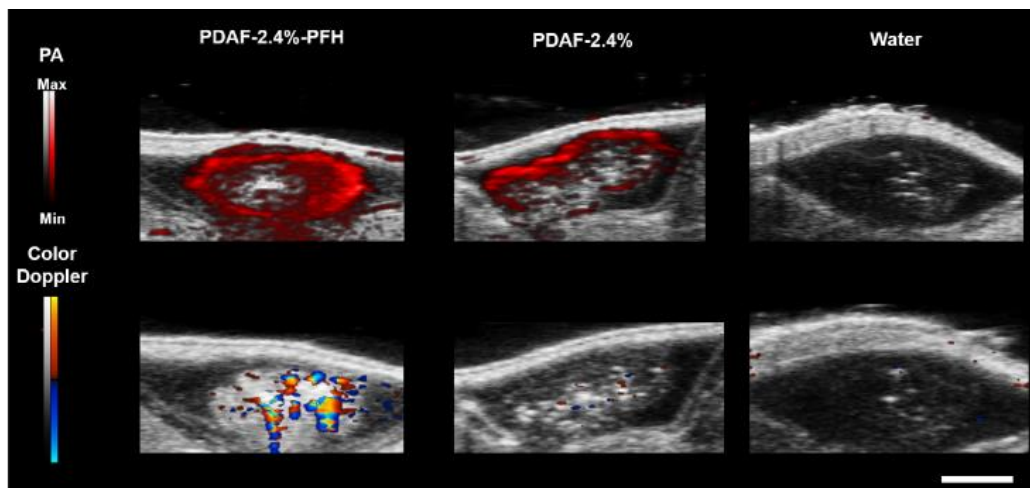
Figure 4.28 *In vivo* PA and color Doppler imaging with PFH-loaded PDAF-2.4% (2 mg mL^{-1}), PDAF-2.4% without PFH, and water control. Scale bar represents 2 mm.
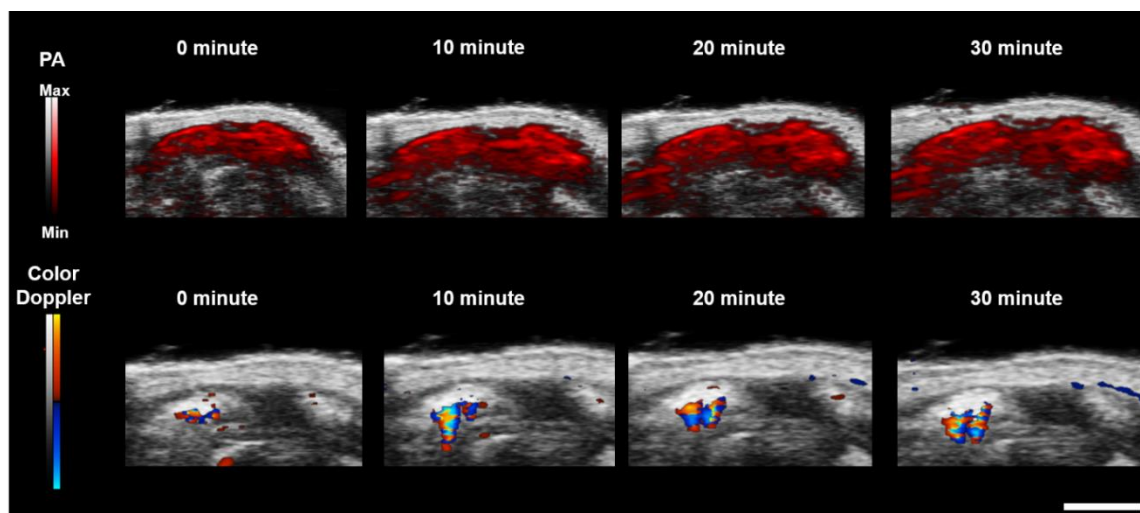
Figure 4.29 Time dependence of PA and color Doppler imaging from initial injection (0 min) to 30 min using PFH-loaded PDAF-2.4%. Scale bar represents 2 mm.
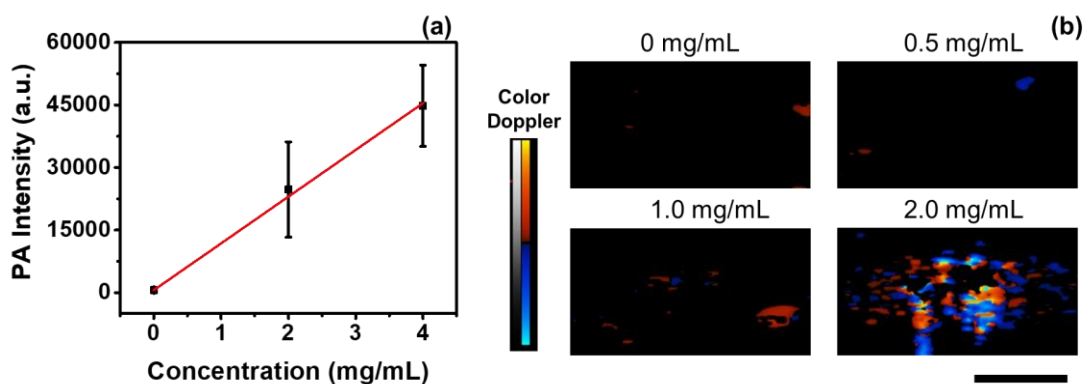
Figure 4.30 . The detection limit of the subcutaneous injected PFH-loaded PDAF-2.4% NPs is (a) 0.12 mg/mL (3 standard deviation above the average of baseline) for photoacoustic signal and (b) around 2.0 mg/mL for the color Doppler signal. Error bars in (a) represent standard deviation of 6 regions of interest. Scale bar represents 2 mm.

4.4 Experimental Section

4.4.1 Materials

Dopamine hydrochloride (DA, 99%) and perfluorohexanes (PFH) was purchased from Alfa Aesar. Ammonium hydroxide (NH$_3$·H$_2$O, 28%-30%) was purchased from VWR International. 1H,1H,2H,2H-Perfluorodecanethiol (97%) was purchased from Sigma-Aldrich. Perfluoropentane (PFP) was purchased from Strem Chemicals. Iron(III) chloride hexahydrate (FeCl$_3$·6H$_2$O, 98%) and ethanol (100%) was obtained

from Fisher Scientific. Perfluorobutane (PFB) was purchased from SynQuest Labs. All chemicals were used without further purifications. Deionized water is used in all the experiments.

4.4.2 Synthesis of PDA-Fe-i% NPs

PDA-Fe-0.13% NPs were synthesized using ethanol-water system by modifying the reported methods.[10, 25, 53-54] Briefly, 60 mg of DA was mixed with 20 mL of ethanol and 60 mL of water under stirring, and subsequently 8 mg of $FeCl_3 \cdot 6H_2O$ in 20 mL of water was added to the mixture. After vigorous stirring for 10 min, 20 mL of water containing 500 µL of $NH_3 \cdot H_2O$ was quickly added to the mixed solution. After stirring for 24 h at room temperature, the product is centrifuged and washed with deionized water three times. In the case of PDA-Fe-1.0%, PDA-Fe-1.7%, and PDA-Fe-2.4% NPs, the amount of $FeCl_3 \cdot 6H_2O$ and $NH_3 \cdot H_2O$ used is 12 mg and 600 µL for PDA-Fe-1.0%, 16 mg and 980 µL for PDA-Fe-1.7%, 20 mg and 1000 µL for PDA-Fe-2.4% NPs, respectively.

4.4.3 Synthesis of PDAF-i% NPs

PDAF-0.13% NPs were synthesized by functionalizing PDA-Fe-0.13% with 1H,1H,2H,2H-perfluorodecanethiol. First, the PDAF-0.13% particles obtained from the previous step was mixed with 10 mL of ethanol and 40 mL of water. Then 60 µL of 1H,1H,2H,2H-Perfluorodecanethiol was added to the mixed solution. After 5 min of vigorous stirring, 10 mL of water containing 150 µL of $NH_3 \cdot H_2O$ was quickly added to the mixture. After stirring for 24 h, the particles are separated by centrifugation and washed with water and ethanol three times, and the final product is PDAF-0.13%. PDAF-1.0%, PDAF-1.7%, and PDAF-2.4% are prepared in the same method using PDA-Fe-1.0%, PDA-Fe-1.7%, PDA-Fe-2.4%, respectively.

4.4.4 Preparation of PFC-loaded PDAF-i% NPs

PFC-loaded PDAF-i% NPs were prepared with the typical immersion method.[10, 55] PDAF-i% particles are first lyophilized at -55°C under 0.04 mbar overnight. Then 1 mg of PDAF-i% particles were

dispersed in 200 µL of PFC and sonicated for 10 s, evaporating the excess PFC until no PFC liquid was seen in the vial. After that, 2 mL of deionized water was added to the mixture and sonicated for another 10 s. The mixed solution was used for imaging experiments. Low speed centrifugation was performed by centrifuging the mixed solution at 2500 rpm for 3 min; the supernatant (PDAF-small) and precipitate (PDAF-large) were collected for the imaging experiments.

4.4.5 Characterization

TEM images were acquired on an FEI Tecnai G2 Spirit TEM operating at 120 kV. SEM images and elemental analysis were obtained by an FEI Quanta 250 SEM equipped with a Thermo Fisher Scientific EDS detector. STEM images and EDS spectra maps were acquired using a Hitachi HD-2300 Dual EDS Cryo STEM equipped with dual Thermo Fischer Scientific EDS detectors. The Hitachi HD-2300 was operated at 200 kV. DLS and zeta potential measurements were determined by Malvern Zetasizer Nano ZS90. XPS analysis was conducted on Thermo Fisher Scientific ESCALab 250Xi spectrometer using Al K-alpha X-ray source (1486.6 eV). The XPS spectra were calibrated with adventitious carbon peak at 284.8 eV. UV−vis spectra were measured on a PerkinElmer Lambda 35 UV/vis spectrophotometer. Optical microscope images were taken on an EVOS FL Auto Imaging System under transmitted light imaging mode.

4.4.6 Ultrasound imaging

Ultrasound imaging was collected on a Siemens Sequoia 512 with an Acuson 15L8 transducer at 7 MHz. 0.5 mg mL^{-1} of PDA particles in aqueous dispersions was tested for *in vitro* ultrasound imaging. Both color Doppler and CPS imaging were used for ultrasound imaging experiments. Both color Doppler and CPS modes are performed with the increase of MI from 0.06 to 1.9. CPS imaging was used at 7 MHz and image brightness was quantified by averaging the brightness over the region of interest using MATLAB

R2016b. Continuous imaging was performed by imaging at color Doppler mode at MI=1.9 until the signal decayed to the intensity of deionized water signal.

4.4.7 Ex vivo cardiac ultrasound experiments

100 µL of PFP-loaded PDAF-2.4% with 4 mg mL^{-1} was injected into the left ventricle of a chicken heart (2.5 cm × 3 cm). Color Doppler imaging commenced immediately after injection with an increase in MI from 0.06 to 1.9. Control experiments were performed by injecting deionized water into the tissue.

4.4.8 Photoacoustic imaging

Photoacoustic imaging was performed on a VisualSonics Vevo 2100 LAZR imaging system. Transducers with the frequency of 21 MHz and 40 MHz were used for the experiments. For *in vitro* experiments, 17 µL of PDA particles with 0.5 mg mL^{-1} was used for imaging at 21 MHz with pulsed laser excitation at 700 nm. ImageJ was used to quantify the PA signal. For the *ex vivo* experiments, PDAF-2.4% NPs (4 mg mL^{-1}) with 100 µL were injected into fresh chicken breast tissue (7 cm × 8 cm). PA as well as B-mode images were collected at the frequency of 40 MHz and laser wavelength of 700 nm.

4.4.9 Cytotoxicity assay

HCT116 colorectal carcinoma cells were plated at 2.5*103 cells/well in DMEM high glucose (Corning) + 10% FBS. Cell were grown for 24 hours and then treated with PDAF-*i*% NPs (pre-solubilized in H$_2$O) ranging from concentrations of 0-500 µg/ml for 24 hours. Then, the cells were washed twice with PBS, and 100 µL of media was added to each well, followed by 20 µL of CellTiter Aqueous One Solution (Promega). After 3 hours at 37 °C, solutions were centrifuged at 10,000 RPM for 10 minutes, three times, and supernatant was transferred to a new plate. Then absorbance readings were taken at 490 nm (test wavelength) and 690 nm (reference wavelength).

4.4.10 In vivo ultrasound and photoacoustic imaging

All animal studies were performed in accordance with the Institutional Animal Care and Use Committee (IACUC) at the University of California, San Diego (UCSD). Colloidal suspensions of PDAF-2.4% NPs (1, 2, 4, and 8 mg mL^{-1}, 50 µL) with or without PFH loading were mixed with Matrigel in a 1:1 ratio and subcutaneously injected into the loose skin over the back of a 5-month old nude mouse via an insulin syringe (BD Micro-Fine™). Due to timing and equipment constraints, prepared mixtures were transferred to the IACUC and stored at 4 °C for 4.5 h before *in vivo* experiments. The photoacoustic and color Doppler images were collected using the same VisualSonics LAZR photoacoustic scanner with a LZ550 transducer at 37 dB with and without 700 nm excitation, respectively. We repeated the experiment using a mixture of 50 µL Millipore water with 50 µL Matrigel as the negative control. For the signal stability measurement, the injected area was exposed to 700 nm laser for 10, 20, and 30 minutes and imaged using the photoacoustic or color Doppler mode. The photoacoustic images were exported as TIFF files and analyzed via ImageJ 1.49v.[56] The photoacoustic images were converted to grey scale (8 bit) and the raw integrated intensity of 6 regions of interested within one sample were measured. The limit of detection was calculated at 3 standard deviation above the average of the baseline. The color Doppler signal detection limit was estimated by comparing the signal of 2.0, 1.0, 0.5, and 0 mg/mL PDAF-PFH NPs that were subcutaneously injected in the nude mouse.

4.5 Conclusion

In vitro US imaging at 20°C and 37°C both show remarkable contrast pulse sequences (CPS) and color Doppler signal at MI = 1.9; and significant color Doppler signal could be found at MI = 0.87 at 37°C. It should be noted that our PDAF-*i*% NPs could be imaged at MI = 1.9 for at least 6 h and were effective after storage at 4°C for almost two months, a behavior markedly different from other type of microbubble-based agents as well as our previous PDA-F NPs.[10] Often in nanoparticle-based ultrasound UCAs, it is difficult to characterize the extent to which aggregation plays a role in the properties. Optimization of our

initial size distribution and careful separation by low speed centrifugation and immediate characterization have allowed us to address key differences due to nanoparticle aggregations. Importantly, our results indicate that both isolated particles and aggregations contribute to the overall signal we observe, but the differences are not simply in signal magnitude. Specifically, the threshold MI response for PDAF-small warrants further study and may hold cues as to the methods to further control and optimize this signal response. Future work will continue to push the limits of these materials to longer imaging time and more optimized ultrasound response via tuning the particle design. Given the wide known parameter space for modification of polymer nanoparticles, further capabilities should be available, such as triggered positive contrast and multi-color contrast. This synthetic control of functionality offers the exciting possibility of specializing UCAs analogous to more established contrast agents like those of MRI, which have benefitted strongly from fundamental exploratory research into their structure-property relationships.

4.6 Acknowledgement

4.7 References

(1) Cai, W.; Chen, X. Nanoplatforms for Targeted Molecular Imaging in Living Subjects. *Small* **2007,** *3* (11), 1840-1854.

(2) Terreno, E.; Castelli, D. D.; Viale, A.; Aime, S. Challenges for Molecular Magnetic Resonance Imaging. *Chem. Rev.* **2010,** *110* (5), 3019-3042.

(3) Qian, X.; Han, X.; Chen, Y. Insights into the unique functionality of inorganic micro/nanoparticles for versatile ultrasound theranostics. *Biomaterials* **2017,** *142,* 13-30.

(4) Ferrara, K. W.; Borden, M. A.; Zhang, H. Lipid-Shelled Vehicles: Engineering for Ultrasound Molecular Imaging and Drug Delivery. *Acc. Chem. Res.* **2009,** *42* (7), 881-892.

(5) Nakatsuka, M. A.; Mattrey, R. F.; Esener, S. C.; Cha, J. N.; Goodwin, A. P. Aptamer-Crosslinked Microbubbles: Smart Contrast Agents for Thrombin-Activated Ultrasound Imaging. *Adv. Mater.* **2012,** *24* (45), 6010-6016.

(6) Yang, F.; Hu, S.; Zhang, Y.; Cai, X.; Huang, Y.; Wang, F.; Wen, S.; Teng, G.; Gu, N. A Hydrogen Peroxide-Responsive O2 Nanogenerator for Ultrasound and Magnetic-Resonance Dual Modality Imaging. *Adv. Mater.* **2012,** *24* (38), 5205-5211.

(7) Sirsi, S. R.; Borden, M. A. Microbubble compositions, properties and biomedical applications. *Bubble Sci. Eng. Technol.* **2009,** *1* (1-2), 3-17.
(8) Schutt, E. G.; Klein, D. H.; Mattrey, R. M.; Riess, J. G. Injectable Microbubbles as Contrast Agents for Diagnostic Ultrasound Imaging: The Key Role of Perfluorochemicals. *Angew. Chem., Int. Ed.* **2003,** *42* (28), 3218-3235.

(9) Zhou, Y.; Wang, Z.; Chen, Y.; Shen, H.; Luo, Z.; Li, A.; Wang, Q.; Ran, H.; Li, P.; Song, W.; Yang, Z.; Chen, H.; Wang, Z.; Lu, G.; Zheng, Y. Microbubbles from Gas-Generating Perfluorohexane Nanoemulsions for Targeted Temperature-Sensitive Ultrasonography and Synergistic HIFU Ablation of Tumors. *Adv. Mater.* **2013,** *25* (30), 4123-4130.

(10) Xie, Y.; Wang, J.; Wang, Z.; Krug, K. A.; Rinehart, J. D. Perfluorocarbon-loaded polydopamine nanoparticles as ultrasound contrast agents. *Nanoscale* **2018,** *10* (26), 12813-12819.

(11) Su, C.-F.; Merlitz, H.; Rabbel, H.; Sommer, J.-U. Nanoparticles of Various Degrees of Hydrophobicity Interacting with Lipid Membranes. *J. Phys. Chem. Lett.* **2017,** *8* (17), 4069-4076.

(12) Bao, Q.-Y.; Liu, A.-Y.; Ma, Y.; Chen, H.; Hong, J.; Shen, W.-B.; Zhang, C.; Ding, Y. The effect of oil-water partition coefficient on the distribution and cellular uptake of liposome-encapsulated gold nanoparticles. *Colloids Surf. B* **2016,** *146*, 475-481.

(13) Pickering, S. U. CXCVI.—Emulsions. *J. Chem. Soc., Trans.* **1907,** *91* (0), 2001-2021.

(14) Li, D. S.; Schneewind, S.; Bruce, M.; Khaing, Z.; O'Donnell, M.; Pozzo, L. Spontaneous Nucleation of Stable Perfluorocarbon Emulsions for Ultrasound Contrast Agents. *Nano Lett.* **2019,** *19* (1), 173-181.

(15) Li, D. S.; Lee, Y.-T.; Xi, Y.; Pelivanov, I.; O'Donnell, M.; Pozzo, L. D. A small-angle scattering environment for in situ ultrasound studies. *Soft Matter* **2018,** *14* (25), 5283-5293.

(16) Lemaster, J. E.; Chen, F.; Kim, T.; Hariri, A.; Jokerst, J. V. Development of a Trimodal Contrast Agent for Acoustic and Magnetic Particle Imaging of Stem Cells. *ACS Appl. Nano Mater.* **2018,** *1* (3), 1321-1331.

(17) Wang, J.; Lin, C.-Y.; Moore, C.; Jhunjhunwala, A.; Jokerst, J. V. Switchable Photoacoustic Intensity of Methylene Blue via Sodium Dodecyl Sulfate Micellization. *Langmuir* **2018,** *34* (1), 359-365.

(18) Li, Y.; Xie, Y.; Wang, Z.; Zang, N.; Carniato, F.; Huang, Y.; Andolina, C. M.; Parent, L. R.; Ditri, T. B.; Walter, E. D.; Botta, M.; Rinehart, J. D.; Gianneschi, N. C. Structure and Function of Iron-Loaded Synthetic Melanin. *ACS Nano* **2016,** *10* (11), 10186-10194.

(19) Wang, Z.; Xie, Y.; Li, Y.; Huang, Y.; Parent, L. R.; Ditri, T.; Zang, N.; Rinehart, J. D.; Gianneschi, N. C. Tunable, Metal-Loaded Polydopamine Nanoparticles Analyzed by Magnetometry. *Chem. Mater.* **2017,** *29* (19), 8195-8201.

(20) Wang, Z.; Carniato, F.; Xie, Y.; Huang, Y.; Li, Y.; He, S.; Zang, N.; Rinehart, J. D.; Botta, M.; Gianneschi, N. C. High Relaxivity Gadolinium-Polydopamine Nanoparticles. *Small* **2017,** *13* (43), 1701830.

(21) Hu, D.; Liu, C.; Song, L.; Cui, H.; Gao, G.; Liu, P.; Sheng, Z.; Cai, L. Indocyanine green–loaded polydopamine–iron ions coordination nanoparticles for photoacoustic/magnetic resonance dual-modal imaging-guided cancer photothermal therapy. *Nanoscale* **2016,** *8* (39), 17150-17158.
(22) Sun, J.; Xu, W.; Li, L.; Fan, B.; Peng, X.; Qu, B.; Wang, L.; Li, T.; Li, S.; Zhang, R. Ultrasmall endogenous biopolymer nanoparticles for magnetic resonance/photoacoustic dual-modal imaging-guided photothermal therapy. *Nanoscale* **2018,** *10* (22), 10584-10595.

(23) Cui, J.; Yan, Y.; Such, G. K.; Liang, K.; Ochs, C. J.; Postma, A.; Caruso, F. Immobilization and Intracellular Delivery of an Anticancer Drug Using Mussel-Inspired Polydopamine Capsules. *Biomacromolecules* **2012,** *13* (8), 2225-2228.

(24) Li, Y.; Jiang, C.; Zhang, D.; Wang, Y.; Ren, X.; Ai, K.; Chen, X.; Lu, L. Targeted polydopamine nanoparticles enable photoacoustic imaging guided chemo-photothermal synergistic therapy of tumor. *Acta Biomater.* **2017,** *47*, 124-134.

(25) Ge, R.; Lin, M.; Li, X.; Liu, S.; Wang, W.; Li, S.; Zhang, X.; Liu, Y.; Liu, L.; Shi, F.; Sun, H.; Zhang, H.; Yang, B. Cu2+-Loaded Polydopamine Nanoparticles for Magnetic Resonance Imaging-Guided pH- and Near-Infrared-Light-Stimulated Thermochemotherapy. *ACS Appl. Mater. Interfaces* **2017,** *9* (23), 19706-19716.

(26) Veith, G. M.; Dudney, N. J. Current collectors for rechargeable Li-air batteries. *J. Electrochem. Soc.* **2011,** *158* (6), A658-A663.

(27) Liberman, A.; Wang, J.; Lu, N.; Viveros, R. D.; Allen, C. A.; Mattrey, R. F.; Blair, S. L.; Trogler, W. C.; Kim, M. J.; Kummel, A. C. Mechanically Tunable Hollow Silica Ultrathin Nanoshells for Ultrasound Contrast Agents. *Adv. Funct. Mater.* **2015,** *25* (26), 4049-4057.

(28) Synnevag, J. F.; Austeng, A.; Holm, S. Adaptive Beamforming Applied to Medical Ultrasound Imaging. *IEEE Trans. Ultrason., Ferroelectr., Freq. Control* **2007,** *54* (8), 1606-1613.

(29) Liberman, A.; Wu, Z.; Barback, C. V.; Viveros, R.; Blair, S. L.; Ellies, L. G.; Vera, D. R.; Mattrey, R. F.; Kummel, A. C.; Trogler, W. C. Color Doppler Ultrasound and Gamma Imaging of Intratumorally Injected 500 nm Iron–Silica Nanoshells. *ACS Nano* **2013,** *7* (7), 6367-6377.

(30) Ke, H.; Wang, J.; Dai, Z.; Jin, Y.; Qu, E.; Xing, Z.; Guo, C.; Yue, X.; Liu, J. Gold-Nanoshelled Microcapsules: A Theranostic Agent for Ultrasound Contrast Imaging and Photothermal Therapy. *Angew. Chem., Int. Ed.* **2011,** *50* (13), 3017-3021.

(31) Santiesteban, D. Y.; Dumani, D. S.; Profili, D.; Emelianov, S. Y. Copper Sulfide Perfluorocarbon Nanodroplets as Clinically Relevant Photoacoustic/Ultrasound Imaging Agents. *Nano Lett.* **2017,** *17* (10), 5984-5989.

(32) Fernandes, D. A.; Fernandes, D. D.; Li, Y.; Wang, Y.; Zhang, Z.; Rousseau, D.; Gradinaru, C. C.; Kolios, M. C. Synthesis of Stable Multifunctional Perfluorocarbon Nanoemulsions for Cancer Therapy and Imaging. *Langmuir* **2016,** *32* (42), 10870-10880.

(33) Blum, N. T.; Yildirim, A.; Chattaraj, R.; Goodwin, A. P. Nanoparticles formed by acoustic destruction of microbubbles and their utilization for imaging and effects on therapy by high intensity focused ultrasound. *Theranostics* **2017,** *7* (3), 694-702.

(34) Wang, J.; Barback, C. V.; Ta, C. N.; Weeks, J.; Gude, N.; Mattrey, R. F.; Blair, S. L.; Trogler, W. C.; Lee, H.; Kummel, A. C. Extended Lifetime In Vivo Pulse Stimulated Ultrasound Imaging. *IEEE Trans. Med. Imaging* **2017,** *37* (1), 222-229.
(35) Chevalier, Y.; Bolzinger, M.-A. Emulsions stabilized with solid nanoparticles: Pickering emulsions. *Colloids Surf., A* **2013,** *439,* 23-34.

(36) Mørch, Ý.; Hansen, R.; Berg, S.; Åslund, A. K. O.; Glomm, W. R.; Eggen, S.; Schmid, R.; Johnsen, H.; Kubowicz, S.; Snipstad, S.; Sulheim, E.; Hak, S.; Singh, G.; McDonagh, B. H.; Blom, H.; de Lange Davies, C.; Stenstad, P. M. Nanoparticle-stabilized microbubbles for multimodal imaging and drug delivery. *Contrast Media Mol. Imaging* **2015,** *10* (5), 356-366.

(37) Wu, J.; Ma, G.-H. Recent Studies of Pickering Emulsions: Particles Make the Difference. *Small* **2016,** *12* (34), 4633-4648.

(38) Calliada, F.; Campani, R.; Bottinelli, O.; Bozzini, A.; Sommaruga, M. G. Ultrasound contrast agents: Basic principles. *Eur. J. Radiol.* **1998,** *27*, S157-S160.

(39) Dong, Z.; Feng, L.; Hao, Y.; Chen, M.; Gao, M.; Chao, Y.; Zhao, H.; Zhu, W.; Liu, J.; Liang, C.; Zhang, Q.; Liu, Z. Synthesis of Hollow Biomineralized CaCO3–Polydopamine Nanoparticles for Multimodal Imaging-Guided Cancer Photodynamic Therapy with Reduced Skin Photosensitivity. *J. Am. Chem. Soc.* **2018,** *140* (6), 2165-2178.

(40) Weber, J.; Beard, P. C.; Bohndiek, S. E. Contrast agents for molecular photoacoustic imaging. *Nat. Meth.* **2016,** *13*, 639.

(41) De La Zerda, A.; Zavaleta, C.; Keren, S.; Vaithilingam, S.; Bodapati, S.; Liu, Z.; Levi, J.; Smith, B. R.; Ma, T.-J.; Oralkan, O.; Cheng, Z.; Chen, X.; Dai, H.; Khuri-Yakub, B. T.; Gambhir, S. S. Carbon nanotubes as photoacoustic molecular imaging agents in living mice. *Nat. Nanotechnol.* **2008,** *3*, 557.

(42) Xu, M.; Wang, L. V. Photoacoustic imaging in biomedicine. *Rev. Sci. Instrum.* **2006,** *77* (4), 041101.

(43) Tian, C.; Qian, W.; Shao, X.; Xie, Z.; Cheng, X.; Liu, S.; Cheng, Q.; Liu, B.; Wang, X. Plasmonic Nanoparticles with Quantitatively Controlled Bioconjugation for Photoacoustic Imaging of Live Cancer Cells. *Adv. Sci.* **2016,** *3* (12), 1600237.

(44) Mallidi, S.; Larson, T.; Tam, J.; Joshi, P. P.; Karpiouk, A.; Sokolov, K.; Emelianov, S. Multiwavelength Photoacoustic Imaging and Plasmon Resonance Coupling of Gold Nanoparticles for Selective Detection of Cancer. *Nano Lett.* **2009,** *9* (8), 2825-2831.

(45) Tang, W.; Yang, Z.; Wang, S.; Wang, Z.; Song, J.; Yu, G.; Fan, W.; Dai, Y.; Wang, J.; Shan, L.; Niu, G.; Fan, Q.; Chen, X. Organic Semiconducting Photoacoustic Nanodroplets for Laser-Activatable Ultrasound Imaging and Combinational Cancer Therapy. *ACS Nano* **2018,** *12* (3), 2610-2622.

(46) Yang, Z.; Tian, R.; Wu, J.; Fan, Q.; Yung, B. C.; Niu, G.; Jacobson, O.; Wang, Z.; Liu, G.; Yu, G.; Huang, W.; Song, J.; Chen, X. Impact of Semiconducting Perylene Diimide Nanoparticle Size on Lymph Node Mapping and Cancer Imaging. *ACS Nano* **2017,** *11* (4), 4247-4255.

(47) Yang, Z.; Fan, W.; Tang, W.; Shen, Z.; Dai, Y.; Song, J.; Wang, Z.; Liu, Y.; Lin, L.; Shan, L.; Liu, Y.; Jacobson, O.; Rong, P.; Wang, W.; Chen, X. Near-Infrared Semiconducting Polymer Brush and pH/GSH-Responsive Polyoxometalate Cluster Hybrid Platform for Enhanced Tumor-Specific Phototheranostics. *Angew. Chem., Int. Ed.* **2018,** *130* (43), 14297-14301.
(48) Yang, Z.; Dai, Y.; Yin, C.; Fan, Q.; Zhang, W.; Song, J.; Yu, G.; Tang, W.; Fan, W.; Yung, B. C.; Li, J.; Li, X.; Li, X.; Tang, Y.; Huang, W.; Song, J.; Chen, X. Activatable Semiconducting Theranostics: Simultaneous Generation and Ratiometric Photoacoustic Imaging of Reactive Oxygen Species In Vivo. *Adv. Mater.* **2018,** *30* (23), 1707509.

(49) Zhu, H.; Qin, D.; Wu, Y.; Jing, B.; Liu, J.; Hazlewood, D.; Zhang, H.; Feng, Y.; Yang, X.; Wan, M.; Wu, D. Laser-Activated Bioprobes with High Photothermal Conversion Efficiency for Sensitive Photoacoustic/Ultrasound Imaging and Photothermal Sensing. *ACS Appl. Mater. Interfaces* **2018,** *10* (35), 29251-29259.

(50) Xu, R. X. Multifunctional microbubbles and nanobubbles for photoacoustic imaging. *Contrast Media Mol. Imaging* **2011,** *6* (5), 401-411.

(51) Kim, C.; Qin, R.; Xu, J. S.; Wang, L. V.; Xu, R. X. Multifunctional microbubbles and nanobubbles for photoacoustic and ultrasound imaging. *J. Biomed. Opt.* **2010,** *15* (1), 010510.

(52) Wilson, K.; Homan, K.; Emelianov, S. Biomedical photoacoustics beyond thermal expansion using triggered nanodroplet vaporization for contrast-enhanced imaging. *Nat. Commun.* **2012,** *3*, 618.

(53) Liu, Y.; Ai, K.; Liu, J.; Deng, M.; He, Y.; Lu, L. Dopamine-Melanin Colloidal Nanospheres: An Efficient Near-Infrared Photothermal Therapeutic Agent for In Vivo Cancer Therapy. *Adv. Mater.* **2012,** *25* (9), 1353-1359.

(54) Yue, Q.; Wang, M.; Sun, Z.; Wang, C.; Wang, C.; Deng, Y.; Zhao, D. A versatile ethanol-mediated polymerization of dopamine for efficient surface modification and the construction of functional core-shell nanostructures. *J. Mater. Chem. B* **2013,** *1* (44), 6085-6093.

(55) Picheth, G.; Houvenagel, S.; Dejean, C.; Couture, O.; Alves de Freitas, R.; Moine, L.; Tsapis, N. Echogenicity enhancement by end-fluorinated polylactide perfluorohexane nanocapsules: Towards ultrasound-activable nanosystems. *Acta Biomater.* **2017,** *64*, 313-322.

(56) Abràmoff, M. D.; Magalhães, P. J.; Ram, S. J. Image processing with ImageJ. *Biophotonics Intern.* **2004,** *11* (7), 36-42.

Chapter 5 Strengthening nanocomposite magnetism through microemulsion synthesis

5.1 Abstract

In this chapter, we studied the magnetic interactions between two particles in nanoparticle system. The magnetic strength and versatility of heterostructures generated via a simple microemulsion cluster-formation technique is demonstrated. This approach allows optimization of individual component magnetic nanoparticles prior to heterostructuring, expediting the discovery and optimization of hybrid magnetic materials. The efficacy of this method is validated through a magnetic study of nanoparticle clusters combining antiferromagnetic CoO and superparamagnetic $CoFe_2O_4$ nanoparticles with tunable particle ratio and size. An enhancement of coercivity compared with pure $CoFe_2O_4$ nanoparticles indicates that close interparticle contacts are achieved. Upon annealing, an exchange bias field of 0.32 T was observed – over twice that achieved in any other colloidally-synthesized system. Additionally, the unique microstructure is defined during cluster formation and thus protects magnetic coercivity during the annealing process. Overall, this work demonstrates a general approach for quickly exploring magnetic parameter space, designing interparticle functionality, and working towards the construction of high-value bulk magnets with low materials and processing cost.

5.2 Introduction

The design of new, commercially-viable magnetic materials is limited by the extreme difficulty in controlling or even predicting solid state reactivity. Thus more common approaches are to manipulate the

shape, grain size, and surface structure of known materials [1-3]; or to interface different known materials with synergistic properties [4-5]. Combinations of these two methodologies have resulted in nearly every major advance in magnet-based technologies of the last thirty years [6-7]. One such approach that is particularly intriguing is to intimately interface single-domain grains of two different types of magnetic materials so that their combined properties result in exchange bias effects [5, 8-10]. In exchange bias materials, magnetic coupling between an antiferromagnetic layer and a ferromagnetic (or blocked superparamagnetic) layer biases the anisotropy, effectively enhancing the coercivity of the magnet (Figure 5.1a) [9-10]. Achieving efficient magnetic exchange coupling is difficult, however, so exchange bias is still under active study to find widespread use in enhanced permanent magnets. Several approaches are being considered from top-down and bottom-up methodologies. A general top-down approach is to use ball milling [11], spark erosion [12], spark plasma sintering [13], or sputtering [14] to prepare small particles of the desired magnetic materials. These may be further reduced in size, mixed to increase heterogeneity, and fused with heat and pressure (Figure 5.1b). This approach has the advantage of simple, scalable processing but has difficulty achieving small, homogeneous domains and efficient surface contact [15]. Another method is through colloidally synthesized core/shell structures, effectively combining the antiferromagnet and ferromagnet into a single material (Figure 5.1c) [5, 16-20]. These materials have a built-in homogeneous phase distribution, making them ideal if relatively uniform thick shells can be grown. Designing these systems is synthetically demanding, so screening many material combinations can be time consuming.

With these challenges in mind, we sought to develop a straightforward protocol to allow low-temperature heterostructuring of well-defined colloidal nanoparticles to form strongly-interacting magnetic materials. In this work, we demonstrate how this can be accomplished using colloidally-prepared superparamagnetic $CoFe_2O_4$ (CFO) and antiferromagnetic CoO nanoparticles as the building blocks for oil-in-water microemulsion-based nanoclusters (Figure 5.1d). Formation of nanoparticle superstructures in microemulsions has been explored for numerous applications [21-26] and extending the method to binary magnetic clusters would ameliorate many of the issues that have hindered exploratory research in

109

heterostructured magnetic materials. The magnetic phases CFO and CoO were selected for their stability, low cost, and ease of measurement within our instrumental temperature range. Additionally, exchange bias in other formulations of this system has been either non-existent [20, 27] or very weak [28-30], yet the magnetic strength of the component structures suggests that with close surface interactions, it should be quite strong.
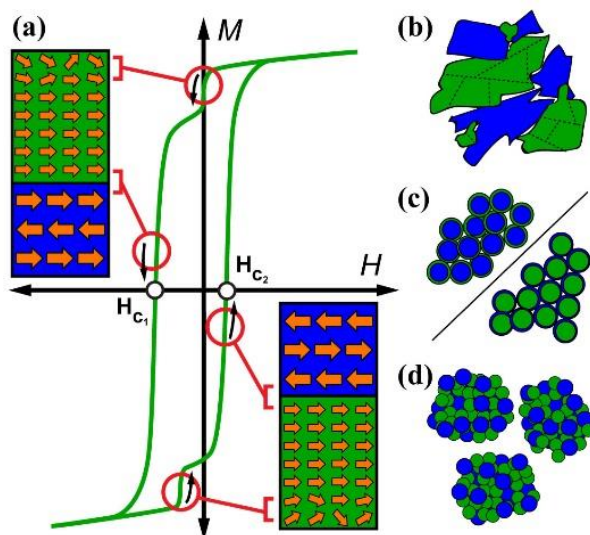
Figure 5.1 Illustrative figure of the phenomenon of magnetic exchange bias and materials capable of producing it: (a) The hysteresis loop of an exchange-biased material with the antiferromagnetic (blue) and ferromagnetic (green) layers coupled at their surface. Two areas of the curve are highlighted in red: one where the interlayer coupling is being broken by the field and the other where spins too far from the interface do not couple strongly. (b) Exchange-biased materials made by top-down method with mixed grains, (c) core/shell materials made by bottom-up method, and (d) mixed magnetic clusters made by oil-in-water micro-emulsion method as described herein. Copyright 2018, Tsinghua University Press and Springer-Verlag GmbH Germany.[31]

5.3 Results and Discussions

5.3.1   Synthesis and Characterizations of CoO and CFO NPs

Prior to formation of the magnetically-interacting nanoclusters, nanoparticles of CFO and CoO were synthesized and structurally characterized individually. Three CFO syntheses were performed, resulting in roughly spherical particles of diameter d = 4.9(0.8), 5.9(1.0), 11.6(2.0) nm (CFO-4.9, CFO-5.9, CFO-11.6; Figure 5.2a-c) [32-33]. Powder x-ray diffraction data confirms the phase as cubic spinel and Debye-Scherrer analysis yields crystallite sizes in agreement with the TEM particle size (Figure 5.3). All CoO

nanoparticles used in the study were from the same synthesis [34-35] with average diameter, d = 7.1(1.0) nm by TEM analysis and rock-salt structure from powder x-ray diffraction (Figure 5.4d, 5.3).
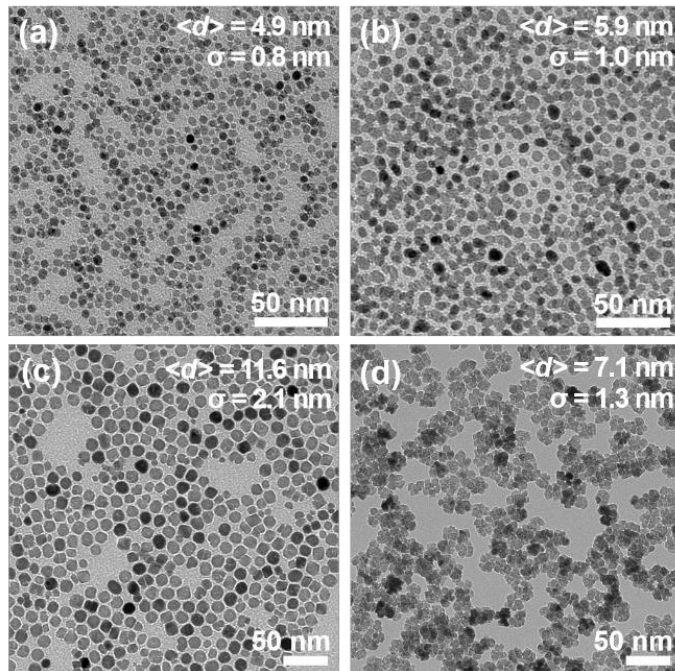
Figure 5.2 TEM images of (a) CFO-4.9, (b) CFO-5.9, (c) CFO-11.6, and (d) CoO nanoparticles. Copyright 2018, Tsinghua University Press and Springer-Verlag GmbH Germany.[31]
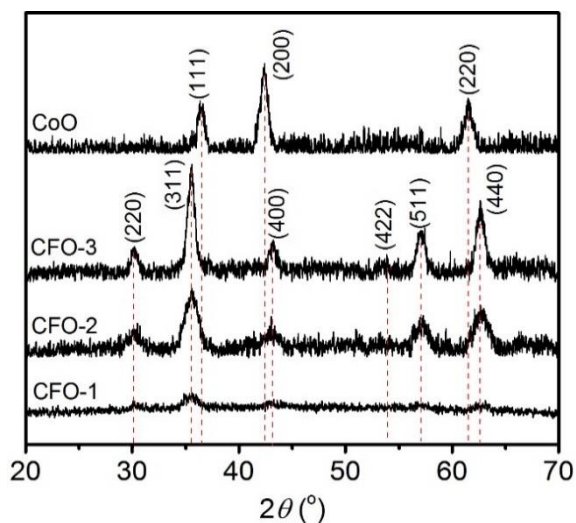
Figure 5.3 XRD patterns of CoO, CFO-4.9, CFO-5.9, and CFO-11.6 nanoparticles. Copyright 2018, Tsinghua University Press and Springer-Verlag GmbH Germany.[31]
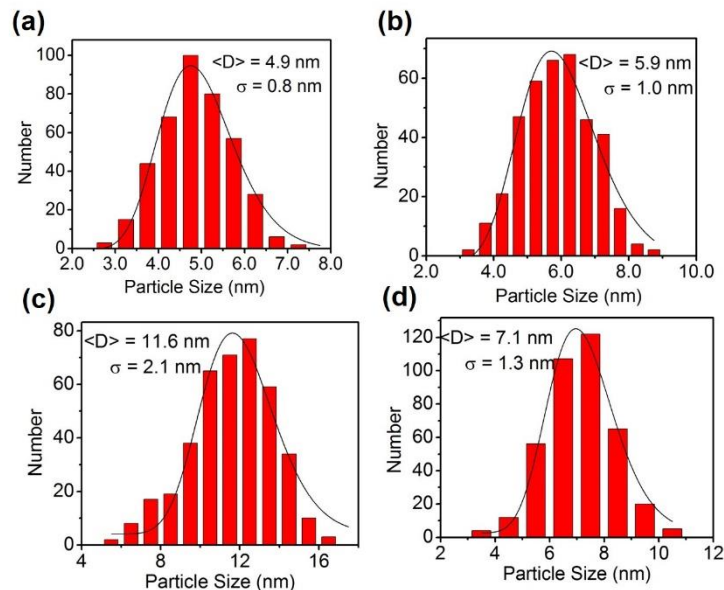
Figure 5.4 TEM size distribution diagrams of (a) CFO-4.9, (b) CFO-5.9, (c) CFO-11.6, and (d) CoO nanoparticles. Copyright 2018, Tsinghua University Press and Springer-Verlag GmbH Germany.[31]

The magnetism of CFO and CoO nanoparticles has been studied extensively, but due to surface, shape and compositional differences, their magnetic properties can vary between batches somewhat. To ensure consistency, all data reported herein were collected on samples from the same initial nanoparticle syntheses. As expected, magnetic blocking temperature (T_B) scales monotonically with particle diameter (Figure 5.5a-c). Field-dependent magnetization data was collected well below the lowest T_B, at 5 K (Figure 5.6a-c). At this temperature, all three samples display open hysteresis loops with roughly equivalent saturation magnetization (M_s) values of ~80 emu/g (Figure 5.6a-c). Nanoparticles of CoO display antiferromagnetic behavior with a Neel temperature (T_N) above 300 K. A small but measurable magnetization is present due to uncompensated spins at the particle surfaces (Figure 5.5d, 5.6d) [34-35].
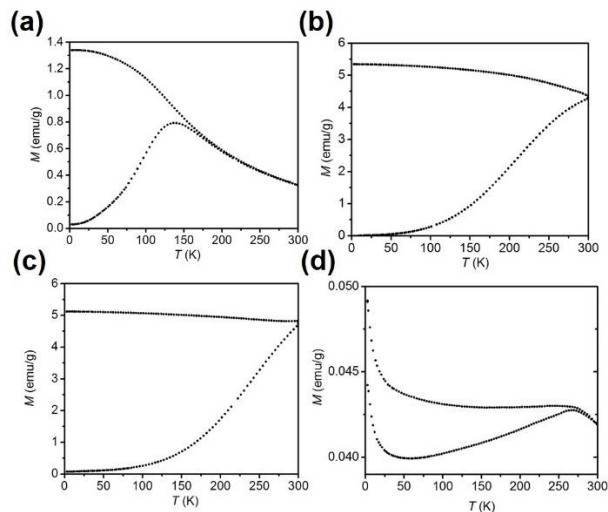
Figure 5.5 Plot of ZFC and FC DC magnetizations for (a) CFO-4.9, (b) CFO-5.9, (c) CFO-11.6, and (d) CoO. Copyright 2018, Tsinghua University Press and Springer-Verlag GmbH Germany.[31]
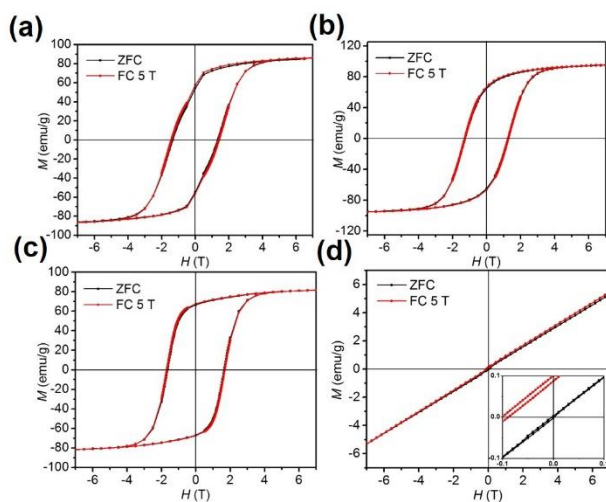
Figure 5.6 Hysteresis loops recorded at 5 K for (a) CFO-4.9, (b) CFO-5.9, (c) CFO-11.6, and (d) CoO. Copyright 2018, Tsinghua University Press and Springer-Verlag GmbH Germany.[31]

5.3.2   Synthesis and Characterizations of CoO-CFO clusters

Following characterization of the individual components, interparticle interactions were introduced between CFO and CoO nanoparticles through microemulsion-induced clustering (Figure 5.7). Addition of CoO and CFO NPs to a vigorously stirred, cetrimonium bromide (CTAB)-stabilized emulsion of hexane in water led to incorporation of the nanoparticles into the hydrophobic phase. Mild (80 °C) heating induced precipitation as the volatile hexane was removed. Clusters consisting of the remaining agglomerates of CoO

and CFO can be isolated as solids or redispersed in aqueous media upon the addition of excess CTAB. Three types of micro-emulsion clusters were synthesized in this manner: CoO-CFO-d; d = 4.9, 5.9, 11.6 (where d is the average TEM particle size of CFO in nm).

Figure 5.8a-c show the morphology of the as-prepared clusters. Interestingly, while the size mismatch between CFO and CoO does not have a large effect on the overall cluster size (120 to 150 nm), it does appear to affect the ability to form well-defined clusters as opposed to cluster/single-particle mixtures. Most nanoparticles are incorporated into well-defined clusters for CoO-CFO-d (d = 4.9, 5.9), however a relatively large number of individual or loosely connected particles can be seen in CoO-CFO-11.6. To demonstrate the cluster structure in detail, a high-magnification TEM image of CoO-CFO-5.9 (Figure 5.9) is shown, indicating well-defined CFO and CoO nanoparticles are distributed in the cluster structure. Future studies will determine if well-defined clusters require specific nanoparticle sizes, or if fine-tuning of the microemulsion conditions can produce better particle definition for all particle combinations.
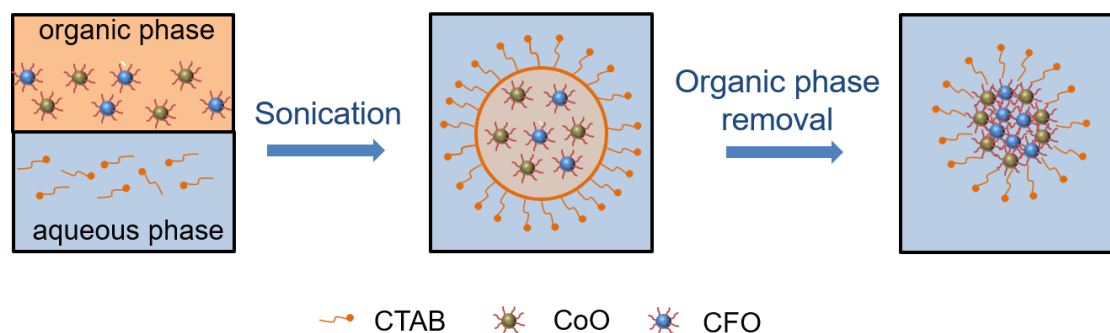
Figure 5.7 Schematic illustration of microemulsion synthesis of clusters. Copyright 2018, Tsinghua University Press and Springer-Verlag GmbH Germany.[31]
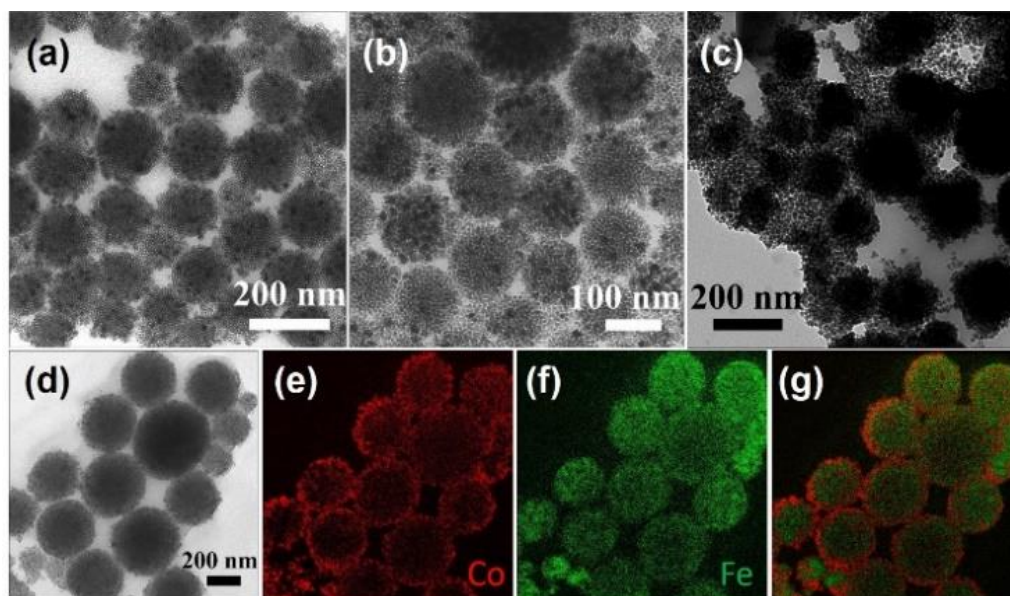
Figure 5.8 TEM images of (a) CoO-CFO-4.9, (b) CoO-CFO-5.9, (c) CoO-CFO-11.6, and representative TEM image for EELS mapping of (d) CoO-CFO-5.9 cluster, and EELS mapping of (e) Co mapping, (f) Fe mapping, (g) Composite of Fe and Co elemental mapping. Copyright 2018, Tsinghua University Press and Springer-Verlag GmbH Germany.[31]
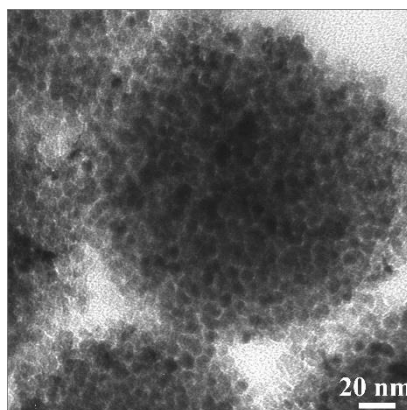
Figure 5.9 High-magnification TEM image of CoO-CFO-5.9. Copyright 2018, Tsinghua University Press and Springer-Verlag GmbH Germany.[31]

Given that some applications of these materials may require colloidal use, data were collected to check for stability in colloidal suspension. Dynamic Light Scattering (DLS) results indicate that resuspended clusters show an average hydrodynamic diameter of 205, 215, and 140 nm for CoO-CFO-d (d = 4.9, 5.9, 11.6), respectively (Figure 5.10b-d). Zeta potentials of dispersed CoO-CFO-d (d = 4.9, 5.9, 11.6) nanoclusters were measured as 31.4, 42.8, and 37.7 mV, respectively, indicating good stability in aqueous

solution. These data show that the nanoclusters remain intact and colloidally stable whereas many other inorganic heterostructuring methods hinder colloidal dispersibility. This allows for the possibility of developing exchange-enhanced magnetic nanoclusters for colloidal applications in magnetic hyperthermia [36], drug delivery [37], biosensing [38].

Another important aspect of the clusters characterization is the distribution of nanoparticles throughout the cluster. Representative Co and Fe elemental mapping of CoO-CFO-5.9 clusters with Electron Energy Loss Spectroscopy (EELS) indicates that Fe and Co are distributed relatively evenly, although there appears to be some preference for deposition of CoO on the surface (Figure 5.8e-f). This surface preference of Co is likely a result of differential packing of the nanoparticles in the microemulsion. The magnetic consequences of these structural differences are discussed below.
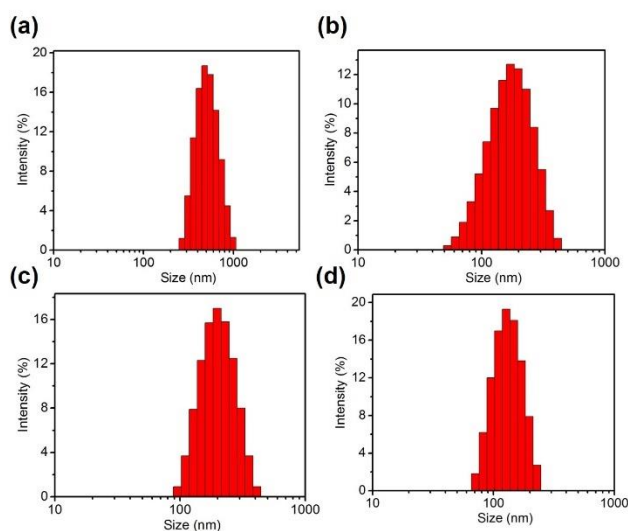
Figure 5.10 DLS size distribution diagrams of (a) oil-in-water microemulsion, (b) CoO-CFO-4.9, (c) CoO-CFO-5.9, and (d) CoO-CFO-11.6. Copyright 2018, Tsinghua University Press and Springer-Verlag GmbH Germany.[31]

5.3.3   Magnetic Characterization of CoO-CFO clusters

With magnetic characterization of individual nanoparticles, for comparison, a study of the changes induced by cluster formation was performed. Cluster samples were measured as solids without annealing or removal of the CTAB surfactant in order to assess the properties of isolate clusters.

Magnetization vs. magnetic field measurements were performed on cluster samples with an optimized molar ratio of 5.7 CoO:CFO (*vida infra*). Interestingly, all samples exhibit an enhancement of coercivity compared with pure CFO nanoparticles (Figure 5.11a, Figure 5.12) which can be attributed to an enhancement of magnetic anisotropy from the exchange interaction between the uncompensated spins at the surface of CoO nanoparticles and the spin of the CFO nanoparticles in the cluster. This analysis is corroborated by the enhancing effect of cooling the clusters under a 5 T magnetic field prior to magnetic measurement. Field-cooling (FC) aligns the magnetization of the CoO surface with the CFO, although the effect is much greater in systems where $T_B > T_N$. The enhanced coercivity in CoO-CFO-*d* is surprisingly robust and indicates that the hydrophobic nanoparticles pack tightly within the microemulsion and are further forced together as the nonpolar solvent evaporates. The end product is a dense cluster of high surface area CoO and CFO (Figure 5.9). Enhanced coercivity from interfacial contact between an antiferromagnet and a superparamagnet is well-documented, however observation of this behavior without chemical (core/shell) or harsh physical (sintering, high pressure) methods is not. To confirm that the magnetic enhancement was the result of forming microemulsion clusters and not simply due to efficient mixing, magnetization vs. magnetic field data were collected on co-precipitated CoO and CFO nanoparticle mixtures as well (Figure 5.11a). The co-precipitated particles show a steep drop in both their remnant magnetization (M_r) and H_C. This indicates that the microemulsion-formed clusters are required for producing the collective magnetic effects we observe. In addition, FC magnetization vs. field measurements reveal that CoO-CFO-5.9 shows significantly higher coercivity than clusters formed from pure CFO-5.9 (Figure 5.13), confirming that the cluster compaction of CoO and CFO leads to a boost in coercivity.
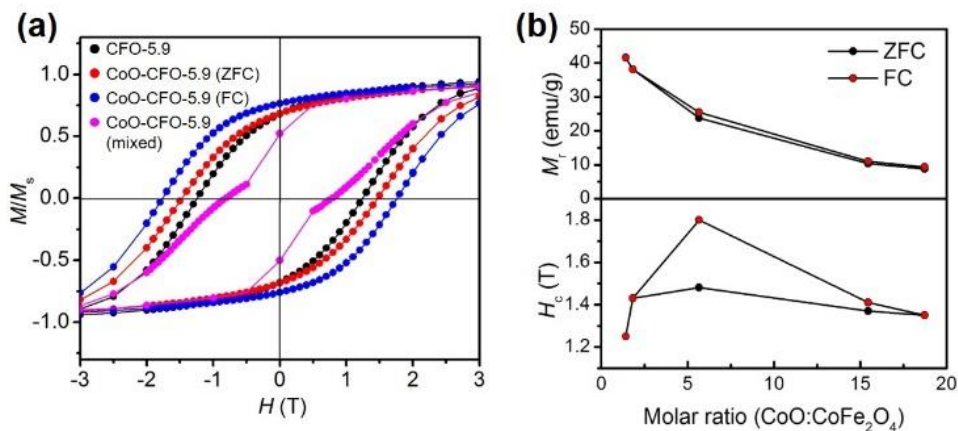
Figure 5.11 (a) Hysteresis loop of CoO-CFO-5.9 cluster and pure CFO nanoparticles recorded at 5 K: CFO-5.9 (black); CoO-CFO-5.9 with ZFC hysteresis loop (red); CoO-CFO with FC hysteresis loop (blue); mixed CoO and CFO-5.9 nanoparticles (pink), (b) plot of coercivity and remanence versus molar ratio of CoO to CFO for CoO-CFO-5.9. Copyright 2018, Tsinghua University Press and Springer-Verlag GmbH Germany.[31]
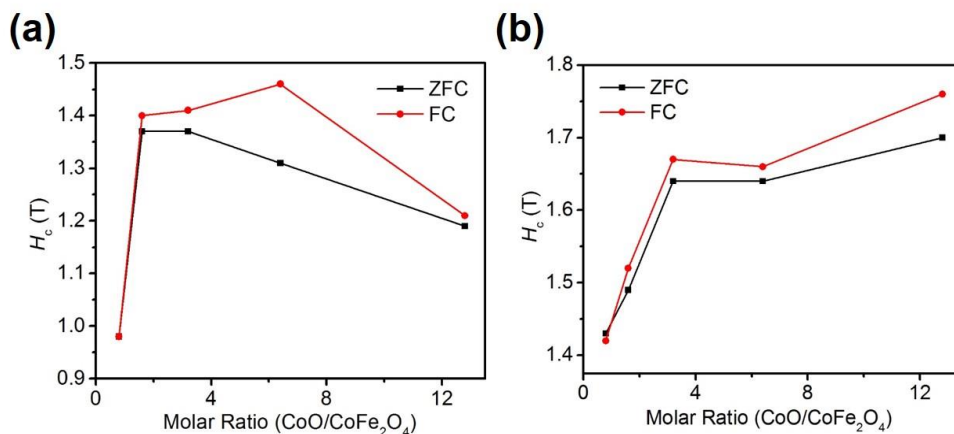
Figure 5.12 Plot of coercivity versus molar ratio of CoO to CFO for (a) CoO-CFO-4.9 and (b) CoO-CFO-11.6. Copyright 2018, Tsinghua University Press and Springer-Verlag GmbH Germany.[31]
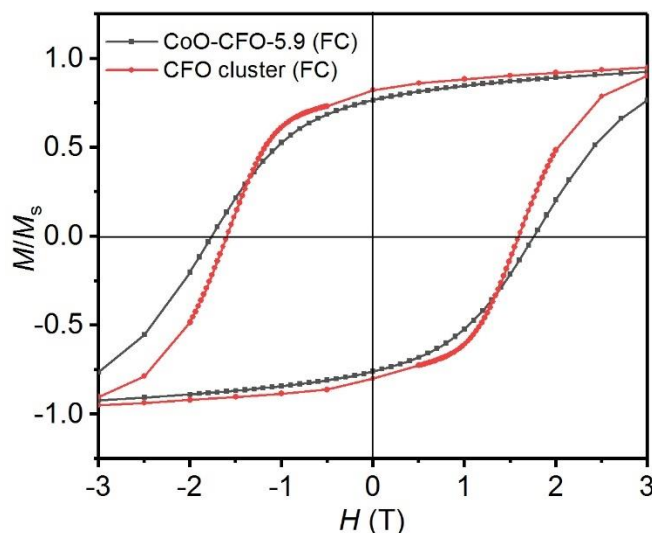
Figure 5.13 FC Hysteresis loops of CoO-CFO-5.9 cluster and pure CFO cluster recorded at 5 K. Copyright 2018, Tsinghua University Press and Springer-Verlag GmbH Germany.[31]

To assess the magnetic impact of varying the superparamagnetic CFO to antiferromagnetic CoO ratio, CFO-CoO-5.9 was synthesized with CoO:CFO molar ratios ranging from 1.4 to 18.7. As expected, increasing the CoO ratio leads to a monotonic decrease in M_r as the overall magnetization per unit mass is decreased (Figure 5.11b). Additionally, H_c is strongly affected by the molar CoO:CFO ratio, but only for a very narrow range of ratios. At the ideal ratio of 5.7:1, interparticle exchange interactions are optimized. The involvement of interactions between nanoparticles is confirmed by a further enhancement of H_c through cooling under a 5 T magnetic field.[20] Collectively, these data demonstrate how the formation of nanoclusters can be used to achieve stronger magnetic properties while maintaining colloidal stability.

Given the interaction between the antiferromagnetic CoO and superparamagnetic CFO, it is curious that no asymmetry is observed in the magnetic hysteresis loop. This indicates that microemulsion cluster process does not necessarily create interfacial exchange coupling conducive to the exchange bias effect. We found this to be true for all cluster samples and may be due to gaps in surface contact or interference from ligands.[39] Future refinement of our synthetic methods may circumvent these issues but another approach is to anneal the particles post-synthetically.

Annealing nanoparticle systems can lead to crystallite sintering and multidomain structures with drastically reduced coercivity;[40] however, we hypothesized that our preformed clusters would facilitate CoO-CFO exchange interactions at relatively low temperatures without inducing larger crystallite formation. Indeed, magnetization vs field data for CoO-CFO nanoclusters annealed at 350 $^{\circ}$C demonstrate minimal losses of H_C and the appearance of a large exchange bias effect (Figure 5.14a). The observed exchange bias field ($H_{ex} = -[H_{c2} + H_{c1}]/2$) was: 0.32 T, 0.07 T, and 0.1 T for CoO-CFO-d ($d = 4.9, 5.9, 11.6$), respectively. Amongst similar nanostructured systems these nanoclusters show superior performance (Table 5.1). Interestingly, CoO@CFO core-shell nanoparticles [20, 27] have thus far shown no evidence of exchange bias, possibly due to the shell structure being unable to support strong magnetic interactions.
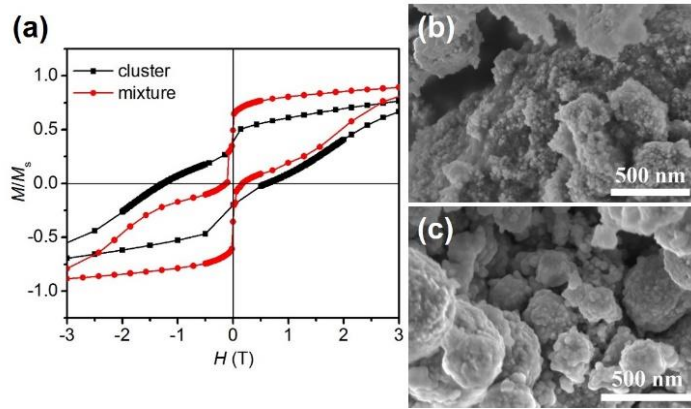
Figure 5.14 Magnetic and structural data for CoO-CFO-4.9 and mixtures of CoO and CFO-4.9: (a) Magnetization vs. magnetic field plot showing large exchange bias and preservation of coercivity for clusters vs. nanoparticle mixtures. (b) SEM images showing the microstructure of nanoparticle mixtures and (c) clusters. Copyright 2018, Tsinghua University Press and Springer-Verlag GmbH Germany.[31]

Table 5.1 Colloidally-synthesized exchange-bias materials.

Type	$<d>$ (nm)	T (K)	H_{ex} (T)	Ref
CoO/CFO	8.1	5	0	[41]
Co_3O_4/CFO	6.0	5	0.11	[38]
NiO/CFO	9.0	5	0.0233	[42]
Ni/NiO	9.0	2	0.114	[43]
CoO/$CoZnFe_2O_4$	10.0	5	0.14	[44]
CoO/CFO	4.9	5	0.32	This work

To determine if the large H_{ex} is truly dependent on cluster morphology, isolated CoO and CFO nanoparticles were colloidally suspended together, precipitated, anneal, and magnetically analyzed. If the annealing is solely responsible for the magnetic behavior we observe, no difference should exist between our microemulsion-synthesized clusters and the annealed mixtures. The nanoparticle mixtures, however, show drastically different magnetic behavior with large losses in magnetization around $H = 0$, loss of coercivity, and the lack of a spike in H_{ex}. These properties are quantified in the M_r/M_s values of 0.18, 0.41, and 0.50, H_{ex} values of 0.04 T, 0.14 T, and 0.06 T, and H_c values of 0.15 T, 1.06 T, and 0.85 T for mixtures of CoO with CFO-d (d = 4.9, 5.9, 11.6), respectively (Figure 5.14a, Figure 5.15). It should be noted that properties for these clusters have the potential to be improved through further optimization of experimental conditions. For instance, CoO-CFO-11.6 clusters have multiple drops in magnetization at different fields indicating phase separation or multidomain formation during the annealing process that could be eliminated through better cluster formation or refined annealing conditions.
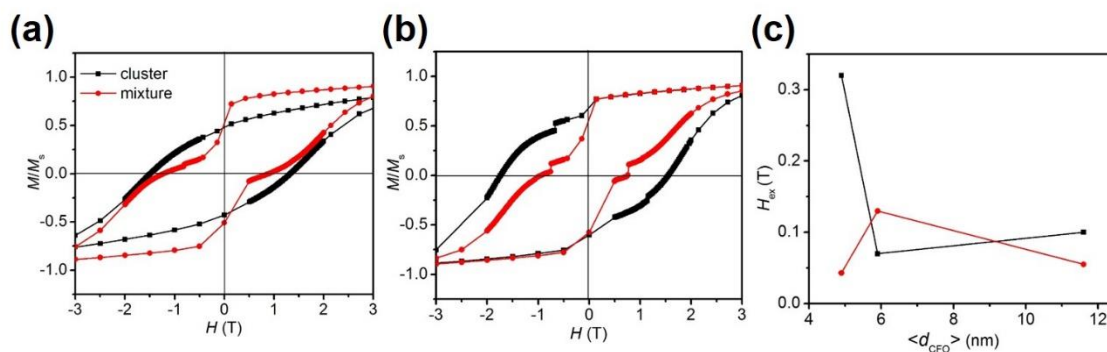
Figure 5.15 Field cooled hysteresis loops at 5 K of annealed (a) CoO-CFO-5.9 and mixture of CoO and CFO-5.9 NPs, (b) CoO-CFO-11.6 cluster and mixture of CoO and CFO-11.6 NPs; (c) Plots of average exchange bias versus size of CFO on annealed clusters and nanoparticle mixtures. Copyright 2018, Tsinghua University Press and Springer-Verlag GmbH Germany.[31]

Our results indicate the vital role played by the microstructure of the clusters compared to the annealed mixtures. A number of factors are expected to contribute to this. One factor is that segregation of CFO or CoO nanoparticles is limited in the clusters due to the small size of the microemulsion droplets. Thus, large regions of pure CoO or CFO do not form. Additionally, EELS mapping of Co (Figure 5.8e) indicates a preference for CoO at the cluster surface. This interfacial preference for CoO over CFO is a result of the size, shape and hydrophobicity differences between the nanoparticles and offers another handle by which to tune the magnetic properties of microemulsion clusters warranting further exploration. Due to this CoO "shell", the clusters are protected from the formation of low-H_c multidomain CFO crystallites during annealing. This compartmentalization is reinforced by the smaller surface area available for intercluster sintering compared to nanoparticle mixture sintering. These compartmentalized domain groups offer an interesting mechanism for circumventing an ever-present obstacle to high coercivity magnetism: Brown's paradox. Brown's paradox, or the tendency of the theoretical anisotropy field to vastly overestimate the experimental coercive field ($H_A \gg H_c$), is the results of local soft defects that propagate magnetization reversal throughout a material.[45-48] While the annealing of mixtures of nanoparticles takes place stochastically between all particles in the sample, CoO-CFO-d (d = 4.9, 5.9, 11.6) clusters are preferentially annealed in an intracluster fashion. This not only exploits the already intimate mixing created

122

by the emulsion clustering, but also limits defect-induced propagation of magnetization reversal to single clusters (Figure 5.14b,c). Control over nano- and microstructure is very difficult to achieve using bulk-synthesis, top-down methodologies and yet these methods demonstrate a way to systematically test models of extrinsic magnetic behavior and design magnets with optimized properties without the need for new exploratory solid state synthesis.

5.4 Experimental Section

5.4.1 Materials

The following reagents were used as received: iron(III) acetylacetonate ($Fe(acac)_3$, >99%) and cobalt(II) acetylacetonate ($Co(acac)_2$, 99%) were purchased from Acros Organics. 1,2-tetradecanediol (90%), oleylamine (70%), benzyl ether (>98%), and cetrimonium bromide (CTAB, 99%) were purchased from Sigma-Aldrich. Oleic acid (90%) was purchased from Alfa Aesar.

5.4.2 Synthesis of CoFe$_2$O$_4$ nanoparticles

$CoFe_2O_4$ nanoparticles were synthesized by a common thermal decomposition method in the presence of oleylamine and oleic acid [32-33, 49].

To synthesize 4.9 nm $CoFe_2O_4$ nanoparticles (CFO-4.9), $Fe(acac)_3$ (2 mmol), $Co(acac)_2$ (1 mmol), 1,2-tetradecanediol (10 mmol), oleylamine (6 mmol), oleic acid (6 mmol) and benzyl ether (20 mL) were added to a 100 mL three-necked flask. The mixture was heated to 60 °C and degassed with three cycles of reduced pressure (50 mbar) followed by reintroduction of nitrogen gas. Subsequently, the solution was heated to 200 °C at 5 °C/min under N_2 flow. After 30 min, the sample was heated to 265 °C at 10 °C/min. After another 30 min, the sample was removed from heat and allowed to cool to room temperature. The black suspension was fully precipitated with excess ethanol, centrifuged, redispersed in hexane, washed with ethanol three times, and dried (60 °C, < 50 mbar) for 12 h.

For 5.9 nm CoFe$_2$O$_4$ nanoparticles (CFO-5.9), after degassing, the precursor mixtures were heated at 5 °C/min to 200 °C for 1 h and then heated to 295 °C at 10 °C/min for 30 min. The washing and centrifugation cycles were identical to CFO-4.9.

For 11.6 nm CoFe$_2$O$_4$ nanoparticles (CFO-11.6), Fe(acac)$_3$ (5.3 mmol), CoCl$_2$ (2.7 mmol) were mixed with oleic acid (4 mmol), oleylamine (4 mmol) and benzyl ether (50 mL). The mixture was heated to 120 °C and was degassed under reduced pressure (<50 mbar) with vigorously stirring for 30 min. It was then heated to 270 °C at 3 °C/min for 15 min under N$_2$ flow. The washing and centrifugation cycles were identical to CFO-4.9.

5.4.3 Synthesis of CoO nanoparticles

The CoO nanoparticles were synthesized according to a previously reported method [34-35]. In a typical synthesis, Co(acac)$_2$ (3 mmol) was dissolved in oleylamine (30 mL). The mixture was heated to 230 °C at 3 °C/min and held for 30 min. Then the sample was removed from heat and allowed to cool to room temperature. The suspension was precipitated by excess ethanol, centrifuged, redispersed in hexane and washed with ethanol three times and dried (60 °C, < 50 mbar) for 12 h.

5.4.4 Synthesis of CFO-CoO nanoparticle cluster

The CoFe$_2$O$_4$-CoO nanoparticle clusters were prepared by an oil-in-water microemulsion method.[22, 50] Typically, CoO and CFO nanoparticles (25 mg total mass) were dispersed in hexane (150 μL) and added to a 20 mL vial with CTAB (0.1 mmol) aqueous solution (2 mL). The vial was then sonicated for 5 min. The mixture was heated in an 80 °C oil bath for an hour under constant stirring to promote evaporation of hexane. The clusters were collected by centrifugation at 10,000 rpm for 10 min. Nanoparticle clusters made from different sizes of CoFe$_2$O$_4$ were designated as CoO-CFO-4.9, CoO-CFO-5.9, and CoO-CFO-11.6 based on the varying size of the incorporated CoFe$_2$O$_4$ (4.9 nm, 5.9 nm, 11.6 nm, respectively). In annealing experiments, the nanoparticle clusters were heated at 350 °C for 1 h under Ar atmosphere.

5.4.5 Characterization

Crystalline structures were determined by powder X-ray diffraction (PXRD) using a Bruker D8 Advance diffractometer at 40 kV, 40 mA for Cu K$_\alpha$ (λ = 1.5418 Å) with a 2θ range of 20 – 70º, and a step size of 0.02º. Transmission electron microscope (TEM) images were obtained using an FEI Tecnai G2 Spirit operated at 120 kV. The size distribution of nanoparticles was calculated using Image J software analysis on sample sizes > 200 nanoparticles. Scanning electron microscope (SEM) images were recorded on a Zeiss Sigma 500 field emission scanning electron microscope operated at 3 kV. The electron energy loss spectroscopy (EELS) mapping of nanoclusters was investigated using a JEOL 3200 FS electron microscope working with a 300 kV accelerating voltage equipped with an Omega electron energy filter. Dynamic light scattering (DLS) size distribution and zeta potentials of nanoclusters was measured with a Malvern Zetasizer Nano ZS90.

5.4.6 Magnetic measurements

Magnetic measurements were performed using a Quantum Design MPMS3 superconducting quantum interface device (SQUID) magnetometer. Zero-field cooled (ZFC) and field cooled (FC) magnetization curves were carried out by first cooling the sample from 300 to 3 K under zero magnetic field. After cooling, the magnetic moment was recorded from 3 to 300 K with a 100 Oe applied field (ZFC) and the sample was again cooled from 300 to 3 K FC under 100 Oe while measuring magnetic moment (FC). For the exchange bias measurements (FC hysteresis loop), samples were first heated to 350 K and then cooled back to 5 K under a 5 T magnetic field, with subsequent measurement of the hysteresis loop. ZFC hysteresis loop were measured by sweeping the field from −7 T to 7 T with no cooling field.

5.5 Conclusion

In conclusion, we have presented a series of multicomponent nanoclusters with cooperative magnetic properties prepared by a versatile, well-established, and facile synthetic method. The nanoparticle clusters are found to form stable colloidal suspensions and demonstrate enhanced coercivity due to intracluster interactions between CoO and CFO nanoparticles. In addition to the enhanced magnetic behavior, additional nanoparticle components introduced into the microemulsion offer prospects for multifunctional applications in cellular uptake [51], magnetic resonance imaging (MRI) contrast agents [22] and catalysts [24].

Annealing these clusters leads to a large exchange bias effect for CoO-CFO-4.9, ($H_{ex,max} = 0.32$ T) higher than has been achieved in any other oxide nanoparticle system while largely retaining their coercivity, in contrast to mixtures of CoO and CFO. This result is especially intriguing as it suggests a multi-level structuring approach to magnetic solids wherein nanoparticle formation, cluster formation, and bulk annealing lead to magnetic materials that preserve far more of the intrinsic anisotropy than is possible by traditional methods. While one must still contend with inter-diffusion, phase separation and multidomain formation, the close interfacing achievable by microemulsion clustering should facilitate stronger interactions under milder annealing conditions. Future work will focus on improving the strength of interparticle interactions by altering or removing surface ligands, moving from proof-of-concept materials to high temperature, commercially-relevant magnetic materials, and expanding the scope of the magnetic interactions to include hard/soft ferromagnetic, magnetic/superconducting, and magnetic/plasmonic particle interactions.

5.6 Acknowledgement

author of this paper. For Chapter 5, I would like to thank Alexandre H. Vincent and Haeun Chang for the

nanoparticle synthesis. I also appreciate the project design of Prof. Jeffrey Rinehart.

5.7   References

(1) Brown, D.; Ma, B.-M.; Chen, Z. Developments in the processing and properties of NdFeb-type permanent magnets. *J. Magn. Magn. Mater.* **2002,** *248* (3), 432-440.

(2) Woodcock, T.; Zhang, Y.; Hrkac, G.; Ciuta, G.; Dempsey, N.; Schrefl, T.; Gutfleisch, O.; Givord, D. Understanding the microstructure and coercivity of high performance NdFeB-based magnets. *Scripta Mater.* **2012,** *67* (6), 536-541.

(3) Fischer, R.; Schrefl, T.; Kronmüller, H.; Fidler, J. Grain-size dependence of remanence and coercive field of isotropic nanocrystalline composite permanent magnets. *J. Magn. Magn. Mater.* **1996,** *153* (1-2), 35-49.

(4) Leighton, C.; Nogués, J.; Jönsson-Åkerman, B.; Schuller, I. K. Coercivity enhancement in exchange biased systems driven by interfacial magnetic frustration. *Phys. Rev. Lett.* **2000,** *84* (15), 3466.
(5) Estrader, M.; López-Ortega, A.; Estradé, S.; Golosovsky, I.; Salazar-Alvarez, G.; Vasilakaki, M.; Trohidou, K.; Varela, M.; Stanley, D.; Sinko, M. Robust antiferromagnetic coupling in hard-soft bi-magnetic core/shell nanoparticles. *Nat. Commun.* **2013,** *4*, 2960.

(6) Goll, D.; Seeger, M.; Kronmüller, H. Magnetic and microstructural properties of nanocrystalline exchange coupled PrFeB permanent magnets. *J. Magn. Magn. Mater.* **1998,** *185* (1), 49-60.

(7) Zeng, H.; Li, J.; Liu, J. P.; Wang, Z. L.; Sun, S. Exchange-coupled nanocomposite magnets by nanoparticle self-assembly. *Nature* **2002,** *420* (6914), 395.

(8) Skumryev, V.; Stoyanov, S.; Zhang, Y.; Hadjipanayis, G.; Givord, D.; Nogués, J. Beating the superparamagnetic limit with exchange bias. *Nature* **2003,** *423* (6942), 850-853.

(9) Nogués, J.; Sort, J.; Langlais, V.; Skumryev, V.; Surinach, S.; Munoz, J.; Baró, M. Exchange bias in nanostructures. *Phys. Rep.* **2005,** *422* (3), 65-117.

(10) Nogués, J.; Schuller, I. K. Exchange bias. *J. Magn. Magn. Mater.* **1999,** *192* (2), 203-232.

(11) Kremenović, A.; Jančar, B. t.; Ristić, M.; Vučinić-Vasić, M.; Rogan, J.; Pačevski, A.; Antić, B. Exchange-bias and grain-surface relaxations in nanostructured NiO/Ni induced by a particle size reduction. *J. Phys. Chem. C* **2012,** *116* (7), 4356-4364.

(12) Berkowitz, A.; Hansen, M. F.; Parker, F.; Vecchio, K.; Spada, F.; Lavernia, E.; Rodriguez, R. Amorphous soft magnetic particles produced by spark erosion. *J. Magn. Magn. Mater.* **2003,** *254*, 1-6.

(13) Rao, N. R.; Gopalan, R.; Raja, M. M.; Chandrasekaran, V.; Chakravarty, D.; Sundaresan, R.; Ranganathan, R.; Hono, K. Structural and magnetic studies on spark plasma sintered $SmCo_5$/Fe bulk nanocomposite magnets. *J. Magn. Magn. Mater.* **2007,** *312* (2), 252-257.

(14) Balasubramanian, B.; Das, B.; Skomski, R.; Zhang, W. Y.; Sellmyer, D. J. Novel Nanostructured Rare-Earth-Free Magnetic Materials with High Energy Products. *Adv. Mater.* **2013,** *25* (42), 6090-6093.

(15) Mendoza-Suarez, G.; Matutes-Aquino, J.; Escalante-Garcıa, J.; Mancha-Molinar, H.; Rıos-Jara, D.; Johal, K. Magnetic properties and microstructure of Ba-ferrite powders prepared by ball milling. *J. Magn. Magn. Mater.* **2001,** *223* (1), 55-62.

(16) Masala, O.; Seshadri, R. Spinel ferrite/MnO core/shell nanoparticles: chemical synthesis of all-oxide exchange biased architectures. *J. Am. Chem. Soc.* **2005,** *127* (26), 9354-9355.

(17) Zeng, H.; Sun, S.; Li, J.; Wang, Z.; Liu, J. Tailoring magnetic properties of core∕shell nanoparticles. *Appl. Phys. Lett.* **2004,** *85* (5), 792-794.

(18) Wang, L.; Wang, X.; Luo, J.; Wanjala, B. N.; Wang, C.; Chernova, N. A.; Engelhard, M. H.; Liu, Y.; Bae, I.-T.; Zhong, C.-J. Core− Shell-Structured Magnetic Ternary Nanocubes. *J. Am. Chem. Soc.* **2010,** *132* (50), 17686-17689.

(19) López-Ortega, A.; Tobia, D.; Winkler, E.; Golosovsky, I. V.; Salazar-Alvarez, G.; Estradé, S.; Estrader, M.; Sort, J.; González, M. A.; Surinach, S. Size-dependent passivation shell and magnetic properties in antiferromagnetic/ferrimagnetic core/shell MnO nanoparticles. *J. Am. Chem. Soc.* **2010,** *132* (27), 9398-9407.

(20) Lima Jr, E.; Winkler, E. L.; Tobia, D.; Troiani, H. E.; Zysler, R. D.; Agostinelli, E.; Fiorani, D. Bimagnetic CoO Core/CoFe$_2$O$_4$ shell nanoparticles: synthesis and magnetic properties. *Chem. Mater.* **2012,** *24* (3), 512-516.

(21) Bai, F.; Wang, D.; Huo, Z.; Chen, W.; Liu, L.; Liang, X.; Chen, C.; Wang, X.; Peng, Q.; Li, Y. A Versatile Bottom-up Assembly Approach to Colloidal Spheres from Nanocrystals. *Angew. Chem., Int. Ed.* **2007,** *46* (35), 6650-6653.

(22) Qiu, P.; Jensen, C.; Charity, N.; Towner, R.; Mao, C. Oil phase evaporation-induced self-assembly of hydrophobic nanoparticles into spherical clusters with controlled surface chemistry in an oil-in-water dispersion and comparison of behaviors of individual and clustered iron oxide nanoparticles. *J. Am. Chem. Soc.* **2010,** *132* (50), 17724-17732.

(23) Lu, Z.; Ye, M.; Li, N.; Zhong, W.; Yin, Y. Self-Assembled TiO2 Nanocrystal Clusters for Selective Enrichment of Intact Phosphorylated Proteins. *Angew. Chem., Int. Ed.* **2010,** *122* (10), 1906-1910.

(24) Chen, C.; Nan, C.; Wang, D.; Su, Q.; Duan, H.; Liu, X.; Zhang, L.; Chu, D.; Song, W.; Peng, Q.; Li, Y. Mesoporous Multicomponent Nanocomposite Colloidal Spheres: Ideal High-Temperature Stable Model Catalysts. *Angew. Chem., Int. Ed.* **2011,** *50* (16), 3725-3729.

(25) Liu, Y.; Zhang, Y.; Ding, H.; Xu, S.; Li, M.; Kong, F.; Luo, Y.; Li, G. Self-assembly of noble metallic spherical aggregates from monodisperse nanoparticles: their synthesis and pronounced SERS and catalytic properties. *J. Mater. Chem. A* **2013,** *1* (10), 3362-3371.

(26) Xiao, M.; Hu, Z.; Wang, Z.; Li, Y.; Tormo, A. D.; Le Thomas, N.; Wang, B.; Gianneschi, N. C.; Shawkey, M. D.; Dhinojwala, A. Bioinspired bright noniridescent photonic melanin supraballs. *Sci. Adv.* **2017,** *3* (9).

(27) Lavorato, G. C.; Lima Jr, E.; Tobia, D.; Fiorani, D.; Troiani, H. E.; Zysler, R. D.; Winkler, E. L. Size effects in bimagnetic CoO/CoFe$_2$O$_4$ core/shell nanoparticles. *Nanotechnology* **2014,** *25* (35), 355704.

(28) Tüysüz, H.; Salabaş, E. L.; Bill, E.; Bongard, H.; Spliethoff, B.; Lehmann, C. W.; Schüth, F. Synthesis of hard magnetic ordered mesoporous Co$_3$O$_4$/CoFe$_2$O$_4$ nanocomposites. *Chem. Mater.* **2012,** *24* (13), 2493-2500.

(29) Zhang, B.; Xu, J.; Wang, P.; Han, Y.; Hong, B.; Jin, H.; Jin, D.; Peng, X.; Li, J.; Yang, Y. Interfaces exchange bias and magnetic properties of ordered CoFe$_2$O$_4$/Co$_3$O$_4$ nanocomposites. *Appl. Surf. Sci.* **2015,** *355*, 531-535.

(30) Fan, S.; Wang, W.; Ke, H.; Rao, J.-C.; Zhou, Y. Bimagnetic urchin-like Co$_3$O$_4$/CoFe$_2$O$_4$ nanocomposites: synthesis and magnetic properties. *RSC Adv.* **2016,** *6* (99), 97055-97062.

(31) Xie, Y.; Vincent, A. H.; Chang, H.; Rinehart, J. D. Strengthening nanocomposite magnetism through microemulsion synthesis. *Nano Res.* **2018,** *11* (8), 4133-4141.

(32) Sun, S.; Zeng, H.; Robinson, D. B.; Raoux, S.; Rice, P. M.; Wang, S. X.; Li, G. Monodisperse MFe$_2$O$_4$ (M= Fe, Co, Mn) nanoparticles. *J. Am. Chem. Soc.* **2004,** *126* (1), 273-279.

(33) López-Ortega, A.; Lottini, E.; Fernandez, C. d. J.; Sangregorio, C. Exploring the magnetic properties of cobalt-ferrite nanoparticles for the development of a rare-earth-free permanent magnet. *Chem. Mater.* **2015,** *27* (11), 4048-4056.

(34) Seo, W. S.; Shim, J. H.; Oh, S. J.; Lee, E. K.; Hur, N. H.; Park, J. T. Phase-and size-controlled synthesis of hexagonal and cubic CoO nanocrystals. *J. Am. Chem. Soc.* **2005,** *127* (17), 6188-6189.

(35) Zhang, H.-T.; Chen, X.-H. Controlled synthesis and anomalous magnetic properties of relatively monodisperse CoO nanocrystals. *Nanotechnology* **2005,** *16* (10), 2288.

(36) Espinosa, A.; Di Corato, R.; Kolosnjaj-Tabi, J.; Flaud, P.; Pellegrino, T.; Wilhelm, C. Duality of iron oxide nanoparticles in cancer therapy: amplification of heating efficiency by magnetic hyperthermia and photothermal bimodal treatment. *ACS Nano* **2016,** *10* (2), 2436-2446.

(37) Ulbrich, K.; Holá, K. i.; Šubr, V.; Bakandritsos, A.; Tucek, J.; Zboril, R. Targeted drug delivery with polymers and magnetic nanoparticles: covalent and noncovalent approaches, release control, and clinical studies. *Chem. Rev.* **2016,** *116* (9), 5338-5431.

(38) Park, J.; Porter, M. D.; Granger, M. C. Colloidally Assembled Zinc Ferrite Magnetic Beads: Superparamagnetic Labels with High Magnetic Moments for MR Sensors. *ACS Appl. Mater. Interfaces* **2017,** *9* (23), 19569-19577.

(39) Schuller, I. K.; Morales, R.; Batlle, X.; Nowak, U.; Güntherodt, G. Role of the antiferromagnetic bulk spins in exchange bias. *J. Magn. Magn. Mater.* **2016,** *416*, 2-9.

(40) Herzer, G. Grain size dependence of coercivity and permeability in nanocrystalline ferromagnets. *IEEE Trans. Magn.* **1990,** *26* (5), 1397-1402.

(41) Lavorato, G. C.; Peddis, D.; Lima, E.; Troiani, H. E.; Agostinelli, E.; Fiorani, D.; Zysler, R. D.; Winkler, E. L. Magnetic Interactions and Energy Barrier Enhancement in Core/Shell Bimagnetic Nanoparticles. *J. Phys. Chem. C* **2015,** *119* (27), 15755-15762.

(42) Debnath, B.; Bansal, A.; Salunke, H. G.; Sadhu, A.; Bhattacharyya, S. Enhancement of Magnetization through Interface Exchange Interactions of Confined NiO Nanoparticles within the Mesopores of CoFe2O4. *J. Phys. Chem. C* **2016,** *120* (10), 5523-5533.

(43) Rinaldi-Montes, N.; Gorria, P.; Martínez-Blanco, D.; Fuertes, A. B.; Fernández Barquín, L.; Rodríguez Fernández, J.; de Pedro, I.; Fdez-Gubieda, M. L.; Alonso, J.; Olivi, L.; Aquilanti, G.; Blanco, J. A. Interplay between microstructure and magnetism in NiO nanoparticles: breakdown of the antiferromagnetic order. *Nanoscale* **2014,** *6* (1), 457-465.

(44) Lavorato, G. C.; Lima, E.; Troiani, H. E.; Zysler, R. D.; Winkler, E. L. Tuning the coercivity and exchange bias by controlling the interface coupling in bimagnetic core/shell nanoparticles. *Nanoscale* **2017,** *9* (29), 10240-10247.

(45) Balasubramanian, B.; Mukherjee, P.; Skomski, R.; Manchanda, P.; Das, B.; Sellmyer, D. J. Magnetic nanostructuring and overcoming Brown's paradox to realize extraordinary high-temperature energy products. *Sci. Rep.* **2014,** *4*, 6265.
(46) Brown Jr, W. F. Virtues and weaknesses of the domain concept. *Rev. Mod. Phys.* **1945,** *17* (1), 15.

(47) Kneller, E. F.; Hawig, R. The exchange-spring magnet: a new material principle for permanent magnets. *IEEE Trans. Magn.* **1991,** *27* (4), 3588-3560.

(48) Shtrikman, S.; Treves, D. In *in Magnetism*; Rado, G. T.; Suhl, H., Eds.; Academic Press: New York, 1963.

(49) Peddis, D.; Orrù, F.; Ardu, A.; Cannas, C.; Musinu, A.; Piccaluga, G. Interparticle interactions and magnetic anisotropy in cobalt ferrite nanoparticles: influence of molecular coating. *Chem. Mater.* **2012,** *24* (6), 1062-1071.

(50) Bai, F.; Wang, D.; Huo, Z.; Chen, W.; Liu, L.; Liang, X.; Chen, C.; Wang, X.; Peng, Q.; Li, Y. A Versatile Bottom-up Assembly Approach to Colloidal Spheres from Nanocrystals. *Angew. Chem., Int. Ed.* **2007,** *46* (35), 6650-6653.

(51) Wu, M.; Zhang, D.; Zeng, Y.; Wu, L.; Liu, X.; Liu, J. Nanocluster of superparamagnetic iron oxide nanoparticles coated with poly (dopamine) for magnetic field-targeting, highly sensitive MRI and photothermal cancer therapy. *Nanotechnology* **2015,** *26* (11), 115102.